Superfluid Helium and Cryogenic Noble Gases as Stopping Media for Ion Catchers

RIJKSUNIVERSITEIT GRONINGEN

Superfluid Helium and Cryogenic Noble Gases as Stopping Media for Ion Catchers

Proefschrift

ter verkrijging van het doctoraat in de
Wiskunde en Natuurwetenschappen
aan de Rijksuniversiteit Groningen
op gezag van de
Rector Magnificus, dr. F. Zwarts,
in het openbaar te verdedigen op
vrijdag 28 november 2008
om 13:15 uur

door

Sivaji Purushothaman

geboren op 21 december 1978
te Kozhikode–Kerala, India

Promotor:	Prof. Dr. K. P. Jungmann
Copromotor:	Dr. P. G. Dendooven

Beoordelingscommissie:	Prof. Dr. J. Äystö
	Prof. Dr. Ir. R. A. Hoekstra
	Prof. Dr. C. Scheidenberger

ISBN: 978-90-367-3651-0 Printed version
ISBN: 978-90-367-3652-7 Electronic version

This work has been performed as part of the research program of the "Stichting voor Fundamenteel Onderzoek der Materie" (FOM), which is financially supported by the "Nederlandse Organisatie voor Wetenschappelijk Onderzoek"; (NWO). This work has been supported by the EU 6th Framework programme "Integrating Infrastructure Initiative - Transnational Access", Contract Number: 506065 (EURONS) and by the Academy of Finland under the Finnish Centre of Excellence Programme 2006-2011 (Nuclear and Accelerator Based Physics Programme at JYFL).

PRINTED BY: Ponsen & Looijen B.V., Wageningen, November 2008.

"An experiment is a question which science poses to nature, and a measurement is the recording of nature's answer"

Max Planck
Scientific Autobiography and Other Papers, 1949

Contents

1 Introduction

The study of atomic nuclei takes a prominent position in the quest to understand quantum-mechanical many-body systems. Studying merely the naturally occurring atomic nuclei imposes a severe limit since these constitute only 5 % of the about 7000 combinations of protons and neutrons which are bound by the strong interaction. Experimental facilities where radioactive nuclei are created and studied are thus a necessity. The use and study of radioactive nuclei has had a great impact on other fields of science (ranging from particle physics to materials science) and has yielded an enormous amount of spin-off technologies and applications [3, 81, 117, 119]. For a long time, high-energy beams of only stable isotopes were readily available. In the past 25 years, radioactive ion beam (RIB) facilities allowed for the first time the study of many exotic nuclei with proton or neutron combinations very different than those of stable nuclei. This led to the discovery of many new and unexpected phenomena, such as halo nuclei and the melting of nuclear shells. The construction of next-generation RIB facilities is of the highest priority for the nuclear physics community. Such a next generation facility will produce beams with several orders of magnitude higher intensity, allowing new research with a wide range of nuclear species much further away from the region of stable nuclei. In RIB facilities of the in-flight type such as FAIR (Facility for Antiproton and Ion Research) at GSI, Germany [45], RIBF (Radioactive Ion Beam Factory), RIKEN, Japan [90], NSCL (National Superconducting Cyclotron Laboratory), MSU, United States of America [80] and GANIL (Grand Accélérateur National d'Ions Lourds), France [48], radioactive ions are produced and selected at high energies (100 - 1000 MeV per nucleon), resulting in a radioactive ion beam of high energy and poor beam quality (large emittance and large energy spread). Many precision studies of exotic nuclei far from the valley of stability, such as high-resolution particle spectroscopy or studies in atom or ion traps, need low-energy beams (typically less than a few tens of keV) of high quality (small emittance and energy spread smaller than 1 eV). The same requirements hold for the re-acceleration of the radioactive ions to a precisely defined energy needed e.g. for nuclear reaction studies with radioac-

tive ions. This makes the transformation of a high-energy, low-quality beam into a low-energy, high-quality one (a so-called "cold beam") an essential part of next generation RIB facilities. The essential requirements for such a transformation are speed and efficiency because the most exotic nuclei have short half-lives (down to milliseconds) and are produced in small quantities. The so-called "ion catcher" method to perform this transformation is being investigated in several laboratories for use in virtually all existing and planned RIB facilities. It is based on the IGISOL method developed in the early 1980's at the University of Jyväskylä, Finland by J. Ärje, J. Äystö and collaborators (see [9, 34] for reviews on this topic): the high-energy ions are stopped in a chamber filled with helium gas and extracted through an exit-hole. The size of the chambers required by the high energy of the RIB (up to 2 m long with a pressure of up to 2 bar) makes the use of the gas flow to extract the ions from the chamber too slow; guidance by DC electric fields or a combination of DC and RF fields is therefore an essential, but non-trivial task.

The main aim of this research programme is to check the feasibility of cryogenic noble gases and superfluid liquid helium as stopping medium. This thesis will discuss these two approaches separately. Physical processes behind both approaches are discussed in the next two chapters and the experimental techniques, results and discussion are presented in the following chapters.

The fundamental limit of efficiencies of a noble gas ion catcher has been an open question for years. Near and at thermal energies, ions cannot neutralize in collisions with noble gas atoms due to the high ionization potential of the latter. So in case of near zero impurity level, most of the neutralization of ions will happen during the slowing down process. This means that the relative importance of neutralization and ionization cross sections of the ion in the noble gas during slowing down will determine the efficiency limit of a noble gas ion catcher. The relevant physics has been explained since the early days of quantum theory of atomic collisions in the book "*The theory of atomic collisions*" by N. F. Mott and H. S. W. Massey [76]. However, accurate charge exchange cross sections could not be calculated accurately because of the mathematical complexity involved. The pioneering work by Hughes et al. on electron capture for singly charged particles like protons and muons [58] had been ignored in the nuclear physics community for some three decades and led to a series of misunderstandings. Some recent measurements of the average charge state of low-energy xenon ions in helium are reported by Willmann et al. [130]: the average charge state of xenon ions decreases down to about 0.25 at the lowest measured energy of 10 keV in full agreement with the expectations of the early models in the relevant range of energies.

What happens to thermalized ions is determined by the presence of impurities and the ionization of the noble gas by the energetic ions and possibly by an accelerator beam or radioactive decay radiation or both [6]. Impurities take part in the neutralization process via three-body recombination involving a free electron and form molecules or adducts with the ions, see e.g. Reference [65]. It is important to note that the ionizing radiation also plays a role in re-ionizing those ions which

have been neutralized. So one of the main factors that could improve the efficiency of the gas cells is a low impurity level. Over the past 25 years, a lot of technical development has focused on removing impurities from and preventing ionization of the noble gas. Sub-ppb impurity levels have been achieved in noble gas catchers that are built according to ultra-high vacuum standards, that are bakeable and filled with ultra-pure noble gases, see e.g. References [65, 93]. Constructing large ultra-pure gas catchers, although possible, is far from trivial [93]. There is, however, an alternative approach to reach ultra-pure conditions: freezing out the impurities. An added benefit of cryogenic gas catchers comes from the fact that for a constant gas density, the mass flow out of a gas cell is proportional to the square-root of the gas temperature. This means that a cryogenic noble gas cell allows easier differential pumping for the same gas density, or, reversing this argument, allows a higher density for a constant gas load on the extraction system. The latter means that higher energy ions can be stopped or that, for the same ion energy, the gas cell can be made shorter.

Chapter 4 is dedicated to describe the setup, the methods and the principles used for the experimental study and the data analysis.

Chapter 2 gives an overview of the physics involved in the processes and a literature survey on the available experimental data within the context of cryogenic noble gases. Off-line experiments using recoil ions from a radioactive ^{223}Ra source are performed to study the feasibility of using a cryogenic noble gas stopping medium for high-energy ion beams. Based on the off-line result, an on-line experimental study on the extraction of thermalized ^{219}Rn recoils from an ionized stopping medium was conducted. Results from both on-line and off-line experiments and a discussion of the observed properties are reported in chapter 5.

The much larger density (factor 800) of liquid helium relative to room temperature helium gas at 1 bar allows the use of a very small stopping chamber. This makes the extraction of the ions very fast, thereby also increasing the efficiency of ion extraction because of a reduction in neutralization and radioactive decay which is important for short-lived nuclei. Also, the guiding by electric fields can be very simple. The fact that nuclear polarization is preserved in superfluid helium [100, 111, 112, 106, 109, 110] could allow the extraction of polarized beams. At the envisaged temperatures, the low vapour pressure above the superfluid helium surface removes the need for pumping large volumes of helium gas. This new method, if proven successful, could be implemented in many existing and planned laboratories around the world. Experimental work to produce a cold radioactive ion beam using superfluid helium was started at the Department of Physics of the University of Jyväskylä about 7 years ago. ^{219}Rn ions created in the alpha decay of ^{223}Ra and recoiling out of the source were stopped in superfluid helium and extracted into the vapour phase as positive ions by means of electric fields. This was the first ever observation of the extraction of positive ions from the surface of liquid helium [56, 57, 108].

Different processes, most importantly the dependence of the survival of snow-

balls on applied electric fields and the dependence of their extraction across the superfluid-vapor interface on temperature are studied in the framework of this project. Chapter 3 give an essence of the physics tools necessary to understand the physical processes involved. The experiments described in chapter 6 aim towards a better understanding of the ion extraction at the superfluid-vapor interface. Further, as a new idea, the possibility to enhance the ion extraction efficiency by second sound assisted superfluid surface evaporation is also investigated.

Finally chapter 7 gives concluding remarks and discusses some future research directions.

2 Physics processes in cryogenic noble gas ion catchers

This chapter presents a brief review of the properties of electrons and positive ions in cryogenic helium gas. The mobility of electrons and positive ions and charge recombination processes play a critical role in the efficiency of a cryogenic helium ion catcher.

2.1 Electrons in low temperature helium gas

In the slowing down and thermalization of energetic heavy ion beams in cryogenic noble gas ion catchers, helium ion-electron pairs are created, resulting in partial ionization of the buffer gas. The electrons can be considered as an electron swarm. Such a swarm consists of a small number density n of electrons in a gas (in our case helium atoms) of much higher number density N. The most important physical parameters of an electron swarm within the parameter range of cryogenic noble gas ion catchers are the electron drift velocity v_d, the momentum transfer cross-section σ_m, the diffusion coefficient D and the recombination coefficient α. All these parameters are determined by the ratio E/N of the system where E is the applied electric field strength. E/N is often expressed in units of "Townsend" whose magnitude is defined as $1\ \mathrm{Td} = 10^{-17}\ \mathrm{V\,cm^2}$. It has been traditional to refer to the ratio of the ionic drift velocity v_d to the electric field strength E as the mobility μ, which is related to the diffusion coefficient through the Einstein relation (also known as Einstein-Smoluchowski relation) $D = \mu k_B T_g / e$. Here k_B is the Boltzmann constant, T_g is the gas temperature and e is the electron charge. This section will summarize the available data of the relevant parameters within the E/N range relevant for cryogenic

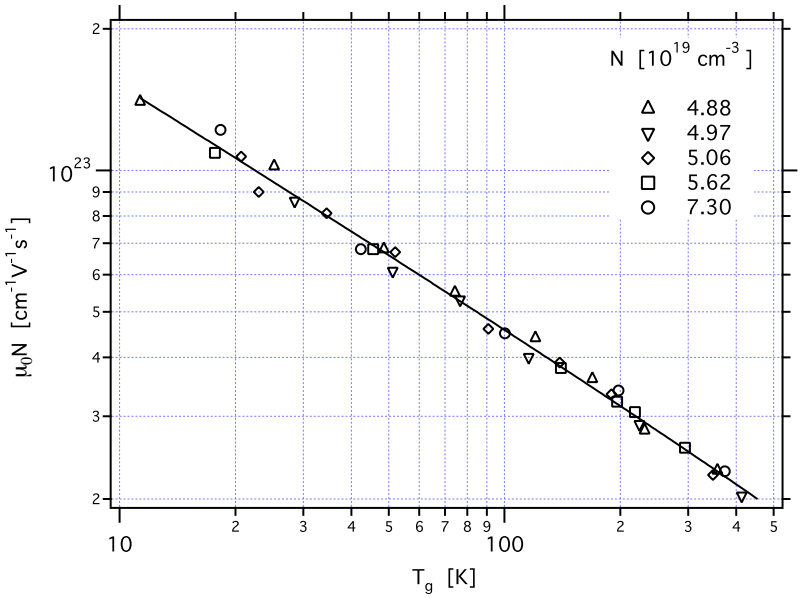

Figure 2.1: *Density-normalized zero field electron mobilities $\mu_0 N$ in helium as a function of temperature [88].*

noble gas ion catchers (10^{-3} Td $\leqslant E/N \leqslant 1$ Td, for $E = 1$ V cm^{-1} to 1000 V cm^{-1} while $N = 10^{20}$ cm^{-3} to 10^{18} cm^{-3}).

At lower densities electrons are quasifree. Their wave function is de-localised and the system can be treated with classical kinetic theory. This treatment assumes the conduction of electrons in an array of randomly placed scattering centers. This classical approach is valid at low densities and at high temperatures. The basic assumption of the kinetic theory is that the density of scatterers is so low that only binary collisions take place. This is valid only if the electron mean free path $l_c = (N\sigma_m)^{-1}$, the electron de Broglie wavelength $\lambda_T = h/(2\pi m k_B T_g)^{1/2}$, the atomic size a and the average inter-atomic distance $N^{-1/3}$ satisfy both the inequalities $l_c \gg N^{-1/3} > a$ and $l_c \gg \lambda_T$. In the limit of vanishingly small electric field ($E \to 0$) the kinetic theory predicts that the density-normalized zero-field mobility, $\mu_0 N$, of electrons is independent of the gas density N [96]

$$\mu_0 N = \frac{4}{3} \frac{e}{(2\pi m k_B T_g)^{1/2}} \frac{1}{\sigma_{m0}} , \tag{2.1}$$

where m is the mass, σ_{m0} the zero energy limit of the momentum transfer cross-section and μ_0 the zero field mobility of the electron. Figure 2.1 shows the zero-field electron mobility at different temperatures for different helium gas densities.

A large deviation from classical behavior is observed at high densities and at low temperatures. For $\lambda_T/l_c \sim 1$ the electron wave interacts with several scattering

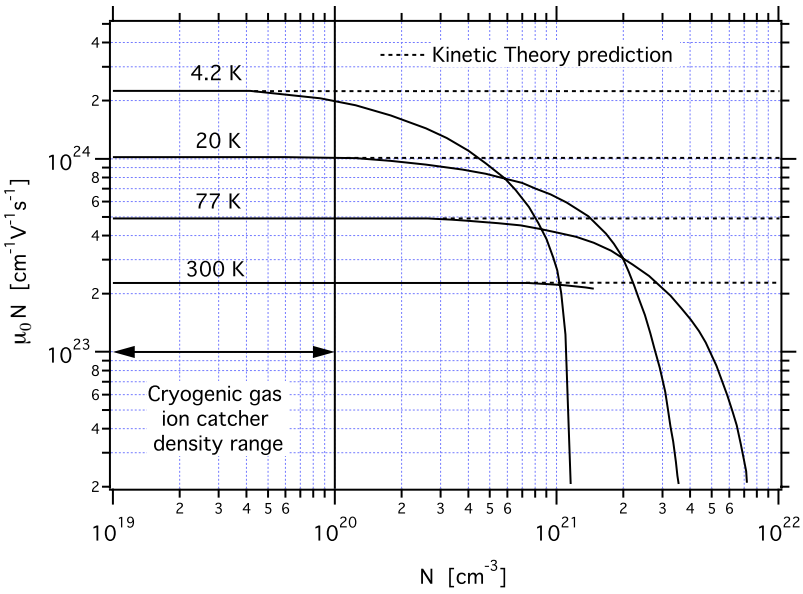

Figure 2.2: *Density-normalized zero-field mobility of electrons ($\mu_0 N$) vs. gas number density (N) of helium for various gas temperature values. Solid lines are summarized from many experimental results [53]. The relevant range for cryogenic noble gas ion catchers is indicated.*

centers simultaneously and usual complications associated with a random quantum mechanical system arise. For gas densities $N \gtrsim 10^{20}$ cm^{-3}, density-dependent effects for a given ratio E/N start to play a role. The deviation of density-normalised zero-field electron mobilities from the kinetic theory predictions with the increase in density and decrease in temperature are shown in Figure 2.2. For cryogenic gas ion catchers, the range of possible E/N and N values are well below the non-classical regime and the discussions in the following section will hence be restricted to the classical regime [11].

The most commonly available data on electron swarms is the electron drift velocity v_d. Figure 2.3 represents a compilation of drift velocity and density-normalized mobility data. At lower gas densities, the electron drift velocity is a function of the gas temperature T_g, and of the ratio E/N, but not of N independently. At very low E/N the electrons are in thermal equilibrium with the gas: the distribution of electron velocities is Maxwellian with a temperature equal to the gas temperature. Also, v_d depends linearly on the ratio E/N and can be described by the kinetic theory. At intermediate E/N the electron energy distribution is defined by elastic collisions and the mean electronic energy significantly exceeds the gas temperature. In this region the velocity distribution function changes from a Maxwellian to a Druyvesteynian distribution an v_d is proportional to $(E/N)^{1/2}$ because the scattering rate increases with the electron kinetic energy (see Figure 2.3).

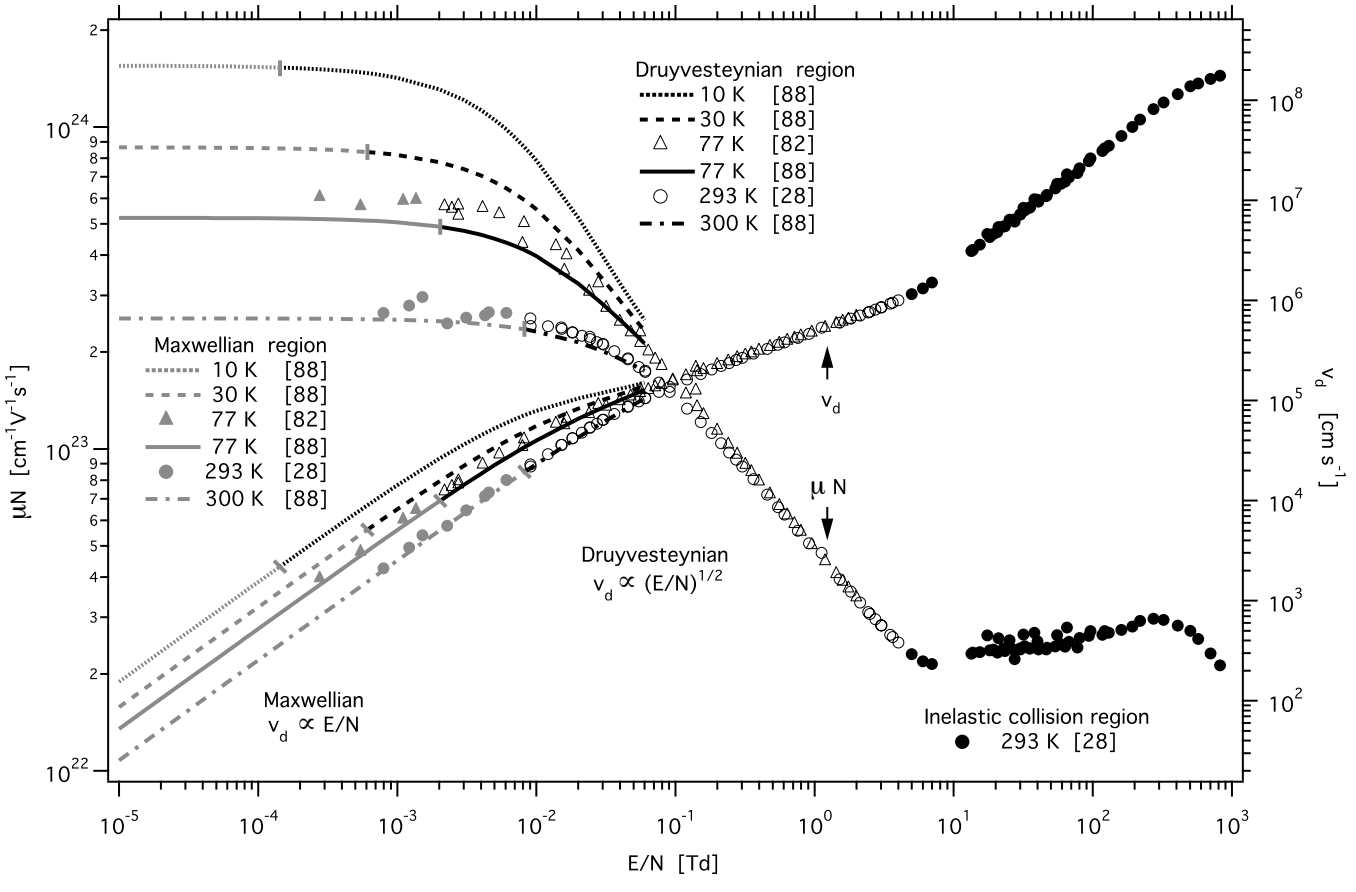

Figure 2.3: *Drift velocity v_d and density-normalized mobility μN of electrons in helium as a function of the ratio E/N [28, 82, 88].*

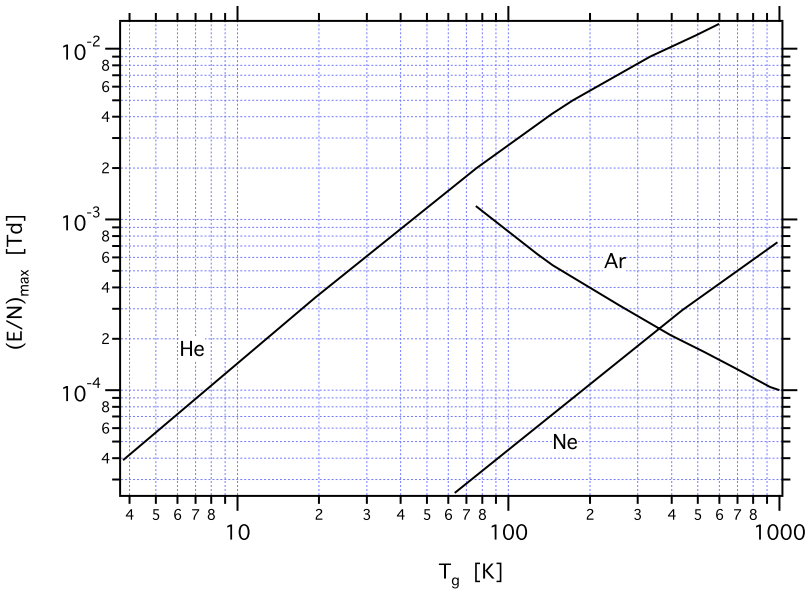

Figure 2.4: *Maximum value of the ratio E/N which can define the values of μ_0 in inert gases as a function of temperature. For $E/N < (E/N)_{max}$ the electron energy distribution function is Maxwellian [53].*

This transition occurs where the drift velocity is comparable to the thermal velocity of the ions.

For $E/N > 5$ Td, the electron energy distribution is modified by inelastic collisions and excitation of the helium gas limits the mean energy of the electrons [8].

The density-normalized mobility μN is a parameter often used to describe an electron swarm. Within the cryogenic noble gas ion catcher parameter range, μN is a function of E/N and T_g. At small values of E/N, μN is independent of E/N. From this characteristic, the value of zero-field mobility $\mu_0 N$ can be defined, which is only a function of T_g (see Figure. 2.1). Figure 2.4 shows the maximum value of E/N ($(E/N)_{max}$) for which μN is sill equal to $\mu_0 N_0$, where μ_0 is the zero-field mobility of electrons and N_0 is the Loschmidt number. The Loschmidt number is the molecular number density of an ideal gas at standard temperature 237.15 K and pressure 1 bar: $N_0 = 2.687 \times 10^{19}$ cm^{-3} [53]. In the Druyvesteynian regime, between 0.01 Td $\leqslant E/N \leqslant$ 5 Td, μN drops to a value of 2.5×10^{22} cm^{-1} V^{-1} s^{-1} and remains constant in the inelastic region 5 Td $\leqslant E/N \leqslant$ 300 Td due to the near constancy of the electron energy and the slowly varying electron collision frequency $\nu = N\sigma_m(2\langle\epsilon\rangle/m)^{1/2}$, where m is the electron mass, $\langle\epsilon\rangle$ is the characteristic energy of the electron swarm in this region (see Figure 2.5) and σ_m is the momentum transfer cross-section (see Figure 2.6).

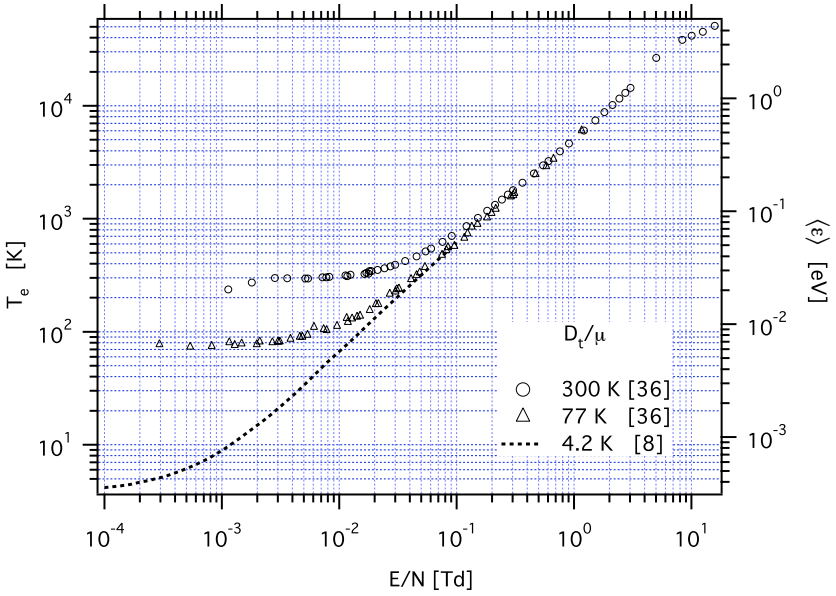

Figure 2.5: *Electron temperature T_e and characteristic energy $\langle\epsilon\rangle$ for electrons in helium as a function of the ratio E/N for gas temperatures $T_g = 300$ K, 77 K, and 4.2 K as determined from measurements of D_t/μ [8, 36].*

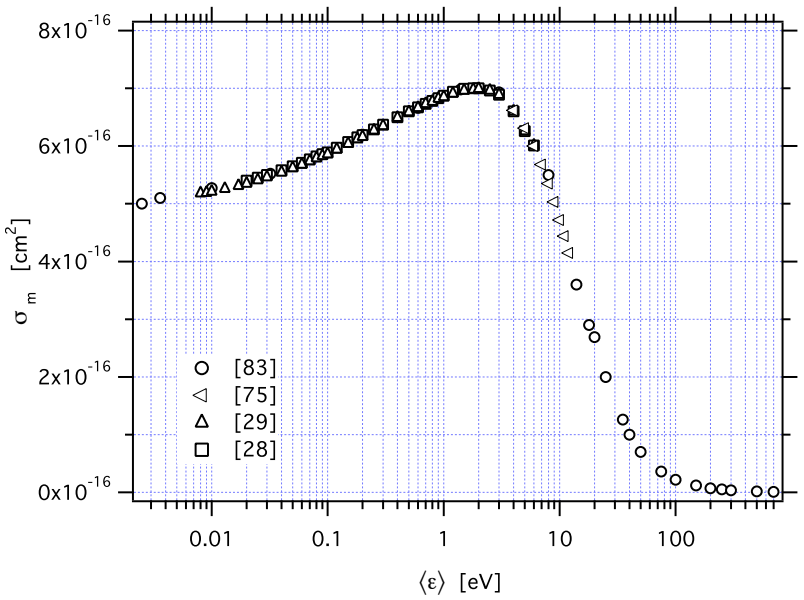

Figure 2.6: *Momentum transfer cross section σ_m of electrons in helium as a function of the electron energy $\langle\epsilon\rangle$ [28, 29, 75, 83].*

As an electron swarm drifts with a velocity v_d under the influence of an electric field E, it also diffuses due to the thermal motion of the electrons. At very low electric field strength diffusion is isotropic; at high electric field strength it acts as a tensor with components D_l and D_t along and transverse to the direction of the electric field. D_t/μ is a widely measured parameter of electron swarms, as it is approximately equal to the average electron energy $\langle\epsilon\rangle$ in the elastic collision region ($E/N \lesssim 5 \times 10^{-2}$ Td). $\langle\epsilon\rangle$ is of great significance in cryogenic noble gas ion catcher efficiency calculations as it directly gives the electron temperature $T_e = 2\langle\epsilon\rangle/3k_B$, which is an important parameter describing electron-ion recombination. T_e is sensitive to a variation of the momentum transfer cross-section σ_m. At low E/N electrons are in thermal equilibrium with the gas, and thus $T_e = T_g$. As E/N increases, the average value of T_e rises well above this value. In the simple case where only a constant elastic cross-section is involved, T_e increases linearly with E/N for values above T_g. If, however, the elastic collision cross-section increases or decreases with electron energy, T_e varies with E/N correspondingly, less or more rapidly than linearly. The momentum transfer cross-section of electrons in helium gas is almost constant up to electron energies of about 2 eV; for energies higher than 4 eV it decreases rapidly as the electron enters the inelastic collision regime (see Figure 2.6). In a similar fashion, the onset of inelastic collisions ($E/N \gtrsim 5$ Td) is evident in the T_e curve as a sudden decrease in its slope (see Figure 2.5) [4, 83].

2.2 Positive ions in low temperature helium gas

The ion mobility μ is defined as the ratio of the drift velocity v_d and the electric field E such that $v_d = \mu E$. At low electric fields the diffusion coefficient and the mobility hold the "Einstein relation" $D = \mu k_B T_g/q$, where q is the ion charge, D is the scalar diffusion coefficient and T_g is the gas temperature. This relation is valid only when the ions are close to thermal equilibrium with the neutral helium atoms. This means that the random thermal velocity is larger than the drift velocity v_d. If the electric field strength is large enough such that the average ion energy is larger than the thermal energy, the mobility μ is no longer constant but rather a function of the ratio of the electric field and the gas number density E/N. In this situation the energy distribution of the ions is non-Maxwellian and the diffusion coefficient is a tensor rather than a scalar. Viehland and Mason [120, 121] provided the first rigorous kinetic theory of ion mobility in neutral gases in which the ions are allowed to have a temperature different from that of the neutral-gas. This is referred as the two-temperature theory and is known to adequately describe ion mobility. The mobility μ of an ion according to the two-temperature theory is

$$\mu = \frac{v_d}{E} = \frac{3}{8}\frac{q}{N}\left(\frac{\pi}{2m'k_B T_{eff}}\right)^{1/2}\frac{1+\alpha}{\Omega^{(1,1)}(T_{eff})}\,, \tag{2.2}$$

$$m' = mM/(m+M) \tag{2.3}$$

were q is the ion charge, v_d is the ion drift velocity, N is the gas density, m' is the reduced mass, m and M are the ion and neutral gas atomic masses and $\Omega^{(1,1)}(T_{eff})$ is an energy-averaged momentum-transfer cross section. T_{eff} is the effective ion temperature and represents the total energy of the ions

$$\frac{3}{2}k_B T_{eff} = \frac{3}{2}k_B T_g + \frac{1}{2}Mv_d^2(1+\beta)\ , \tag{2.4}$$

where $\frac{3}{2}k_B T$ and $\frac{1}{2}Mv_d^2$ represent the thermal and the field part of the ion energy. The parameters α and β are higher order correction terms which depend in a complicated way on T_g, E/N, m, M and the ion-atom interaction potential. Numerical calculations have shown that in most practical cases α and β are substantially smaller than 0.01. The results obtained by setting them equal to zero are sufficiently accurate for most practical cases. The energy-averaged momentum transfer collision integral $\Omega^{(1,1)}(T_{eff})$ is given by

$$\Omega^{(1,1)}(T_{eff}) = \frac{1}{2(k_b T_{eff})^3}\int_0^\infty \epsilon^2\sigma^1 exp\left(\frac{-\epsilon}{k_b T_{eff}}\right)d\epsilon\ , \tag{2.5}$$

where σ^1 is the momentum-transfer (diffusion) cross section

$$\sigma^1 = 2\pi\int_0^\pi (1-cos\theta)\sigma(\epsilon,\theta)sin\theta d\theta \tag{2.6}$$

and ϵ and θ are the kinetic energy and scattering angle, respectively, for an ion-neutral collision in the center-of-mass system, and $\sigma(\epsilon,\theta)$ is the differential cross section for elastic scattering, a quantity which can be calculated from the ion-neutral interaction potential. For a fixed value of T_g and the ratio E/N, the mobility μ varies inversely with N. It is conventional to normalize the mobility to the Loschmidt number N_0 and refer to it as the reduced mobility μ_{red}

$$\mu_{red} = \frac{v_d}{(E/N)N_0} = \mu\left(\frac{N}{N_0}\right). \tag{2.7}$$

An extensive survey of experimental data on μ_{red}, T_{eff} and $\Omega^{(1,1)}(T_{eff})$ for positive ions in helium gas over a wide range of E/N and T_g can be found in the references [39, 40, 41, 122]. The central concern of this project is the helium ion mobility in helium gas, as it plays a key role in the recombination coefficient. The ratio E/N for a cryogenic noble gas ion catcher is less than 10 Td where the positive ions are mostly in thermal equilibrium with the neutral helium atoms. A weakly ionized helium gas contains He^+ ions and ionized helium clusters He_n^+, where n = 2,3,4 etc. The proportions of different species depend on T_g and E/N. He^+, He_2^+ and

He_3^+ are the dominant ionic species within the parameter range of cryogenic noble gas ion catchers and their reduced mobilities μ_{red} vary between 10 $cm^2\,V^{-1}\,s^{-1}$ and 20 $cm^2\,V^{-1}\,s^{-1}$. A detailed description of the formation of helium ionic species can be found in Section 2.5 and References [35, 54, 86].

2.3 Charge recombination

Stopping and thermalization of high-energy ion beams in a noble gas ion catcher causes ionization of the gas. The recombination of electrons and positive ions in the presence of neutral atoms is an important mechanism which determines the efficiency of a noble gas ion catcher. In the noble gas ion catcher we are dealing with a weakly ionized gas rather than a fully stripped plasma. The evolution of the electron-ion density in the gas cell is of importance as it influences the neutralization of the ions of interest, the extent of the penetration of the applied electric field in the ionization region, which is necessary for the extraction of the ions of interest and possible space-charge effects. The electron-ion density in a gas cell is determined by the balance between charge creation by the incoming beam and charge recombination. Most of the ions present in the gas cell are helium ions and the recombination process is dominated by the helium recombination coefficient. For thermalized ions three-body recombination causes neutralization. A detailed discussion of the recombination process in room temperature noble gas can be found in articles by Huyse et al. and Facina et al. [43, 44, 60]. This section is dedicated to the discussion of ion-electron recombination processes within the context of cryogenic noble gas ion catchers.

2.4 Recombination loss factor

The recombination loss factor f is a useful parameter to represent the figure of merit of a noble gas ion catcher. The recombination loss factor is the fraction of ions recombining in the ionization region. The efficiency for ion extraction from the ionization region is thus $(1 - f)$. The recombination loss factor f in a parallel plate ionization chamber can be estimated as [27, 60, 98]

$$f = \frac{Q\alpha d^2}{6\mu_+\mu_- E^2}\,, \tag{2.8}$$

where Q is the ionization rate density (helium ion-electron pairs $cm^{-3}\,s^{-1}$), d is the distance between the plates, α is the ion-electron recombination coefficient, μ_+ is the positive ion mobility, μ_- is the electron mobility and E is the electric field present in the ionization region. It is important to note that Equation 2.8 holds true only as long as f is small [98]. Within the noble gas ion catcher context, d is the lenght of the ionization region along the direction of applied electric field. The ion-electron

recombination coefficient α will be discussed in forthcoming sections. Electron and positive ion mobilities in cryogenic helium gas are discussed in previous sections. As the mobility of electrons is 3 - 4 orders of magnitude higher than that of positive ions, a positive ion cloud essentially exists in the ionisation region. The applied electric field pushes the ions, removing them from the ionization region. The equilibrium between the ionization of the helium gas and the removal of positive ions results in a steady state positive charge density. This positive ion cloud induces a voltage V_{ind} shielding the applied field (i.e. decreasing the effective field)

$$V_{ind} = \sqrt{\frac{eQ}{4\epsilon_0\mu_+}}d^2 \,, \tag{2.9}$$

where e is the electric charge and ϵ_0 the permittivity of the vacuum. As the beam intensity increases, the induced voltage increases. The resulting decrease in the effective field slows down the removal of ions from the ionisation region, enhancing the positive charge density and the induced voltage. Due to this positive feedback mechanism one expects a quick increase in induced voltage with increasing beam intensity up to the point where the effective field becomes zero. In this situation ions will drift out of the cloud into a region where the applied field transports them. Once the effective electric field becomes small enough, electrons are no longer effectively removed from the ionization region causing an increase in neutralization. The only way to overcome this bottleneck is to apply higher electric fields.

2.5 Helium ion species

A large fraction of the energy loss of energetic ions in helium gas goes towards the ionization of helium atoms. On average, 40 eV is needed to create a helium ion-electron pair; less than twice the ionisation energy of 24 eV. Depending on temperature, pressure and electric drift field, the He^+ ions will be transferred to ionized helium clusters He_n^+. The binding energy of He_2^+ is 2.5 eV; that of He_3^+ is 0.17(3) eV [85]. He_4^+ is considered very unstable. In this sense, He_2^+ and He_3^+ are more molecules than clusters, whereas He_n^+ with $n \geqslant 4$ is a true cluster in the sense that it is kept together by van der Waals forces. At room temperature, He^+ is the dominant ion below 1 mbar; above 5 mbar, He_2^+ is dominant. Patterson [85], shows in measurements up to a helium pressure of 40 mbar that He_3^+ starts to form below 200 K and becomes the main ion at about 120 K. Gerber and Gusinow [49] establish that He_3^+ is dominant at 76 K, 1 ms after an electric discharge for densities above about 3×10^{17} cm^{-3}. Delpech and Gauthier [33] suggest that the dominant ion at 4.2 K is He_3^+.

The temperature dependence of the reaction rate coefficient for the dimerisation of helium ($He^+ + 2He \rightarrow He_2^+ + He$) is $k = 3.53 \times 10^{-29}\, T_g^{-1}$ cm^{-6} s^{-1}, measured between 77 K and 449 K at a helium atomic density of 1.8×10^{17} cm^{-3} and from 5 to

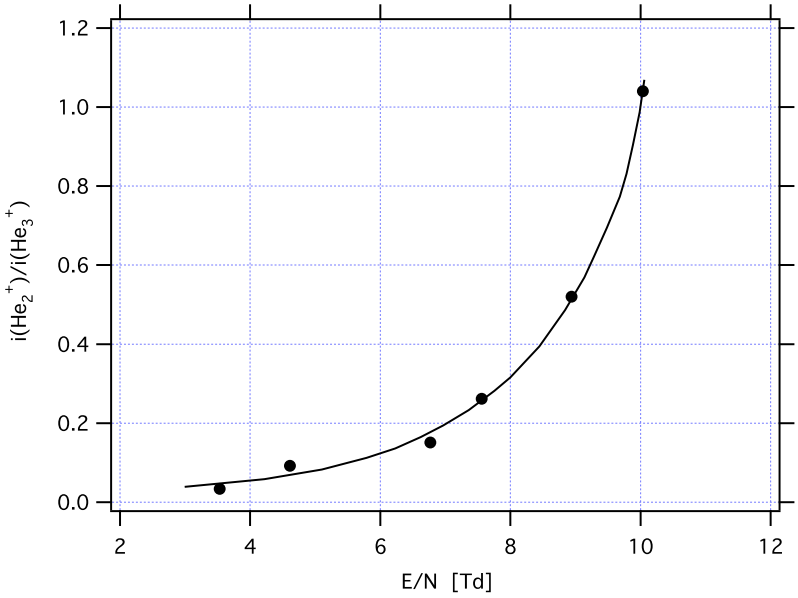

Figure 2.7: *Ion current ratio (iHe_2^+)/$i(He_3^+$) as a function of E/N at 76 K and 1.3 mbar (1.09×10^{17} cm^{-3})[54].*

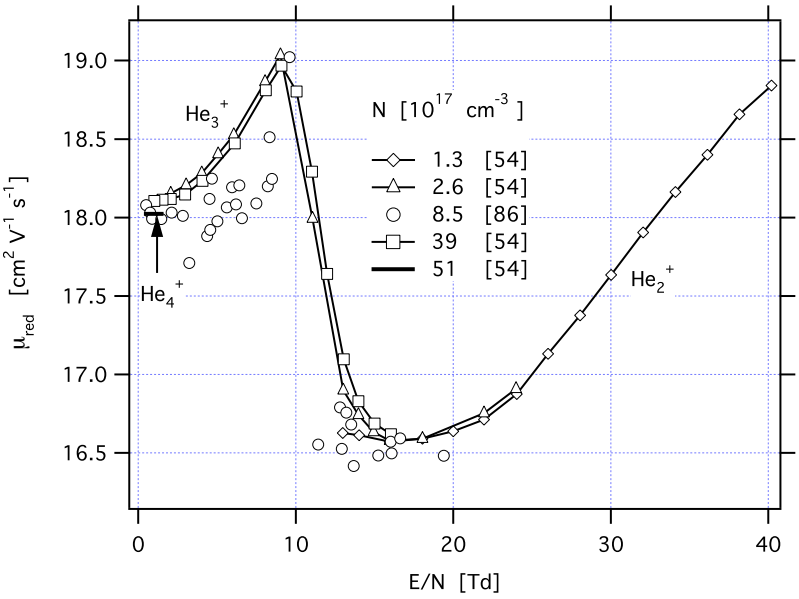

Figure 2.8: *The observed reduced mobility μ_{red} corresponding to an equilibrium mixture of He_2^+, He_3^+ and He_4^+ as a function of E/N at 77 K for four values of neutral densities [54, 86].*

13 mbar at a temperature of 300 K [79]. One should note here that this work [79] was not aware of the existence of He_3^+; the results may therefore very well represent a sum of He_2^+ and He_3^+. This gives a dimer formation half-life $t_{1/2} = \ln 2/kN^2$ of 8 ns at 300 K and of 2 ns at 77 K for a helium atomic density $N = 2.71 \times 10^{19}$ cm^{-3}. At 76 K, the conversion $He_2^+ + 2He \rightarrow He_3^+ + He$ is faster than $He^+ + 2He \rightarrow He_2^+ + He$ [49]. The conversion frequency of the latter is $1.44(14) \times 10^{-31} N^2$ s^{-1}, causing a dimerisation life time of 6 ns at $N = 2.71 \times 10^{19}$ cm^{-3}, in fair agreement with the value given above. At 76 K, the intensity ratio $i(He_2^+)/i(He_3^+)$ is less than $10^{13}\ N^{-1}$ [54]; He_3^+ is thus dominant at all densities relevant for this work.

Helium ion clusters moving at high speed due to an electric drift field can be destroyed for high E/N. Patterson reports that at 76 K and $N = 1.6 \times 10^{17}$ cm^{-3}, He_3^+ ions are mostly intact up to $E/N = 6$ Td, yet mostly destroyed in collisions at $E/N \gtrsim 13$ Td as they are electrically heated. Figure 2.7 shows the rapid increase in the breakup of He_3^+ at about 9 Td at a temperature of 76 K. Figure 2.8 shows the E/N dependence of the observed reduced mobility of molecular helium in helium at 77 K [54]. The same author deduces that He_2^+ is dominant for $(E/N)/N > 6 \times 10^{17}$ Td cm^3.

2.6 Recombination coefficient of helium ions

Let us first consider the recombination of helium ions in helium gas. A good overview of this subject is given by Dutton [36]. In general, the recombination coefficient depends on temperature and density of the electrons, of the ions and of the neutral gas particles. These temperatures and densities are often interrelated. We focus our discussion here on the situation with low electron density ($< 10^{11}$ cm^{-3}) and rather high pressure (> 10 mbar). We look at the recombination of He_2^+ and He_3^+. The main recombination reactions are

2-body: $He_n^+ + e^- = He_{n-1}^* + He$

and

3-body: $He_n^+ + e^- + He = He_{n-1}^* + 2He$.

The 2-body reaction is characterised by the recombination coefficient or rate constant α_2 (in cm^3 s^{-1}); the 3-body reaction by the recombination coefficient α_3 (in cm^6 s^{-1}). The total recombination coefficient is given by

$$\alpha = \alpha_2 + N\alpha_3 \tag{2.10}$$

where N is the atomic density of the gas. Early work did not take a strong source of electrons from penning ionization (ionization in metastable-metastable collisions) into account and thus measured an effective recombination coefficient. If a strong electron source is present, the recombination coefficient appears smaller. Such

electrons are driving these reactions involving helium ions and metastable helium atoms. The true or actual recombination coefficient can be five times larger [61].

R. Deloche et al. [32] measure the recombination of He_2^+ at room temperature and pressures from 7 mbar to 130 mbar. Five different diagnostic tools, i.e. X-band microwave interferometry, X-band microwave radiometry, mass spectrometry, optical absorption spectrometry and optical emission spectrometry are used to measure the decay time of attenuation and phase-shift of the wave crossing the plasma branch, radiation temperature of ionized gas, atomic- and molecular-ion currents, density of atomic and molecular metastables and decay time of excited atomic and molecular populations. They interpret the data with a mathematical model including all known elementary processes as a set of coupled partial differential equations. In this way, the rate coefficients of all significant mechanisms are measured simultaneously such that the complex correlation between ion, metastable and electron concentration is taken into account. In Deloches' work the ion temperature is equal to the gas temperature, while the electron temperature is not. The resulting recombination coefficient for He_2^+ is:

$$\alpha = (\alpha_c + k_0 N)(T_e/293)^{-x} + k_e n_e (T_e/293)^{-y} , \tag{2.11}$$

where N is the helium density (cm^{-3}), T_e is the electron temperature (K), n_e is the electron density (cm^{-3}), $\alpha_c < 5 \times 10^{10}$ $cm^3\,s^{-1}$, $k_0 = 5(1) \times 10^{-27}$ $cm^6\,s^{-1}$, $k_e = 4.0(5) \times 10^{-20}$ $cm^{-3}\,s^{-1}$, $x = 1(1)$ and $y = 4.0(5)$. Johnson and Gerardo [62] measure the recombination coefficient for an electron temperature equal to the gas temperature of 300 K to be $\alpha = 1.1 \times 10^{-8} + 1.2 \times 10^{-26} N$ $cm^3\,s^{-1}$ for $4.8 \times 10^{17} < N < 1.8 \times 10^{18}$ cm^{-3}. Assuming an electron temperature equal to the gas temperature and an electron density below about 10^{11} cm^{-3} (such that the electron-density dependent term in (Equation. 2.11) can be neglected), we can compare the results of [32] and [62]: for a helium pressure of 100 mbar to 1000 mbar, the two results agree within a factor of about 3. Collings et al. [26] measure recombination of He^+ at 2.5 and 60 mbar (it is not clear if He^+ is singled out, or if in fact He_2^+ was measured at 60 mbar). At 60 mbar, they obtain $\alpha = 1.8 \times 10^{-20}$ $n_e (T_e/300)^{-4.4}$ $cm^3\,s^{-1}$. The terms depending on the electron density from [32] (see Equation 2.11) and [26] are the same within a factor of about 2.

As mentioned above He_3^+ is the dominant ion at low temperatures. Gerardo and Deloche [49, 33] show that the recombination coefficient of He_3^+ at low temperature is much higher than that of He_2^+ at room temperature. Gerardo and Gusinow measure the recombination coeffcient for $T_g = T_e = 80$ K to be $3.4 \pm 1.4 \times 10^{-6}$ $cm^3\,s^{-1}$, and show an electron temperature dependence T_e^{-a}, with $0.98 < a < 1.60$. Delpech and Gauthier [33] measure at a gas temperature of 4.2 K and a helium density of 1.7×10^{17} cm^{-3} to 28.7×10^{17} cm^{-3}, while varying the electron temperature from 10 to 200 K. They obtain a recombination coefficient $= 4.0(6) \times 10^{-4}/T_e$ $cm^3\,s^{-1}$. This was later verified for $T_e \leqslant 100$ K by [92]. For $T_e = 80$ K, this result agrees with [49], indicating that not the gas temperature, but the electron temperature is the relevant parameter. In cryogenic plasmas, hot electrons play thus a dominant role as the

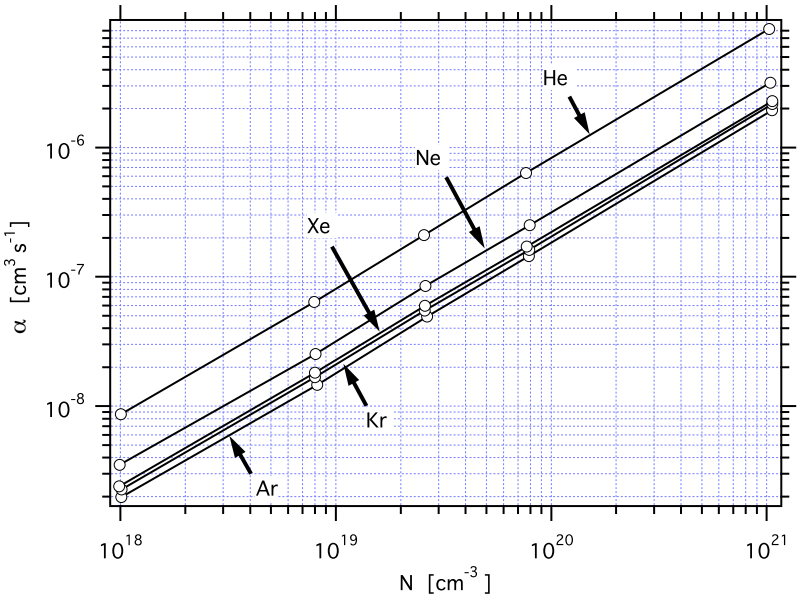

Figure 2.9: *Collisional radiative recombination rate coefficient α for rare gases recombining in helium as a function of helium density N [129].*

electron temperature is often much larger than the gas temperature. Hot electrons (14 - 20 eV) are created in the formation of He^+ and He_2^+ ions and the penning ionization of metastable helium atoms. The experimental results are compatible with an electron temperature dependence of $\alpha(\ He_3^+) \propto T_e^{-1}$. Ion-electron recombination in helium as a function of gas temperature and pressure is measured by [118] for 200 K, 235 K, 275 K and 295 K and over a wide pressure range from 50 mbar to 1200 mbar. This pressure range is relevant for our work, contrary to many other investigations, where pressures are mostly below 50 mbar. The recombination coefficient α_2 has a linear temperature dependence in this pressure range. A fit weighted with the experimental errors of α_3 as a function of T_g yields $\alpha_3 \propto T_g^{-2.94}$, a weighted fit of $\ln(\alpha_3)$ as a function of $\ln(T_g)$ gives $\alpha_3 \propto T_g^{-2.54}$, very close to the $T_g^{-2.5}$ dependence predicted by many theoretical approaches [12, 87, 114]. Because of this, we prefer the latter result. In the fit, the two parameters, scaling and temperature exponent are strongly correlated. The total recombination coefficient is:

$$\alpha = -0.73 \times 10^{-7} + 6.0 \times 10^{-10}\, T_g + 3.6 \times 10^{-21}\, T_g^{-2.5} N\ . \tag{2.12}$$

The experimental error on α_2 is $\sim$10% and on α_3 is $\sim$10 - 20%, so we assume that Equation 2.12 has an error of $\sim$20%. For 293 K, assuming $T_e = T_g$ and n_e is small, this formula is in excellent agreement with the above mentioned result of [32]. It is interesting to note that Cao and Johnson [19] measured a $T_g^{-2.9}$ dependence for the recombination of simple molecular ions (mainly O_2^+, N_2^+) with electrons in helium

at densities 2.5×10^{19} to 2.9×10^{20} cm^{-3} and gas temperatures of 77 K, 125 K and 150 K.

2.7 Recombination of noble gas ions in helium

As this work is mostly concerned with the survival and transport of radon ions in helium, we here summarize the knowledge on the relevant recombination coefficient. Whitten et al. [129] calculate the recombination coefficient for noble gas ions X^+ recombining in helium, $X^+ + e^- + He \rightarrow X^* + He$, for a temperature of 300 K and helium densities from 10^{18} to 10^{21} cm^{-3}. The calculations are validated by comparing them with experimental results of He_2^+ recombining in helium. The calculation is within a factor of 3 from the measurements, which amongst themselves show a variation of the same order. As the values for Ar, Kr and Xe are very close to each other one can expect that radon will have a very similar value (Figure 2.9) i.e. $\alpha = 2.0\times10^{-27} N$ cm^3 s^{-1}.

2.8 Conclusion

This chapter presents a literature survey on relevant physical processes in a cryogenic helium gas ion catcher. Most of the physical processes involved in cryogenic ion catchers fall within the classical and elastic collision limit. The positive ion mobility is an important parameter determining the efficiency of the extraction of ions from such a device as it determines the extraction time of ions from the stopping volume. At the typical helium densities in noble gas ion catchers He_2^+ is the dominant ion in ionised helium gas above a temperature of about 200 K. Below this temperature He_3^+ is dominant. The typical electric field to density ratio considered here is not large enough to induce breakup of He_3^+.

The main ion-loss mechanism in a cryogenic helium gas ion catcher is the recombination loss. Recombination of thermalized ions has a negative impact on the total extraction efficiency, whereas helium ion recombination acts as a positive factor as it decreases the space charge problem associated with the ion beam and removes the electrons that could otherwise neutralize the ions of interest. The recombination coefficient of helium ions shows a temperature dependence of $T_g^{-2.5}$ which is characteristic for the 3-body recombination coefficient α_3. The same temperature behaviour is observed for simple molecular ions in helium down to 77 K. Recombination shows an electron temperature dependence of T_e^{-1} which in turn depends on the ionization method and can be much higher than the gas temperature.

3 Physics processes in superfluid helium ion catchers

Helium has two stable isotopes ^{4}He and ^{3}He. Though ^{3}He has the same chemical nature as ^{4}He, the lighter mass of ^{3}He and the fact that ^{3}He is a fermion result in markedly different behavior. Helium was first liquefied by Kamerlingh Onnes in 1908 for which he won a Nobel Prize in 1913. This work deals with the properties of ^{4}He, and unless specifically stated, it should be assumed that ^{4}He is the isotope being discussed and that parameters are given at saturated vapor pressure.

When liquid helium is cooled to 2.172 K, it undergoes a phase transition. Because of the characteristic profile of the heat capacity curve (see Figure 3.1), the temperature at which the transition takes place is called the lambda temperature T_λ. There is no specific volume change or latent heat involved in the lambda transition. In 1938, P. Kapitza [63] and independently J. F. Allen and A. D. Misener [1] reported the zero viscosity of liquid helium below T_λ. Unlike most fluids, liquid helium below T_λ behaves as a non-Newtonian fluid. It was Kapitza who introduced the term "superfluid" helium to describe the unusual behavior of helium below T_λ. The quantum-mechanical nature of the superfluid helium introduces properties which cannot be explained with a classical treatment.

To account for this unique behavior, F. London [68] suggested that as a single ^{4}He atom is a boson, a large collection of ^{4}He atoms can form a Bose-condensate-like state. Although London was right, experimentally it was very difficult to prove. In the mean time another theory known as the two-fluid model was introduced by L. Tisza [115] and L. Landau [66]. The 2-fluid model postulates that the superfluid helium is composed of two inseparable inter-penetrating fluids, one component being referred to as the normal fluid and the other component as the superfluid. Due to the simplicity and excellent agreement with experimental results, the two-

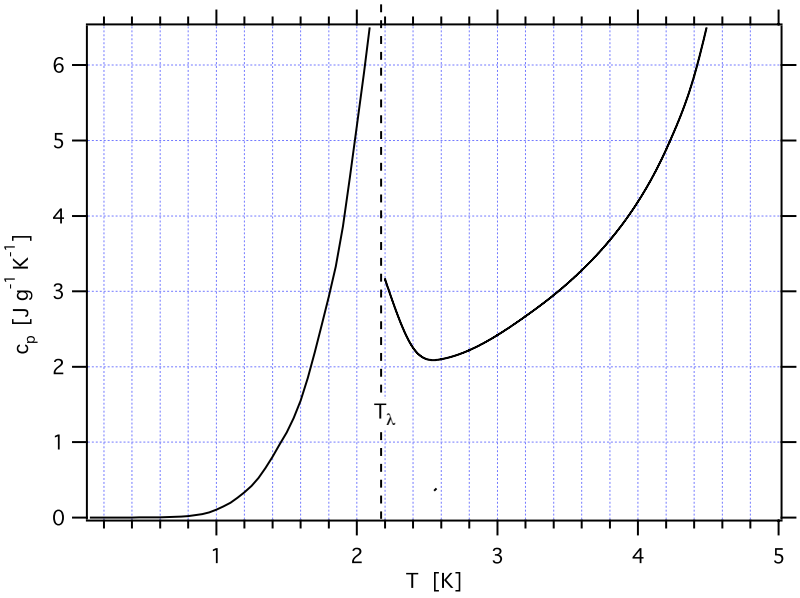

Figure 3.1: *Specific heat capacity c_p of liquid helium at saturated vapor pressure as a function of temperature T [14].*

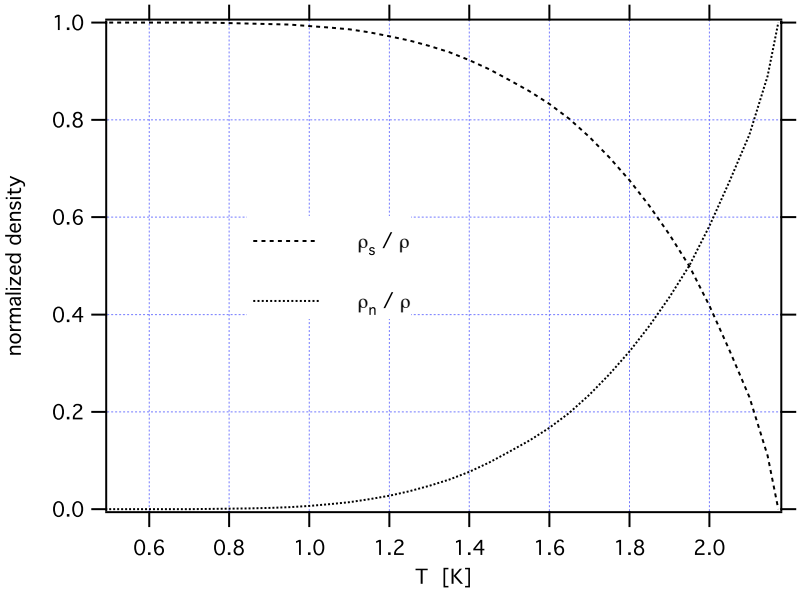

Figure 3.2: *Relative density of the normal and superfluid components in superfluid helium as a function of temperature T [14].*

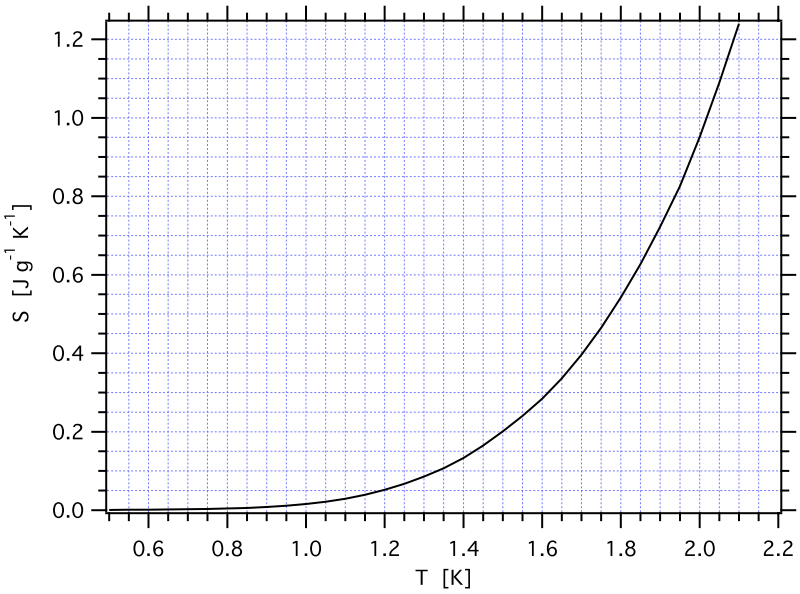

Figure 3.3: *Entropy S of superfluid helium as a function of temperature T [14].*

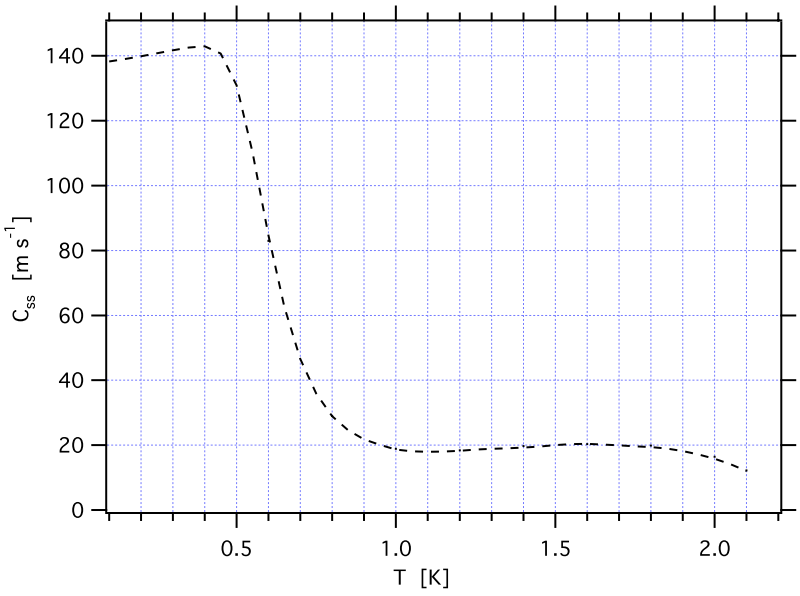

Figure 3.4: *Second sound velocity C_{ss} as a function of temperature T [14].*

fluid model has dominated the scene for the last 70 years. According to the two-fluid model the density of the superfluid component is given by

$$\rho_s = \rho \left(1 - \frac{T}{T_\lambda}\right)^{5.6} , \tag{3.1}$$

$$\rho = \rho_s + \rho_n , \tag{3.2}$$

where ρ is the effective density of the superfluid helium, ρ_s is the density of the superfluid component and ρ_n is the density of the normal component. The effective superfluid density $\rho = \rho_s$ at T = 0 K and $\rho = \rho_n$ at T = T_λ (see Figure 3.2). The superfluid component is thought to have no entropy and no viscosity. One of the most interesting characteristics of superfluid helium is the ability to transmit more than one type of sound. In addition to ordinary or first sound which is a density variation brought on by a local pressure gradient, there is a second sound which is the propagation of a thermal wave as a result of fluctuations in the local entropy. The first sound results in a compression shock wave, whereas the second sound results in a thermal shock wave. The characteristic feature of these sound waves can be explained on the basis of the two-fluid model. The velocity of the second sound is given by the Tisza-Landau thermodynamic expression [31]

$$C_{ss}^2 = \left[\left(\frac{\rho_n}{\rho}\right)^{-1} - 1\right] \frac{TS^2}{c_p} , \tag{3.3}$$

where T is the temperature, S the entropy (see Figure 3.3) and c_p the specific heat capacity (see Figure 3.1) of the superfluid helium. Figure 3.4 shows the second sound velocity C_{ss} as a function of temperature. A detailed discussion of the two-fluid model is outside the scope of this work, however there are excellent references on the subject [67, 69, 97].

Helium atoms are nonpolar, stable and spherically symmetric. They have a very low electric polarizability (2.04×10^{-25} cm^3). Charged particles introduced into superfluid helium will interact with the helium atoms to form various complexes. This chapter gives an overview of the properties of electrons and positive ions in superfluid helium which are relevant to this work.

3.1 Positive ions in superfluid helium

Charged particles in superfluid helium will introduce a polarization interaction with the ambient helium. An ion produces a strong field in its vicinity and the potential energy experienced by the polarizable medium results in an electrostrictive increase in the local density. A solid layer of helium atoms forms around positive ions because the pressure produced by the electrostrictive interaction of positive ion and the ambient medium is larger than the melting pressure for helium.

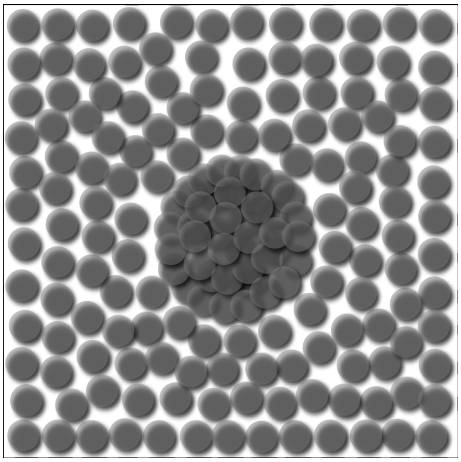

Figure 3.5: *Schematic representation of a snowball.*

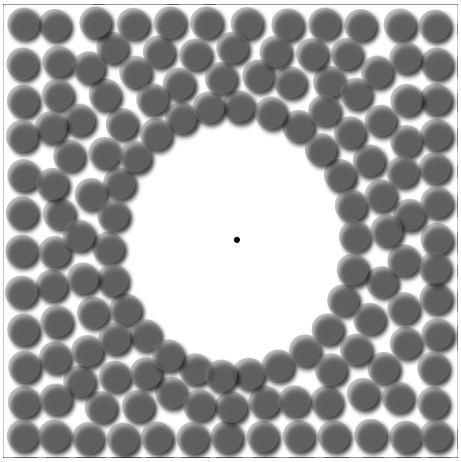

Figure 3.6: *Schematic representation of a bubble.*

This quasimacroscopic entity of a positive ion and the helium solidification region around is called a "snowball" (see Figure 3.5). Atkins [7] put forward a simple model to explain this phenomenon. In this model, the ion complex is taken to be a solid helium sphere surrounding the positive ion core. This structure arises because of the induced dipole attraction between the core ion and a helium atom. In Atkins' model the snowball radius R_{sb} is given by

$$R_{sb} \simeq \frac{V_s}{(V_l - V_s)} \frac{2\sigma_{ls}}{(P_m - P_a)} \ , \tag{3.4}$$

where P_a is the ambient pressure of the liquid helium far from the ion, P_m is the melting pressure of solid helium ($\approx$25 bar), V_s (=27.6 cm^3 mole^{-1}) and V_l (=21 cm^3 mole^{-1}) are the molar volume of liquid and solid helium, and σ_{ls} (=1.35 $\times 10^{-4}$ N m^{-1}) is the solid-liquid surface tension for helium. In Atkins' model the snowball radius R_{sb} is a function of the ion charge q and is roughly 0.6 - 0.7 nm for singly charged ions (Figure 3.7). The effective hydrodynamic mass of a spherical shape of radius R_{sb} in a fluid of mass density ρ is given by

$$M_{hydro} \ = \ \frac{2}{3} \pi R_{sb}^3 \rho \ . \tag{3.5}$$

This results in a snowball mass of ion mass plus 40 to 60 helium masses. Deviations from Atkins' model have been observed for different ionic species.

A more rigorous model which takes into account the direct interaction with the central ion's valance electrons, an interaction associated with the absence or excess of helium near the core ion and a van der Waals interaction can be found in later literature [25, 50]. Nevertheless, Atkins' model retains its significance as a

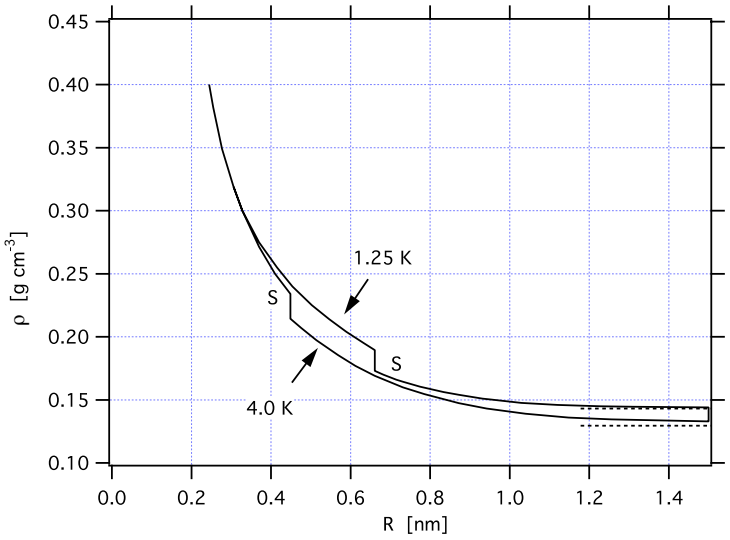

Figure 3.7: *Variation in the density ρ of liquid helium near a localized point charge [7]. Dotted lines show the bulk liquid helium densities at corresponding temperatures.*

first approximation and can be used to estimate the scale of various effects. It is important to note that heavy alkali-earth ions form bubbles in contrast to the other positive ions (see Section 3.3).

3.2 Electrons in superfluid helium

The electron in superfluid helium forms a structure which cannot be described by Atkins' model. The helium atom is a stable quantum system, which cannot accommodate a surplus electron at distances of the order of Bohr's orbit ($a_0 = 0.529 \times 10^{-10}$ m) and the interaction between the electron and neighboring helium atoms is of a very strong repulsive nature at short range (Pauli repulsion). A long-range attractive interaction arising from the electrostrictive polarization of the atoms is also present. When a free electron is injected into superfluid helium and forced to move in the interatomic spaces, it experiences a repulsive potential of about 1 eV and as a result is energetically favorably localized within a spherical cavity from which the helium atoms are completely excluded, a so-called bubble (Figure 3.6). In the representation of the bubble-helium interaction, we can treat helium as a continuous medium rather than as discrete atoms. The balance between the electron zero point energy, the surface energy of the liquid and the pressure-volume energy determines the bubble size. As a first approximation the bubble

energy can be expressed as [24]

$$E = \frac{h^2}{8mR_b^2} + 4\pi R_b^2 \sigma_s + \frac{4}{3}\pi R_b^3 P_a \ , \tag{3.6}$$

where R_b is the bubble radius, m is the electron mass, σ_s $\sim$3.7$\times 10^{-4}$ N m^{-1} is the surface energy per unit area and h is Planck's constant. At zero pressure the radius at which the energy has a minimum is

$$R_b^{min} = \left(\frac{h^2}{32m\pi\sigma_s}\right)^{1/4} . \tag{3.7}$$

This radius is 1.9 nm at 0 K and increases slightly as the temperature goes up. It is important to note that the polarization-induced electrostrictive forces which lead to the snowball formation in the case of positive ions will not play a role in electron bubble formation as $R_b \gg R_{sb}$. As the electron mass is negligible, the effective mass of an electron bubble is the hydrodynamic mass (Equation 3.5) of 243$\pm$5 helium masses [99]. Similar to electrons, negative ions and heavy alkali earth positive ions form bubbles [46].

3.3 Snowball and bubble mobility

A direct implication of snowball or bubble formation by charged particles in superfluid helium is their smaller mobility compared to expectation for the bare positive ions or electrons. The mobility of ions in superfluid helium shows a wide variety of phenomena with strong and striking temperature and electric field dependencies. As the mobility depends mainly on the size of the entity in movement, both snowballs and bubbles show fairly similar mobility profiles. The differences can be explained by differences in size and structure, the positive ion being a high density complex of about 0.6 - 0.7 nm diameter and the electrons being a low density complex of about three times this dimension. At temperatures below about 0.6 K the mobility of snowballs and bubbles is limited mainly by collisions with thermal phonons [95]. At temperatures above about 0.8 K, snowball-roton and bubble-roton collisions start to play a major role in limiting the mobility. A roughly exponential temperature dependence of the mobility reflects the exponential population of roton states. In the "kinetic regime" ($0.8 \lesssim T \lesssim 1.7$ K) roton-roton scattering can be neglected, while above about 2 K, roton-roton scattering is so frequent that the rotons appear to the ions as a viscous fluid [10]. In the "kinetic regime" the zero-field ($E \ll 1$ V cm^{-1}) mobilities of snowballs and bubbles show a temperature dependence of the form

$$\mu_0 \propto e^{\Delta_\pm / k_B T} \ , \tag{3.8}$$

where the value of Δ_+/k_B is around 8.65 - 8.8 K and that of Δ_-/k_B is around 7.7 - 8.1 K [89] (Figure 3.8). Figure 3.9 gives an overview of the behaviour of the snowball

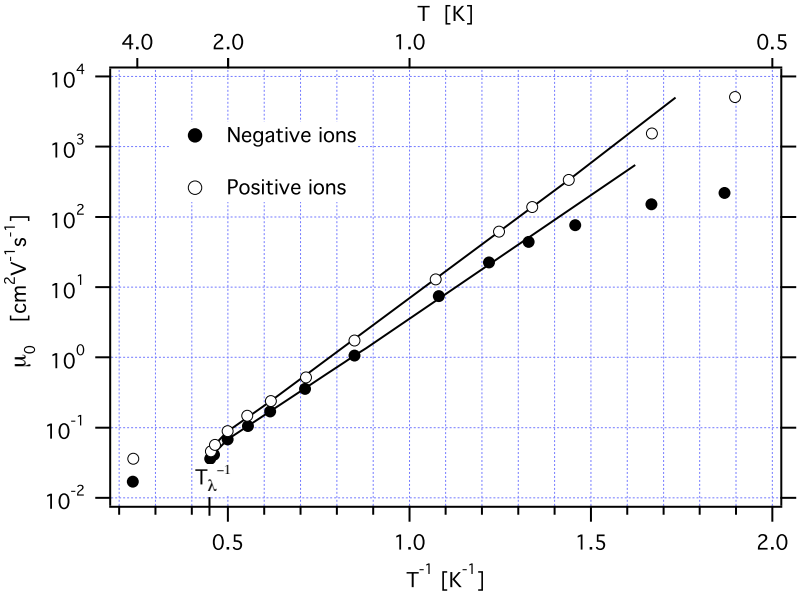

Figure 3.8: *Zero field mobilities μ_0 of positive ions and electrons in liquid helium as a function of inverse temperature $1/T$ [89].*

and bubble drift velocity v_d as function of applied electric field. The drift velocity v_d is proportional to the electric field (i.e. the mobility is constant) up to 200 V cm^{-1} [73]. At higher velocity, the mobility decreases due to the enhanced density of rotons in the disturbed region near the snowball or bubble, giving rise to an increased drag force. At an electric field E_g and a drift velocity v_g a transition from a bare snowball or bubble regime to a snowball or bubble-vortex ring regime occurs: the snowball or the bubble produces vortex rings and is captured by them. A further increase in vortex energy (by an increase in electric field) results in an increase in its radius causing v_d to fall to a minimum value. The snowball is much smaller than the electron bubble and therefore much less tightly bound to its vortex ring, thus the thermally activated escape rate of the snowball from the vortex ring is large. The electron bubble is strongly bound to the vortex ring up to temperatures of at least 1.8 K, whereas the escape probability from the vortex ring for the snowball is already large at a temperature of about 1 K. Because of this, the drift velocities of bubbles and snowballs show a different behaviour for electric fields above E_g. As the energy (i.e. electric field) increases further, the vortex will be gradually shed from the snowball; the drift velocity increases and reaches a saturation value v_r equal to v_g within experimental errors (see Figure 3.9). This saturation occurs when the snowball creates vortex rings continuously without being trapped. The discontinuity in drift velocity above E_g becomes less and less deep with an increase in

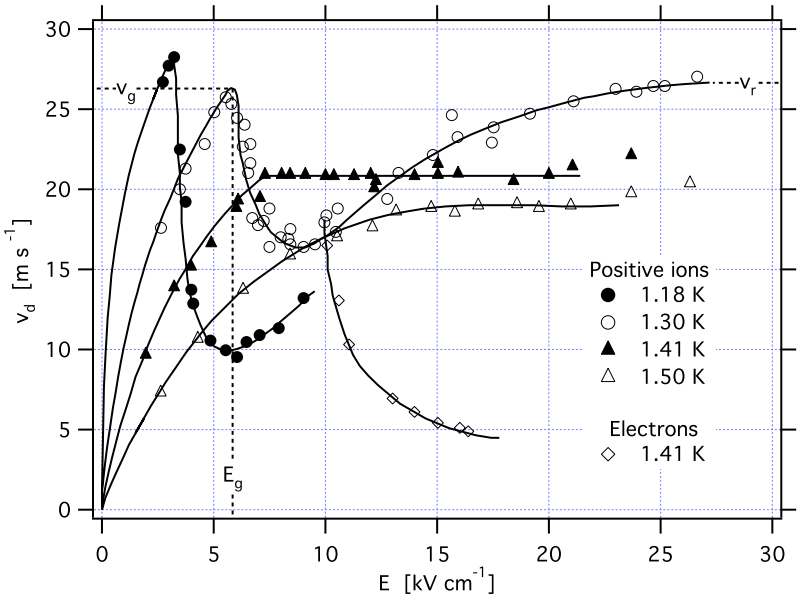

Figure 3.9: *Drift velocity v_d of positive and negative ions as a function of the electric field E [17]. v_g, E_g and v_r are indicated for 1.3 K.*

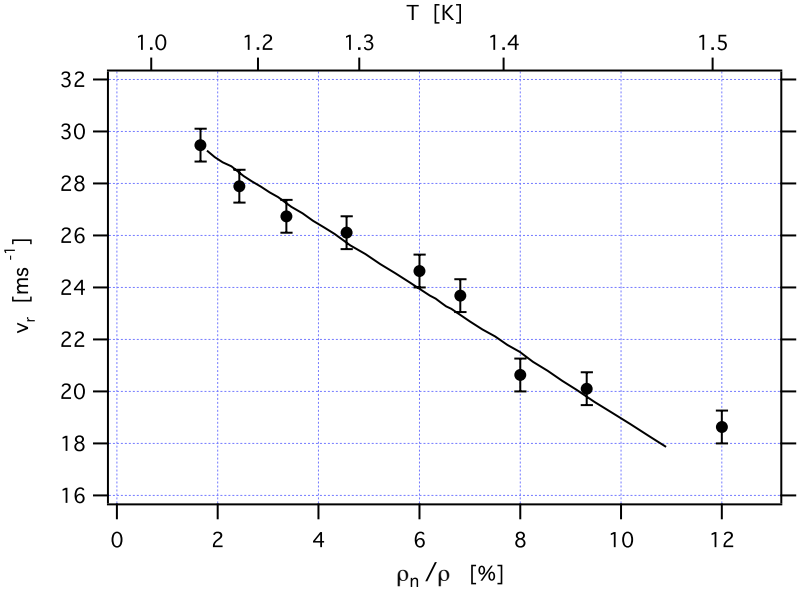

Figure 3.10: *The critical velocity v_r for the production of vortex rings by positive ions as a fucntion of normal-to-total density ratio ρ_n/ρ [17].*

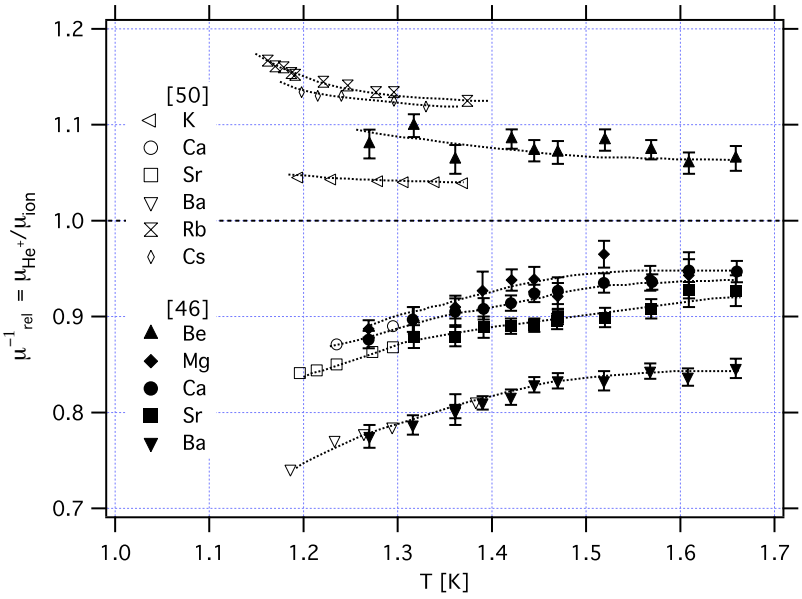

Figure 3.11: *Inverse relative mobilities $\mu^{-1}_{rel} = \mu_{He^+}/\mu_{ion}$ of positive ions as a function of temperature T. The lines are drawn to guide the eye [46, 50].*

temperature and disappears completely at about 1.35 K. The velocity v_r (measured as v_g for $T < 1.35$ K) is temperature dependent above 1 K (see Figure 3.10). A detailed study of the phenomena can be found in [17, 16, 20, 84]. In the context of this thesis, we deal with electric fields well below E_g, concerning both snowballs and bubbles. The main interest of the current project is the fast transport of positive ions in superfluid helium so it's worth to note that the snowball model proposed by Atkins has its limitation as far as a prediction for the mobility of positive impurities in superfluid helium is concerned. Mobility measurements of K^+, Rb^+ and Cs^+ ions show a mobility lower than predicted by the snowball model [13, 25, 50]. The heavier alkaline earth ions Ca^+, Sr^+, Ba^+ and Mg^+ form bubble-like defects instead of snowballs whereas the Be^+ ion form a snowball-like structures [46]. All ion mobilities fall within about 25% of the He^+ mobility (see Figure 3.11). For most practical purposes the He^+ mobility can thus be used.

3.4 Charge recombination factor in superfluid helium

G. Careri and F. Gaeta [21] measured the volume recombination coefficient α_{SF} of ions in superfluid helium in a range of 0.87 K to 2.0 K. In their experiment they sent two ionic beams of opposite charges against each other and calculated the recombination coefficient from the loss of charge suffered by each beam. They used

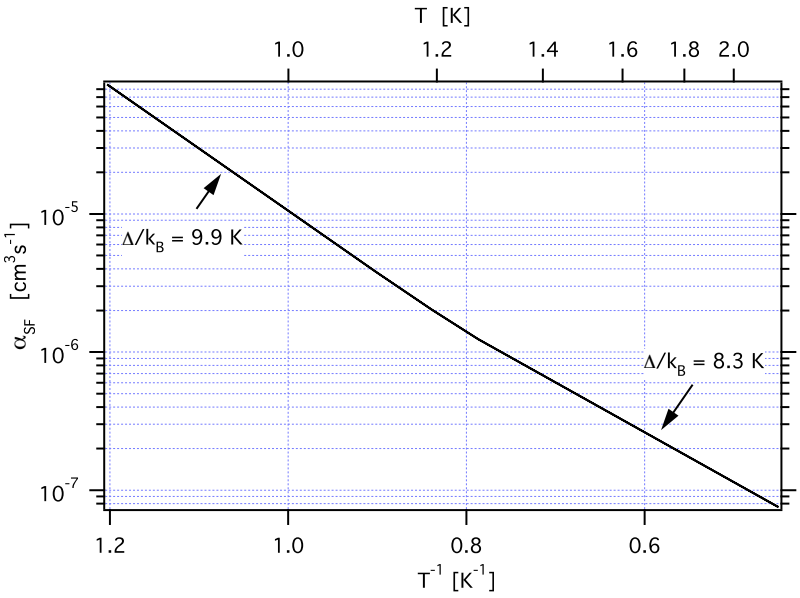

Figure 3.12: *Recombination coefficient of ions in superfluid helium α_{SF} as a function of the inverse temperature $1/T$ [21].*

α particles from a radioactive ^{210}Po source to create a 0.2 mm thick densely ionized region in liquid helium from which beams of ions are drawn out by means of an applied electric field. They observed a general behavior of exponential increase in α_{SF} with the reciprocal of the temperature. This increase is represented by

$$\alpha_{SF} \propto exp(\Delta/k_B T) \ , \tag{3.9}$$

with $\Delta/k_B = 8.3$ K between temperatures 2 K and 1.3 K and $\Delta/k_B = 9.9$ K at temperatures lower than 1.3 K. Figure 3.12 shows the recombination coefficient as a function of inverse temperature.

3.5 Positive ions at the superfluid-vapor interface

The extraction of positive ions (snowballs) from the superfluid helium surface to the vapor phase is not trivial as is that of electron bubbles [104, 105]. The electric potential barrier at the superfluid-gas interface is the bottleneck. The image charge potential model provides a simple way to look at this potential barrier. This model gives the electric potential distribution of a point charge in front of a dielectric interface. When a point charge Q is in the vicinity of a dielectric interface, i.e. of order of a few tens of nanometers, its electric field polarizes the dielectric and a bound charge density is induced at the dielectric interface. No bound charge

is created in the bulk of the medium, as the polarizing field is a Coulomb field of a point charge. The sum of Coulomb forces between the point charge and the elements of the induced surface charges acts like the Coulomb force between the point charge and its mirror image Q' [42]. The image charge potential is attractive for a charge on the low-dielectric-constant side and repulsive for the charges on the high-dielectric constant side of the interface, independent of the sign of the charge. Consider a dielectric interface between two media with the permittivities ϵ_1 and ϵ_2 (Figure 3.13). If the point charge Q is placed at a distance z from the interface, the induced image charge Q' is

$$Q' = Q\left(\frac{\epsilon_1 - \epsilon_2}{\epsilon_1 + \epsilon_2}\right) \tag{3.10}$$

and the image potential energy of a point charge Q is

$$\phi_{im}(z) = \frac{1}{4\pi\epsilon(z)}\frac{QQ'}{4z}\ . \tag{3.11}$$

This is half of the electric potential energy of a system of two real point charges due to the fact that no work is required to bring the image charge Q' from the infinity [51].

This project concerns positive ions in superfluid helium and the possibility to extract them to the vapor phase. If an electric field E is applied across the interface such that the point charge Q is pushed towards the interface, the total potential energy $\phi_{eff}(z)$ is

$$\phi_{eff}(z) = \phi_{im}(z) + QEz\ . \tag{3.12}$$

Figure 3.14 illustrates the electric potential energy of a unit point charge Q at the superfluid helium-vapor interface. It is trapped in a potential well created by the image charge potential in combination with an externally applied electric field normal to the interface. The divergence and discontinuity of Equation 3.11 at $z = 0$ shows that the method of calculating the effective potential using a discrete dielectric interface is unphysical. This divergence is removed by considering a gradual transition of permittivity between superfluid helium and vapor phase [103]. This transition is associated with the gradual change of the superfluid density to the vapor density at the interface. This transition layer is a few atomic diameters thick (Figure 3.15). A mathematical model to represent this transition is a linearly graded transition with sinusoidally rounded corners as used by Stern [103]. A numerical solution for the image charge potential energy of a unit point charge Q at an interface with such a permittivity profile (see Figure 3.15) is given by Stern (see Figure 3.16) [103]. A more realistic superfluid-vapor density transition profile is found in the experimental work of Lurio et al. [70, 71]. No significant variation of interfacial width is observed in a temperature range from 1.1 K to 1.8 K. The width of this interfacial density variation is 0.92(10) nm which is compatible with the 0.68 nm used in Stern's model. The main difference is the variation profile (see Figure 3.15).

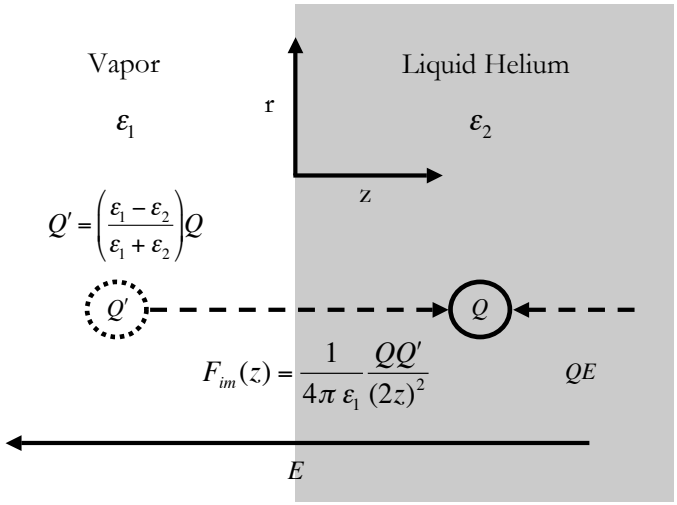

Figure 3.13: *A point charge Q and the induced image charge Q' (at the superfluid helium-vapor interface). F_{im} is the image charge force experienced by the point charge Q. QE is the electric force experienced by the point charge Q due to the applied electric field E*

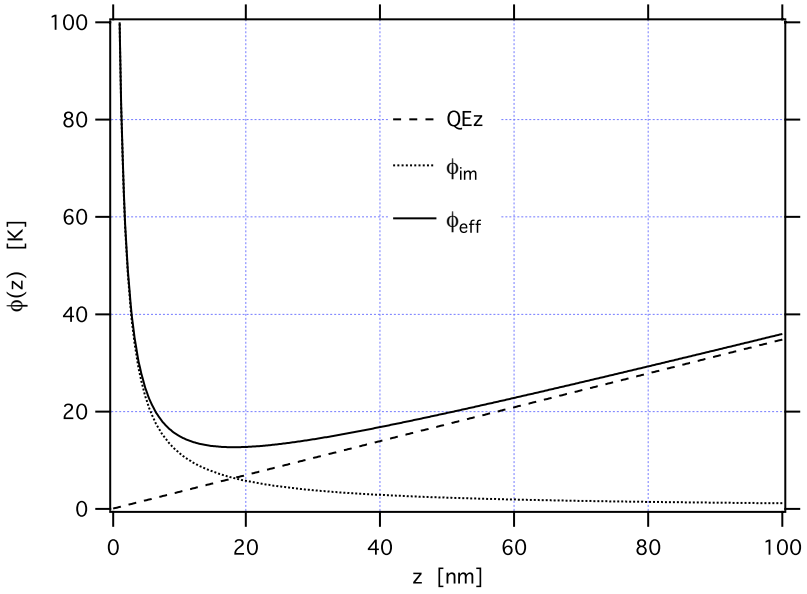

Figure 3.14: *Electric potential energy ϕ of a unit point charge Q as a function of the distance z from an abrupt superfluid- vapor helium interface. The dotted line shows the image charge potential energy ϕ_{im} of a unit point charge Q as a function of the distance z, the dashed line shows the electric potential energy of of a unit point charge Q due to the electric field $E = 300\ V\,cm^{-1}$ applied perpendicular to the interface and the solid line shows the combination of both (ϕ_{eff}).*

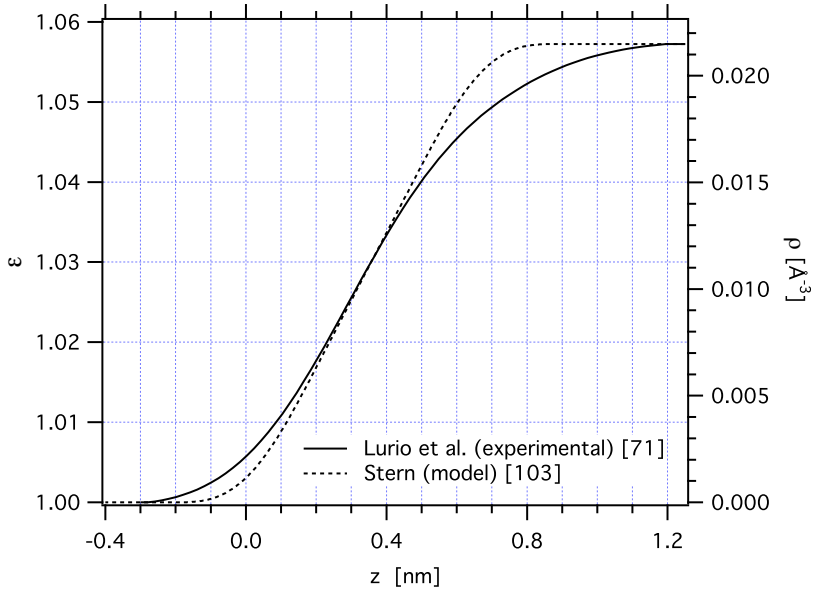

Figure 3.15: *Spatial variation of the dielectric constant ϵ and the density ρ at a superfluid-vapor helium interface. The solid line represents the experimental measurement by Lurio et al. [71]. The dotted line is the model used in Stern's potential barrier calculation [103].*

3.6 Ion extraction across the superfluid-vapor interface

3.6.1 Extraction of electrons

There has been a lot of experimental and theoretical work on the electron extraction across the superfluid-vapor interface [94, 101]. An interfacial potential energy barrier of $\sim$25 - 40 K (depending on the applied electric field) and a characteristic trapping time of 1 - 100 s have been measured for electrons [94].

Interaction of the electron and superfluid helium constitutes of two factors, the strong short-range repulsion, which arises from the requirement of the Pauli exclusion principle and a long-range attraction due to the polarization potential, represented by the classical image charge potential. It is important to note that the large potential step ($\sim$1 eV) due to the Pauli repulsion is 45 times larger than the image-charge-induced attractive potential when the electron approaches the interface from the vapor phase. Thus the Stern image charge model is insufficient to explain the interaction of electrons with the superfluid-vapor interface.

A theoretical work by F. Ancilotto and F. Toigo [5] showed that if an electric field is applied such that an electron bubble inside the liquid helium is pushed towards the superfluid-vapor interface, it is stable up to a distance $\sim$2.3 nm. If it comes closer to the surface due to thermal motion, the bubble bursts and the electron is

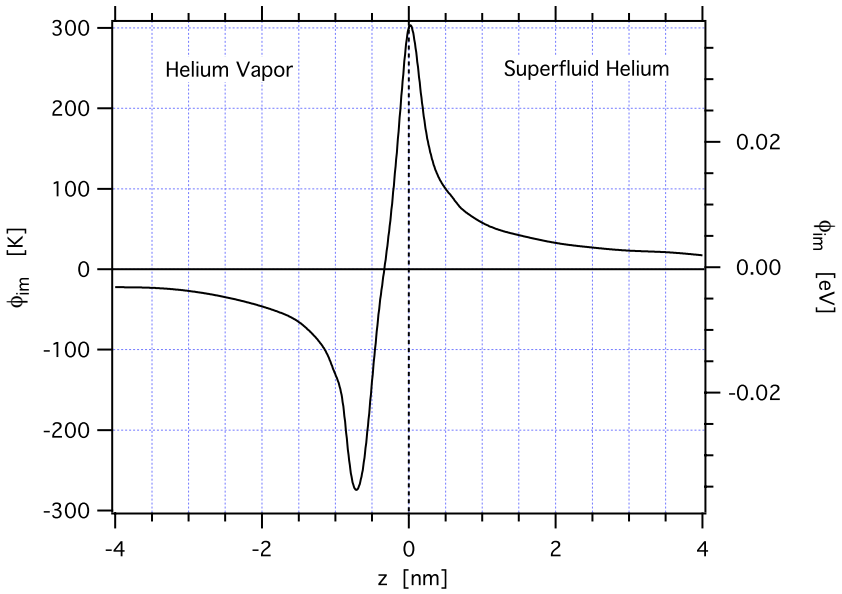

Figure 3.16: *Image charge potential energy ϕ_{im} of a unit point charge calculated for the model interface demonstrated in Figure 3.15 [103].*

ejected into the vapor. They obtained a potential energy barrier of 38 K for the thermal emission. At distances larger than $\sim$2.3 nm quantum tunneling through the surface layer dominates the extraction probability [5]. Theoretical works suggest that the diffusive nature of the superfluid-vapor interface does not play a big role in electron extraction phenomena [5, 23].

3.6.2 Extraction of snowballs

Contrary to electron bubbles, positive ion extraction is reported to be extremely weak [15, 104, 105]. There is not much information available on snowball-interface interactions in the published literature. Extraction of ^{219}Rn ions across the superfluid-vapor interface is reported by Huang et al. with an extraction efficiency of tens of percents at 1.6 K [56, 57]. There is no theoretical model available to understand positive ion extraction. In the case of snowballs, the huge mass compared to the electron, makes quantum tunneling an improbable candidate for an effective extraction mechanism. It is important to keep in mind that the structure and sizes of the electron bubbles and snowballs are very different (see section 3). The size of the snowballs is comparable to the width of the interfacial density variation and there is no repulsive force between snowballs and the ambient medium; thus in this case the diffusive nature of the interface may play an important role contrary to the electron bubble case. Stern's potential barrier model is to be considered as

a first approximation in the case of snowballs, this point is elaborated upon is Section 6.1.3. A similar potential energy barrier calculation with the interfacial density transition profile given by Lurio et al. [70, 71] and inclusion of the surface energy may give a more accurate picture.

As the quantum tunneling effect can be ruled out in the case of snowballs, it's more realistic to consider a Maxwell-Boltzmann energy distribution of snowballs trapped in a potential well created by the image charge potential in combination with an externally applied electric field normal to the interface. A fraction of ions have energies higher than the potential energy barrier. These ions will cross the interface into the vapor phase. Kramer [64] and Chandrasekhar [22] have shown that the escape rate P_{th} of particles from a potential well in consequence of Brownian motion is

$$P_{th} \propto exp(-E_b/k_B T). \tag{3.13}$$

where E_b is the height of the potential energy barrier and T is the temperature of the system. Measuring the extraction efficiency of positive ions as function of temperature gives the height of the potential energy barrier (see Section 6.1.2).

3.7 Conclusion

This chapter gives an overview of positive helium ion and electron properties in superfluid helium. In general, postive ions form "snowballs", i.e. the density around the ion is increased and electrons form "bubbles", i.e. a cavity is formed around the object. The mobility and drift velocity of positive ions in superfluid helium is important to understand the experimental results on the snowball efficiencies presented in Chapter 6. The interaction of snowballs with the superfluid-vapor interface is not yet well understood. The barrier height and location of the potential minimum at the superfluid-vapor interface depend strongly on the details of the density profile at the interface. An accurate theoretical description of the extraction of positive ions and the height of the potential energy barrier is not available yet. Thermal excitation across a potential energy barrier is the most probable explanation.

4 Experimental techniques

The experimental setup for a cryogenic ion catcher consists mainly of an experimental cell and a cryostat which cools down this cell to the desired temperature. Buffer gas can be let in to the experimental cell independently and it can be filled with the desired buffer gas in order to thermalize and transport ions. In our measurements we used helium (in its cryogenic gas phase and its superfluid phase), argon and neon (in their cryogenic gas phase).

4.1 Cryostat

The cryostat used in this project is of "bath cryostat" type which is designed to contain a sufficient supply of cryogens for a convenient duration of operation without refilling (see Figure 4.1). The refilling interval is determined mainly by factors such as the inherent heat load of the cryostat, the heat load from the electric cabling and the cooling power needed for the experimental cell. The main components of the cryostat are the outer vacuum chamber, the liquid nitrogen reservoir, the liquid helium reservoir, the 77 K heat shield, the 4 K heat shield and the 1 K pot. Most parts of the cryostat except the 1 K pot and the heat shields are made of stainless steel because of its very low heat conductance. The heat shields and 1 K pot are made of copper for a good heat conductance with the cryogen reservoirs and are gold-plated for reflection of heat radiation. The cryostat was custom designed and constructed by Vacuum Specials B.V. (Woerden, Netherlands).

4.1.1 Outer vacuum chamber

The outer vacuum chamber (see Figure 4.1) is at room temperature and its main purpose is to provide vacuum for thermal insulation of the whole system. A vacuum

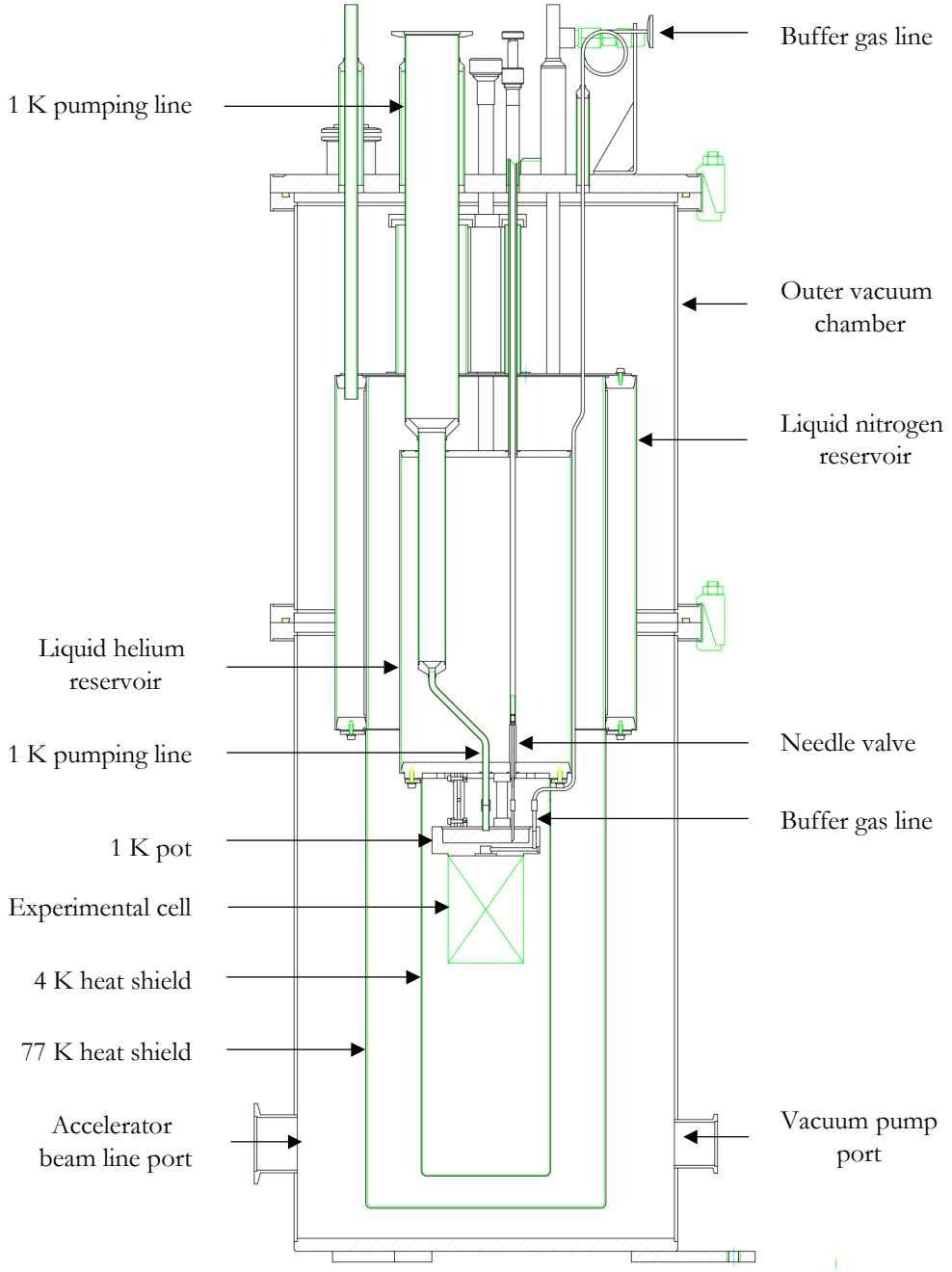

Figure 4.1: *Cryostat.*

of $\sim 10^{-7}$ mbar is reached after filling with cryogens. The outer vacuum chamber consists of two parts: (1) the top plate which contains the inlet and outlet ports for the cryogens, the electric cabling ports and the buffer gas port for the experimental cell and (2) the two-piece vacuum chamber, which consists of a cylindrical upper part and a cup-shaped lower part. It is possible to remove the lower part of the chamber or the whole chamber. There are four ports welded on the lower part of the chamber in which three act as vacuum accessory ports (pressure gauges, pumps, venting valves) and the fourth as accelerator beam inlet. All three parts are assembled with rubber O-ring seals and clamps.

4.1.2 Liquid nitrogen reservoir

The liquid nitrogen reservoir is an annular stainless steel vessel which can store 7.5 liters (Figure 4.1). This reservoir together with a gold-plated copper heat shield attached to it acts as a heat shield for the inner 4.2 K region. There are three stainless steel tubes connecting the liquid nitrogen reservoir and the top plate of the outer vacuum chamber. These are used as the inlet and outlet ports for the liquid nitrogen. The liquid nitrogen reservoir is wrapped with 25 layers of aluminum-coated polyester foil (NCR2) which acts as super-insulator.

4.1.3 Liquid helium reservoir

The liquid helium reservoir is a cylindrical stainless steel chamber which can hold up to 6 liters (Figure 4.1). It is connected to the top plate of the outer vacuum chamber with four stainless steel tubes which act as a support for this reservoir. These tubes are the (1) liquid helium inlet, (2) the exhaust, (3) the needle valve which controls the liquid helium flow from the liquid helium reservoir to the 1 K pot and (4) the pumping line to the 1 K pot which passes through the liquid helium reservoir. These four tubes are heat sunk to the liquid nitrogen reservoir. The liquid helium reservoir is wrapped with 5 layers of aluminum-coated polyester foil (NCR2) as super-insulator. A gold-plated copper heat shield is attached to the liquid helium reservoir to reflect the heat radiation from the 77 K heat shield towards the experimental cell (Figure 4.1).

4.1.4 1 K pot

The 1 K pot is a gold-plated copper chamber attached to the liquid helium reservoir with three carbon fiber bars (Figure 4.1). It is the part of the cryostat system where the lowest temperature is attained. Liquid helium can be let in to the 1 K pot from the liquid helium reservoir via a needle valve and can be pumped away through a pumping line which passes through the liquid helium reservoir (Figure 4.1). The 1 K pot is cooled by lowering the vapor pressure inside it. A roots pump with 500 $m^3\,h^{-1}$ pumping capacity is employed to pump on the 1 K pot. The pumping

is controlled by a manual valve on top of the pump. The lowest temperature attained by this cryostat is 0.92 K; the lowest long term stable temperature achieved is $\sim$1.00 K. The experimental cell is attached to the 1 K pot with an indium seal and screws (see Figure 4.2a). A steel capillary which acts as buffer gas inlet to the experimental cell passes alongside the liquid helium reservoir and through the 1 K pot to pre-cool the buffer gas before it enters the experimental cell (Figure 4.1).

4.1.5 Electric cabling

Twelve cryogenic coaxial cables (Type SR - Lake Shore Cryotronics) and 16 0.1 mm diameter twisted pair insulated copper wires connect the experimental cell to the outside world. These cables start from vacuum feed-throughs on the top plate and are heat sunk on different temperature stages before they reach the low temperature region. The coaxial cables go all the way to the experimental cell. The twisted pair insulated copper wires end on sockets attached to the bottom of the liquid helium reservoir. Connections from these 4.2 K sockets to the 1 K pot sockets are made with thin twisted pair insulated manganin wires. The temperature sensors and the heater are connected with the temperature controller using these 1 K pot sockets.

4.1.6 Helium consumption

The liquid helium consumption of the cryostat is due to the evaporation in the liquid helium reservoir because of the heat load from the 80 K reservoir by radiation and conduction via ports and because of evaporation in the 1 K pot needed to maintain the temperature of the experimental cell. The heat load due to radiation loss Q_{rad} is given by

$$Q_{rad} = A_s \times q_{rad} \times E \times \left(\frac{1}{1+n}\right) , \tag{4.1}$$

where A_s is the size of the radiating surface (m^2), q_{rad} is the black-body radiation heat load per unit area (2 $W\,m^{-2}$ between 80 K and 4.2 K and 20 $\mu W\,m^{-2}$ between 4.2 K and 1 K), E is the emissivity of the surface 0.1 (for a polished metal surface) and n is the number of layers of super-insulation. The heat load due to conduction loss Q_{con} is

$$Q_{con} = \frac{A_c \times q_{con}}{L} , \tag{4.2}$$

where A_c is the cross-sectional area of the conducting material, q_{con} the conduction per unit length (0.317 $W\,mm^{-1}$ between 80 K and 4.2 K and 0.6×10^{-3} $W\,mm^{-1}$ between 4 K and 1 K, for stainless steel), and L the length of the conducting material.

The total heat load on the liquid helium reservoir due to radiation is 0.033 W and due to conduction is 0.15 W. The radiation heat load on the 1 K pot and experimental cell are very small (2 μW) because they are facing the 4.2 K shield. The conduction heat load is contributed by the helium input line to the experimental

cell, the pumping line to the 1 K pot and the cryogenic coaxial cables between experimental cell and the 4.2 K sockets. Together they give a heat loss of 0.034 W. Another heat source of concern is the ^{223}Ra source. For a ^{223}Ra source of 10 kBq the heat load from the absorption of decay products is 50 nW, which is negligible. The total heat load on the helium reservoir is thus 0.22 W. As 1 W evaporates 1.3 liters of helium per hour, the inherent helium consumption of the cryostat is 0.25 liters per hour. The helium consumption during the experiments agrees very well with this number. Evaporation from the 1 K pot thus gives only a small contribution to the helium consumption.

4.1.7 Temperature control

A temperature controller (Model 340, Lake Shore Cryotronics) is used to control the experimental temperature. The controller monitors the temperature with two thin-film resistance temperature sensors (Cernox RTD CX-1030, Lake Shore Cryotronics) and one Pt100 temperature sensor. The Pt100 sensor and one Cernox temperature sensor are mounted on the 1 K pot. The other Cernox sensor is attached to the bottom of the experimental cell. The operating range for the PT-100 sensor is from 873 to 30 K. The calibration for the Cerenox sensors in the range 0.3 K to 40 K was provided by the manufacturer. We have extended the Cernox sensor calibrations up to room temperature by comparing them with the Pt100 sensor. The Cernox sensors have an accuracy of $\pm$ 5 mK and a long term-stability of $\pm$ 25 mK at 1.4 K. Temperature control is achieved by tuning the cryostat needle valve and the pumping speed such that the temperature is below the desired temperature. Then the temperature controller is used to heat up the 1 K pot to the desired temperature by applying an electric current through a thin wire heater (manganin) wound around a copper block and installed on the 1 K pot. The Lake Shore temperature controller uses a PID (proportional-integral-derivative controller) control algorithm to compute the control output based on the temperature set-point and feedback from the temperature sensor. A temperature stable to within 1 mK over a period of many hours was achieved.

4.2 Experimental cell

The experimental cell is made of a copper cylinder. Its top part is attached to the 1 K pot. The bottom is closed with a copper plate with an indium seal (see Figure 4.2a). Electric connections to the experimental cell are made via stycast feed-throughs in the bottom plate. A steel capillary running from the cryostat top plate to the experimental cell via the 1 K pot acts as a pumping port and a buffer gas inlet for the experimental cell. A cernox temperature sensor is attached to the bottom plate in order to achieve an accurate temperature control of the experimental cell.

Stycast rods and spacers are used to build up the electrode configuration inside

the experimental cell. A radioactive ion source, ion trajectory manipulation electrodes, an aluminum ion catcher foil and an α-particle detector are assembled in cylindrical symmetry (see Figures 4.2b and 4.2c).

Once cooled down to the required temperature, helium gas can be let into the experimental cell to have cryogenic gas or superfluid helium as stopping medium for high-energy radioactive ions. Thermalised ions can be transported to the aluminum catcher foil using an electric field provided by the set of guiding electrodes (see Figure 4.2d).

4.2.1 Radioactive scource

Many characteristics of ion survival in a stopping medium can be studied using an "open" α-decaying radioactive source; i.e. a thin source without protective layer such that α-decay products can recoil out of the source.

Advantages of this type of studies are: (1) no external high-energy ion beam is required as the α-decay recoil ions simulate an ion beam; (2) absolute efficiencies can be easily determined as the primary source strength is readily measured.

In this work, ^{223}Ra sources, giving 120 keV ^{219}Rn recoil ions, were used. We detect the ^{219}Rn ions via their characteristic α decay. This radioactive decay detection is essentially background-free and sensitive to the decay of a single atom/ion, resulting in very precise measurements over a large dynamic range. ^{223}Ra sources are prepared from an open ^{227}Ac source as described in [59]. Details of the decay chain of ^{227}Ac are given in Figure 4.3 and Table 4.1. A schematic picture of the source preparation set-up is shown in Figure 4.4. The ^{227}Ac source is placed at the bottom of a chamber filled with $\sim$30 mbar helium gas. A copper screw is placed a few centimeters above at a negative potential (-150 to -300 V) relative to the ^{227}Ac source.

^{223}Ra ions, recoiling from the ^{227}Ac source following the α decay of ^{227}Th, are stopped in the helium gas and transported by the electric field onto the tip of the copper screw. In order to confine the deposition of ^{223}Ra, a plastic tape is wrapped around the side of the copper screw so that only the tip of the copper screw is visible from the ^{227}Ac source.

In the first phase of this project, ^{223}Ra sources where provided by the Department of Physics, University of Jyväskylä, Finland and the Nuclear Physics Institute, University of Mainz, Germany. In Spring 2007 we obtained a 500 kBq ^{227}Ac source from the International Research Center for Nuclear Material Science, Tohoku University, Japan and set up our own ^{223}Ra source preparation unit. Taking care of the cleanliness of the system, the maximum recoil collection efficiency of 30% is obtained; resulting in a saturated ^{223}Ra activity of 75 kBq and thus a ^{219}Rn recoil ion source strength of 37 500 s^{-1}.

In our experiments we mainly consider the α-line from the ^{219}Rn decay because this isotope is the primary recoil ion from the ^{223}Ra source. When using an α-decay recoil source, the number of recoils entering the stopping volume and the location

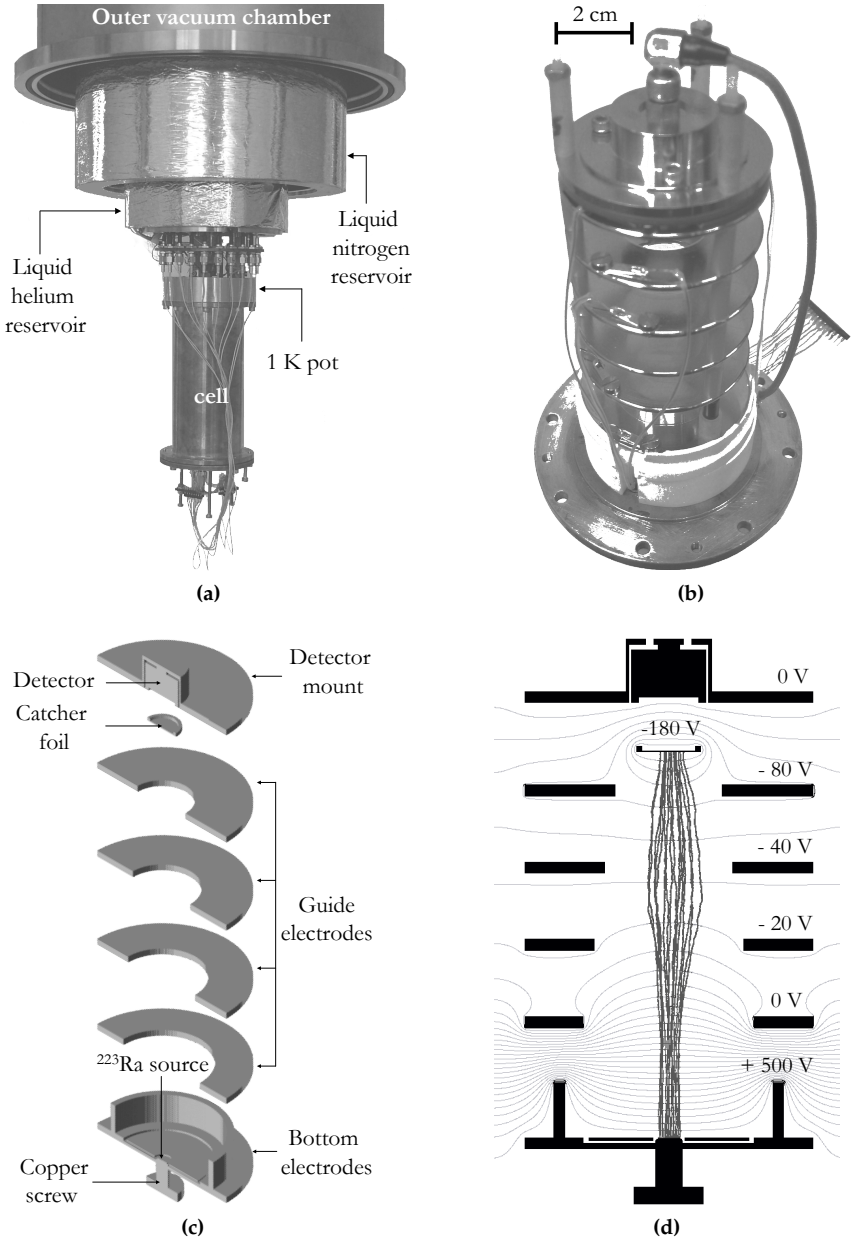

Figure 4.2: ***(a)*** *Inside view of the cryostat with cell mounted on the 1 K pot.* ***(b)*** *Photograph of the electrode assembly.* ***(c)*** *Cut-away view of the inside structure of the experimental cell.* ***(d)*** *Cross-sectional view of the electrode assembly. Decreasing voltages on the bottom electrode/source, guiding electrodes and catcher foil create the electric field that transports ions from close to the source onto the catcher foil. Dark gray lines indicate the ion trajectories and light gray lines indicate the equipotential lines from ion optics simulations with SIMION [30].*

from which they originate is known accurately for the first daughter in the decay chain only. The measured α particle spectra also contains spectral lines from ^{215}Po and ^{211}Bi, the other α emitters in the ^{223}Ra decay chain. However, ^{215}Po and ^{211}Bi are difficult to interpret. Being the granddaughter of the ^{223}Ra source, not all ^{215}Po nuclei originate from the source, but from all the places where ^{219}Rn has ended up. Because its half-life of 1.78 ms is comparable to the transport time, it can also decay along its path. The origin of ^{211}Bi recoil ions, being three α decays away from ^{223}Ra, is even more uncertain than that of ^{215}Po. Moreover, ^{211}Bi is reached via the β-decay of ^{211}Pb that has a half-life of 36 min; longer than our typical measurement time for a certain setting. This prevents us to deduce any relevant information from the ^{211}Bi line intensities.

4.2.2 Electronics and Data Acquisition

The raw data in our experiments are α particle energy spectra. Silicon detectors are used as α-energy spectrometers. They function perfectly down to ~ 1 K. The silicon detector is a thin slice of boron implanted n-type silicon, forming a rectifying p-n junction. A reverse bias voltage of 50 to 100 V to the p-n junction produces a depletion layer about 100 μm thick. The electron-hole pairs formed by ionisation when a charged particle traverses the layer are picked up by the electrodes and put in to a charge sensitive preamplifier. The output of the preamplifier is fed into a linear amplifier which amplifies and shapes the pulse, increasing the signal-to-noise ratio in order to optimize the energy resolution. The signal from the linear amplifier is fed into an ADC (analog to digital converter) and then to a MCA (multichannel analyzer) to convert the analog pulses to digital values and add the numerical values in corresponding channel of the spectrum.

4.2.3 Spectrum analysis

The experimental data in our measurements are the α-decay spectrum of the daughter nuclei of ^{223}Ra collected on the aluminum catcher foil and from the superfluid-vapor interface or the α-recoil source (depending on the experimental situation). Thus our typical spectra consist of 2 sets of lines, one from decay on the aluminum catcher foil and an other from the decay at the source or at the interface. Each set of lines consists of 6 lines, three ^{219}Rn lines, two ^{211}Bi lines and a ^{215}Po lines (see Table 4.1).

$$f(x) = \begin{cases} \text{A.exp}\left[\frac{dx}{2}\left(\frac{2(x-x_0)+dx}{\sigma^2}\right)\right] & \textit{if } x < (x_0 - dx) \\ \text{A.exp}\left[-\frac{1}{2}\left(\frac{x-x_0}{\sigma}\right)^2\right] & \textit{if } x > (x_0 - dx) \end{cases} \tag{4.3}$$

In this representation an individual line is defined by four parameters: the position of the line maximum x_0, the peak height A, the width of the Gaussian σ and the dis-

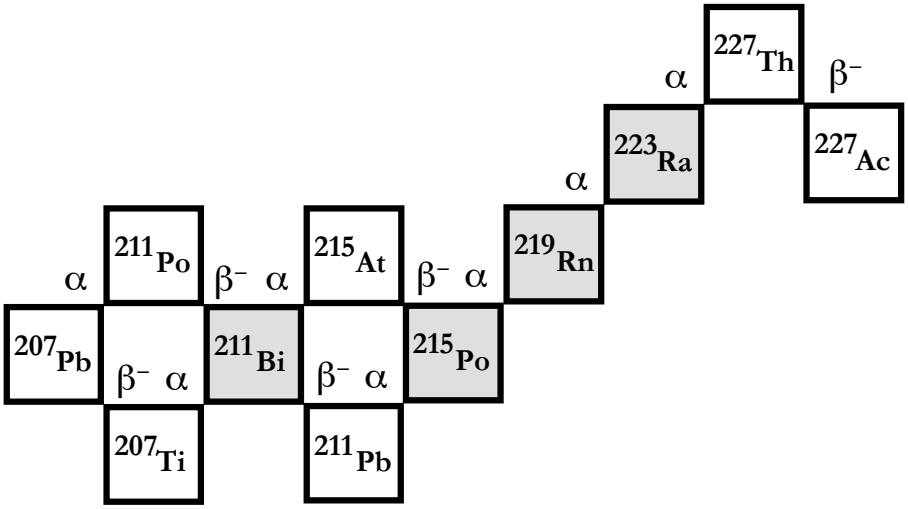

Figure 4.3: *Decay chain of ^{227}Ac.*

Table 4.1: *Isotopes in the ^{223}Ra decay chain and their properties.*

Isotope	Decay mode	Notation used	Half life	Energy [keV]	Branching Ratio [%]
^{223}Ra	α		11.435(4) d	5539.8(9)	9.20(20)
	α			5606.7(3)	25.7(5
	α			5716.2(3)	52.6(13)
	α			5747.0(4)	9.20(20)
^{219}Rn	α	Rn III	3.96(1) s	6425.0(10)	7.5(6)
	α	Rn II		6552.6(10)	12.9(6)
	α	Rn I		6819.1(3)	79.4(10)
^{215}Po	α	Po	1.781(4) ms	7386.1(8)	99.99977(2)
^{211}Pb	β^-		36.1(1) min	1373 (end-point)	100
^{211}Bi	α	Bi II	2.14(2) min	6278.2(7)	16.19(14)
	α	Bi I		6622.9(6)	83.54(14)

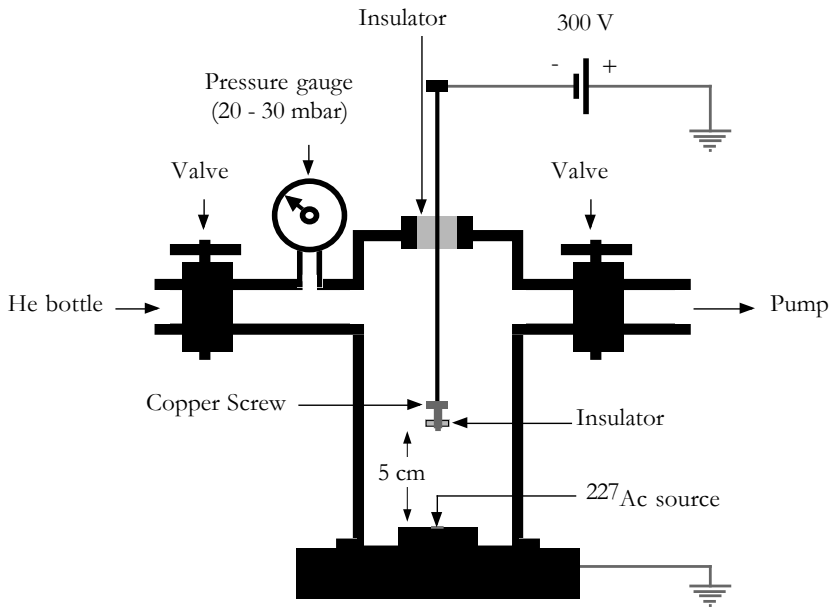

Figure 4.4: *Schematic diagram of ^{223}Rn source preparation setup.*

tance from the position of the line maximum x_0 to the junction point dx (Figure 4.7) [91]. The two sets are either mingled or separated depending on the difference in energy loss between α-emission from the source or the superfluid helium-vapor interface and the foil. The energy loss depends on the helium gas density and the distance travelled.

Table 4.2 shows an example of the typical energy loss experienced by alpha particles in our experiment. Figure 4.5 shows the channel number of identifiable peaks as function of their emitted energies. A linear relation is observed between the channel numbers and the α energies of an individual set. Two linear fits are obtained for the two sets of lines. Thus four parameters, the slope and offset of each linear fit can describe the positions of all 12 α peaks. The offset of the fit corresponds to the energy loss in the buffer gas and the aluminum catcher foil. The slope of the fit corresponds to the energy per channel.

Analyzing an α-decay spectrum involves the deduction of the total number of α counts contributed by the decay of the individual species. When determining the areas of the individual lines it is necessary to know the correct line shape. To test various functional forms, the intense well-isolated ^{215}Po line is used. When fitted with a Gaussian profile we observe a significant deviation at its low energy side (Figure 4.6). The line shape is accurately described by a combination of a Gaussian with a single exponential tail at the low-energy side which joins the gaussian such

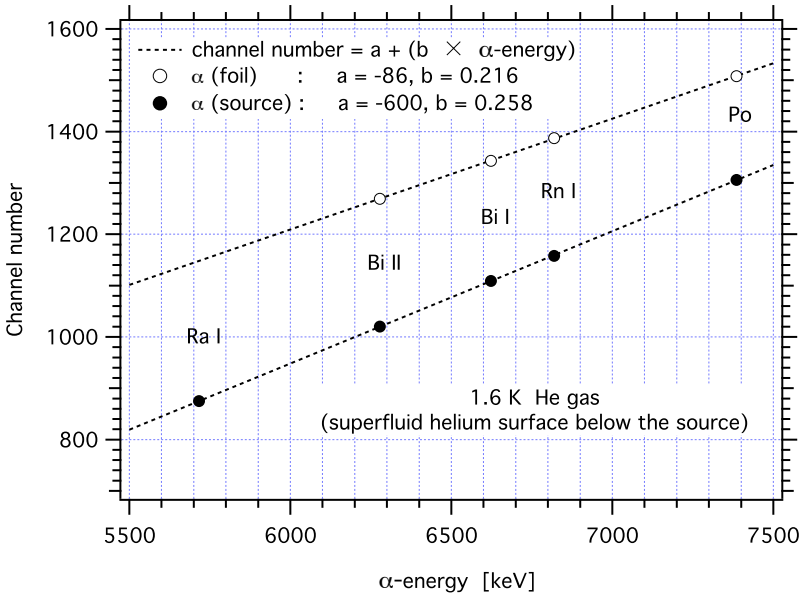

Figure 4.5: *A typical energy calibration plot. The channel numbers of identifiable peaks from each set are plotted as function of the emitted α-energies. A linear relation between the channel numbers and emitted α-energies is observed for an individual set.*

Table 4.2: *Example of the typical energy loss experienced by alpha particles in our experiments at temperatures 1.2 K and 1.6 K. α-particles emitted from the superfluid surface have to travel through 61 mm helium vapor, 0.81 μm aluminum foil and another 3 mm helium vapor. α-particles emitted from the foil have to travel through 0.81 μm aluminum foil and 3 mm helium vapor. E_α is the emitted α energy, E^s_α is the detected energy of α particles emitted from the superfluid surface, E^f_α is the detected energy of the α particles emitted from the catcher foil and ΔE is the energy difference between α-particles emitted from catcher foil and superfluid surface. ΔE at 1.6 K is larger than ΔE at 1.2 K due to the larger vapor pressure at 1.6 K.*

1.2 K				
α line	E_α [keV]	E^s_α [keV]	E^f_α [keV]	ΔE [keV]
^{219}Rn	6819	6540	6702	162
^{219}Rn	6553	6258	6432	174
^{219}Rn	6425	6123	6303	180
^{215}Po	7386	7120	7276	156
^{211}Bi	6623	6333	6503	170
^{211}Bi	6279	5972	6155	183

1.6 K				
α line	E_α [keV]	E^s_α [keV]	E^f_α [keV]	ΔE [keV]
^{219}Rn	6819	5416	6654	1238
^{219}Rn	6553	5092	6383	1291
^{219}Rn	6425	4933	6253	1320
^{215}Po	7386	6091	7232	1141
^{211}Bi	6623	5178	6454	1276
^{211}Bi	6279	4751	6104	1353

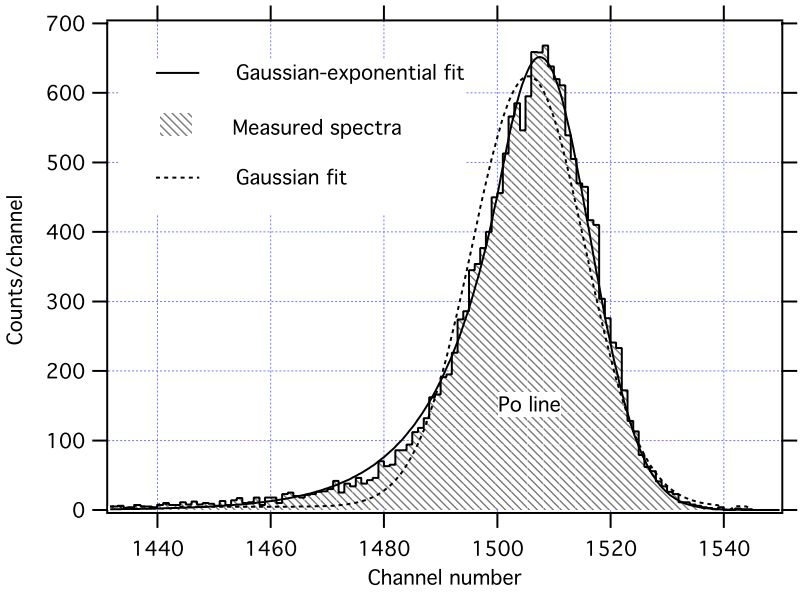

Figure 4.6: *A ^{215}Po α-decay line fitted with a Gaussian line shape and a Gaussian with low-energy exponential tail (see Equation 4.3).*

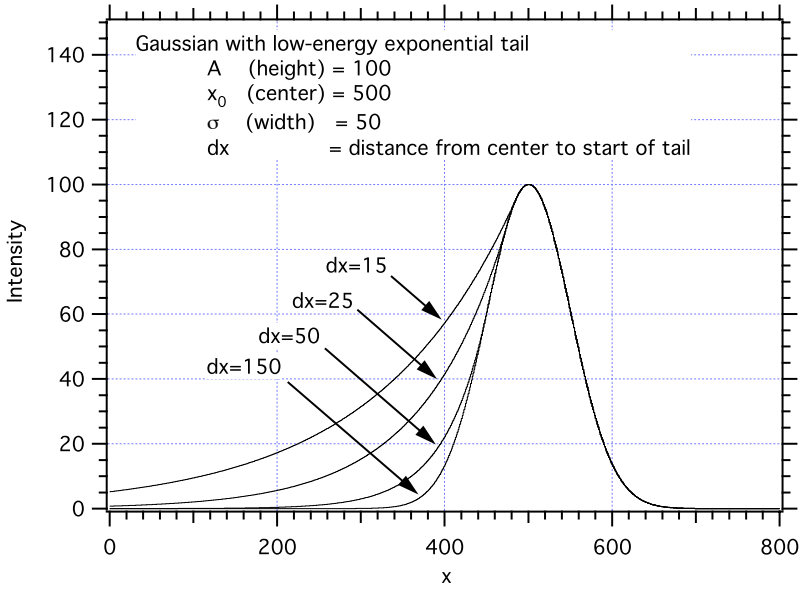

Figure 4.7: *Gaussian with low-energy exponential tail for different distances dx from its center to the start of its exponential tail. The low-energy tail arises from the energy loss due to multiple scattering.*

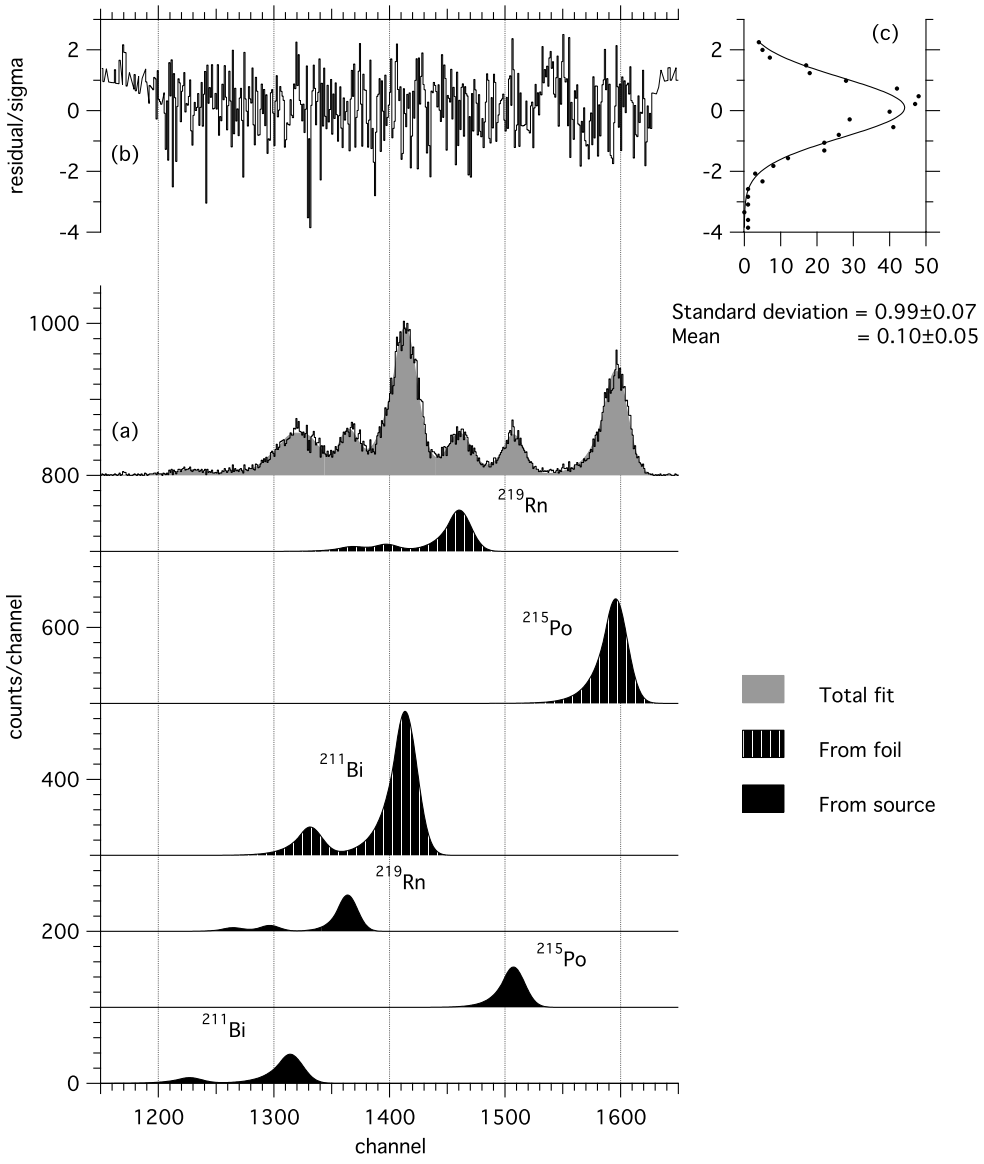

Figure 4.8: *A typical α-particle energy spectrum and its analysis. The solid line in (a) shows the measured spectrum and the fitted spectrum is overlayed in gray. The individual components resulting from the fit for the three α-decaying isotopes originating from both the foil (vertical lines) and the source (black) are shown in the lower parts. Panel (b) shows the residual/sigma of the fit. Here sigma is* $\sqrt{counts}$*. (c) shows the histogram representation of the residual/sigma of the fit; it follows a normal distribution with a standard deviation* ~ 1 *and mean* ~ 0*. This shows that our fitting function is a perfect representation of the spectra.*

that the function and its first derivative are continuous [91]: The total intensity of such a Gaussian-exponential pulse is

$$I = A \left[\underbrace{\int_{\infty}^{(x_0-dx)} e^{\left[-\frac{dx}{2}\cdot\left(\frac{2(t-x_0)+dx}{\sigma^2}\right)\right]} dt}_{\text{Exponential part}} + \underbrace{\int_{(x_0-dx)}^{\infty} e^{\left[-\frac{1}{2}\cdot\left(\frac{t-x_0}{\sigma}\right)^2\right]} dt}_{\text{Gaussian part}} \right] . \qquad (4.4)$$

Figure 4.6 shows the fit of such a function to a single ^{219}Po α-line. We need 48 parameters to describe the total spectrum containing 12 lines (12 for peak positions, 24 for individual line shapes and 12 for individual intensities). As mentioned before only 4 energy calibration parameters (2 for the interface or source and 2 for the aluminum foil) can describe all the peak positions. This reduces the number of free parameters from 48 to 40. Further, by taking the branching ratios of the ^{219}Rn and ^{211}Bi decays (see Table 4.1) into account, the intensities of 6 lines from the same location can be represented by 3 parameters. So for two α-decay locations 6 parameters describe the intensities of the 12 α-lines. This reduces the number of free parameters further from 40 to 34. It is reasonable to assume that the α-lines belonging to the different decay branches of the same isotope decaying at the same position have the same line shape, σ and dx. Thus with 12 shape parameters (6 for the α-particles from source or interface and 6 for the α-particles from the catcher foil) we can represent the line shapes of all 12 lines and the number of free parameters is finally reduced to 22.

We use a χ^2 minimization technique in our fitting procedure. The IGOR Pro 6 data analyzing program [127] is used to carry out the fitting procedure. The initial values for different parameters are deduced from strong, well-defined lines in the spectrum. Some of the parameters are fixed and others let free to iterate until the χ^2 minimized values are attained. The number of fixed parameters is then reduced in a step by step manner. For low-statistics spectra we have to take the same shape parameters for every line in each set. Here we assume that the α-particles emitted from the same region but from different isotopes result in the same line shape. This is often necessary only for ^{215}Po and ^{219}Rn. A typical example of the result of the fitting procedure is shown in Figure 4.8.

4.3 Gas density in the experimental cell at low temperature

For the gas catcher measurements the temperature and density are the relevant gas parameters. In practice the temperature and pressure are measured and the density is calculated using the ideal gas law. In the setup used in this work the temperature of the experimental cell is measured directly with sensors attached to

the cell and 1 K pot. The pressure in the cell is however not measured directly. A pressure gauge is mounted at the end of the filling capillary on top of the cryostat. The pressure gauge is thus at room temperature and measures the pressure of the room-temperature end of the filling capillary. In such a situation, i.e. where two volumes at different temperatures are connected, one cannot simply combine the temperature measurement of the volume at one temperature with the pressure measurement of the volume at the other temperature to obtain the density in either volume. This situation is investigated as follows. The cell was filled with gas at room temperature and then closed. The ratio of the pressure of the warm volume at room temperature P_w to the temperature of the cold volume in the experimental cell T_c was followed during cooling down. Many such data sets for different gases, starting pressures and sizes of the warm volume are shown in Figure 4.9, where the P_w/T_c ratio is normalised to the ratio P_0/T_0 before cooling down starts. In the absence of the effect discussed here the ideal gas law predicts that

$$\frac{P_w/T_c}{P_0/T_0} = 1 \tag{4.5}$$

at all temperatures although pressure and temperature are measured at different places. We see a clear deviation from this. The effect does not depend on the type of gas nor the pressure at room temperature within the rather limited range studied here.

The deviation is larger if the warm volume V_w is bigger relative to the cold volume V_c. The density in the cold volume can be determined from the measured T_c and P_w. A cold and a warm volume V_c and V_w are connected with a capillary of negligible volume. In the setup the capillary to cell volume ratio is a few 10^{-3}. With everything at room temperature T_0, the ideal gas law holds for the whole system

$$P_0(V_c + V_w) = nRT_0 \ , \tag{4.6}$$

where P_0 is the pressure at room temperature, n is the amount of gas (in mole) in the system and $\mathrm{R} = 8.31$ J mole^{-1} K^{-1} is the universal gas constant. During the experiments the volume V_c is cooled down to a temperature T_c, the volume V_w stays at room temperature T_0. The pressures in both volumes are P_c and P_w respectively. This gives the ideal gas law equations in the separate volumes

$$P_c V_c = n_c R T_c \ , \tag{4.7}$$

$$P_w V_w = n_w R T_0 \ , \tag{4.8}$$

with the total amount of gas unchanged

$$n \ = \ n_c + n_w \ , \tag{4.9}$$

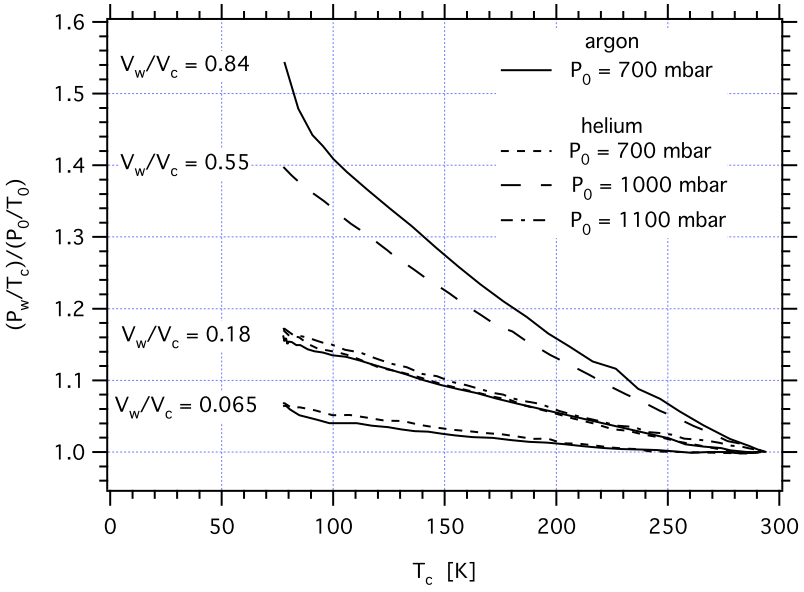

Figure 4.9: *Ratio of the warm volume pressure (P_w) to the cold volume temperature (T_c) as a function of T_c during cooling down, normalised to the ratio before cooling down starts (P_0/T_0). Data sets for helium and argon at different starting pressures P_0 and warm to cold volume ratios V_w/V_c are shown.*

where n_c and n_w are the amount of gas (in mole) in the cold and warm volumes. Substituting Equation 4.7 and Equation 4.8 in Equation 4.6 gives

$$P_c = \frac{T_c P_0}{T_0}\left(1 + \left(1 - \frac{P_w}{P_0}\right)\frac{V_w}{V_c}\right) . \tag{4.10}$$

For $V_w \to 0$, Equation 4.10 reverts to what is expected from the ideal gas law: P_c/T_c is constant during cooling down. For non-negligeable value of V_w/V_c, both P_w and P_c are not what is expected from the ideal gas law. P_c can be calculated from P_w, T_c and V_w/V_c and the density in the cold volume can be determined using the ideal gas law applied to this volume

$$\frac{n_c}{V_c} = \frac{P_c}{RT_c} . \tag{4.11}$$

The density of the warm volume can be calculated in an analogous manner. Figure 4.10 shows the densities of the cold and warm volumes relative to the density at room temperature for the same measurements represented in Figure 4.9. The density in the warm volume decreases and the density of the cold volume increases. This relationship is plotted as a function of V_w/V_c for a cold volume temperature

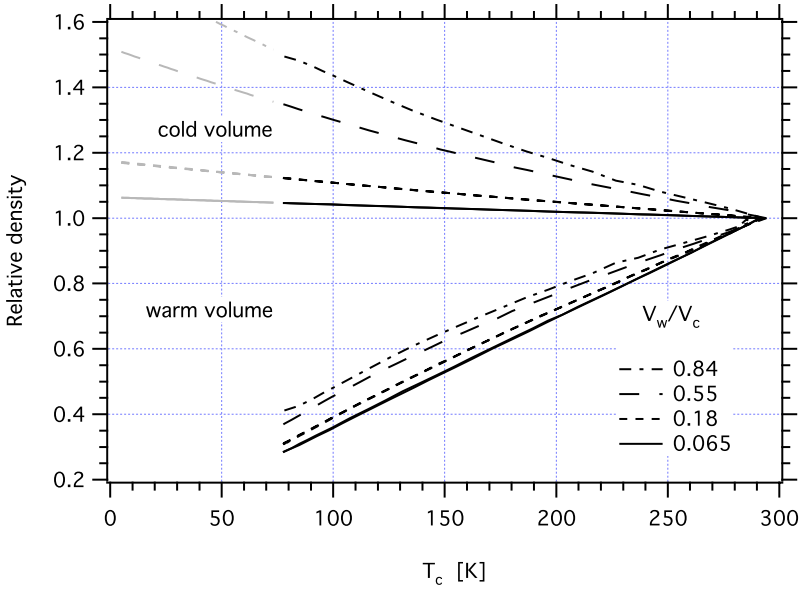

Figure 4.10: *Density relative to the room temperature value in the warm and cold volumes as a function of the cold volume temperature T_c for different warm to cold volume ratios V_w/V_c. The cold volume relative density is extrapolated to 5 K.*

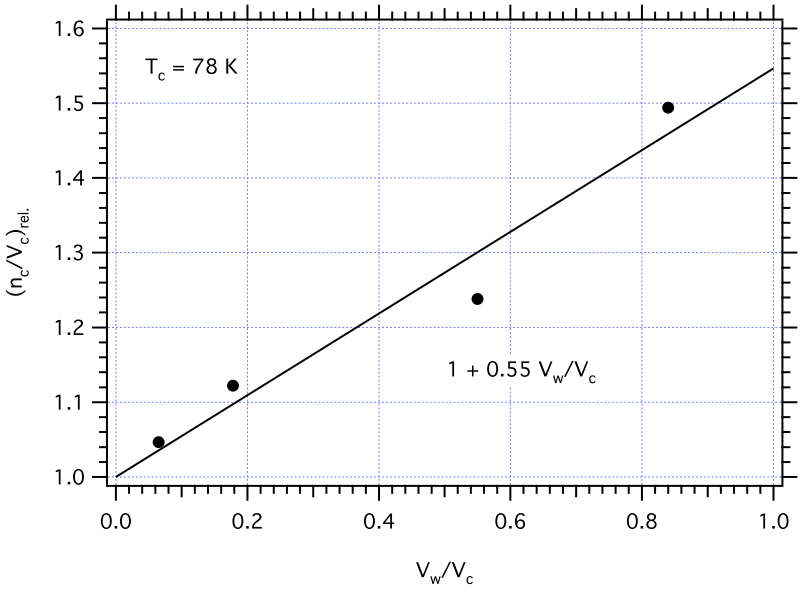

Figure 4.11: *Cold volume density n_c/V_c relative to its room temperature value at a cold volume temperature T_c of 78 K as a function of warm to cold volume ratio V_w/V_c. The result of a linear fit with a fixed offset of $(n_c/V_c)_{rel} = 1$ is indicated.*

of 78 K in Figure 4.11. Equation 4.11 and 4.10 are used to calculate the density in the cell from the measured values T_c, P_w and the known volume ratio V_w/V_c.

In summary: when cooling down, the pressure in the warm volume decreases less than the temperature (see Figure 4.9). At the same time, the higher pressure in the warm volume causes the cold volume density to increase (see Figure 4.10). Because these two effects are of similar size, the error made in calculating the cold volume density using the warm volume pressure is small. For $V_w/V_c < 0.5$, this error is less than 5%. In all measurements except the mobility measurements, V_w/V_c was 0.18 or 0.065 and the effect described in this section is not corrected for. The correction is performed for the mobility measurements of ^{219}Rn ions in noble gases where $V_w/V_c = 0.55$ (see Section 5.3.1).

4.4 Conclusion

An experimental apparatus was designed and constructed in order to perform the experiments outlined later in this thesis. The apparatus has two major parts, the cryostat and an experimental cell. The cryostat is able to stabilize the temperature of the helium cell between 1 K and room temperature. The electrode configuration in the experimental cell is optimized based on the results from ion-optical simulations. An α-recoil ion source is an excellent choice to probe the transport and extraction efficiencies of ions in a stopping medium since radioactive decay detection is sensitive to a single atom or ion. This technique provides a near zero background level. The line shape of the α-decay is accurately described by a combination of a Gaussian with a single exponential tail at the low energy side. By considering the branching ratios of α-decays, assuming the same line shape per isotope and location and using energy calibrations of the observed lines, the number of free parameters required to represent the line shapes of all 12 lines is reduced from 48 to 22.

5 Cryogenic noble gas ion catchers

An energetic ion slowed down in a noble gas has a finite probability to be in a charged state at the time of thermalization. Under suitable conditions these ions survive long enough to be transported through and extracted from the stopping volume. This is the underlying principle of the use of noble gases to transform high-energy nuclear reaction products into low-energy ion beams. At high energies the interaction of the ions with noble gas atoms causes slowing down and may also lead to neutralization by electron transfer. The neutral atom then can be stripped of an electron again. Which process dominates depends on the cross section for the respective processes. Near and at thermal energies, i.e. if the ionization energy of the ion $E_i(ion)$ is below the ionization energy of the noble gas $E_i(noble)$ by more than its kinetic energy $E_{kin}(ion)$,

$$E_i(ion) < E_i(noble) - E_{kin}(ion) \ , \tag{5.1}$$

the ions cannot neutralize in collisions with noble gas atoms. Due to the high ionization potential of noble gas elements the probability an ion thermalizes in a charged state is large. Ions neutralize upon hitting the wall or any structure inside the gas catcher. Because the electrode structures inside gas catchers are designed to prevent ions from hitting the walls, neutralization upon colliding with a solid structure is not considered in the following discussion. What happens to thermalized ions is influenced by the presence of impurities and ionized noble gas atoms which are created by the energetic ions and possibly by an accelerator beam or radioactive decay radiation [6]. Impurities are involved in the neutralization of ions through 3-body recombination involving a free electron to form molecules or adducts with the ions (see e.g. [65]). It is important to note that the ionizing radiation also plays a role in re-ionizing neutral atoms. Generally speaking, the nuclide of interest will appear as four species: atoms and molecules and both of these in neutral or charged states.

A lot of technical developments over the past 25 years were devoted to remove impurities from and to prevent ionization of the noble gas. Sub-ppb impurity levels have been achieved in devices that are built to ultra-high vacuum standards which are bakeable and filled with ultra-pure noble gas (see e.g. [65]). The construction of large ultra-pure gas catchers, although possible [93], is far from trivial. There is however another approach to reach ultra-pure conditions: freezing out of the impurities. We describe here measurements where this approach is investigated for the first time. This chapter will discuss on-line and off-line-experiments to study this approach. Mobility measurements of radon ions in cryogenic noble gases are also discussed.

5.1 Off-line measurements

The basic idea of an off-line experiment is to check the feasibility of a cryogenic noble gas ion catcher before going on-line which is technically more challenging and expensive. This experiment has been designed to investigate the slowing down and transport of energetic ^{219}Rn ions in helium, neon, and argon gas under cryogenic conditions. The underlying principle is to cool the gas cell to cryogenic temperatures (< 77 K) in order to 'freeze out' the impurities at the cold surfaces of the cell.

5.1.1 Experimental setup

The experimental setup is shown in Figures 5.1 and 5.2. A ^{223}Ra source with a typical source strength of a few thousand Bq is mounted at the bottom of the cell filled with a noble gas as stopping medium. The ~ 100 keV α-decay recoil ions will leave the extremely thin ^{223}Ra source if they are emitted in the "upward" direction. They are then thermalized in the noble gas near the source, i.e. at about 0.5 mm in 1 bar helium at room temperature (293 K) according to calculations using the TRIM [131] program package which numerically simulates the passage of charged particles through matter. Electrodes provide an electric field to guide the thermalized ions towards a thin (1.7 mg cm^{-2}) aluminum foil in front of a silicon detector which records α particle energy spectra. Ion optics simulations using the SIMION [30] program package, which calculates the electrostatic fields by numerical solution of the Poisson equation and allows to simulate the ion trajectory show that no losses occur due to the ion transport itself (see Figure 5.2). Ion transport is detected by the α-decay of ions collected on the aluminum foil. ^{219}Rn ions stick to the cell wall and electrodes when the temperature is below about 200 K. The silicon detector also observes with about 10 times lower efficiency α particles directly from the source. Those α particles transferring through the gas suffer a larger energy loss than those originating from the foil. Therefore both can be unambiguously identified. Different isotopes are identified based on their known α energies. The ^{223}Ra activity is

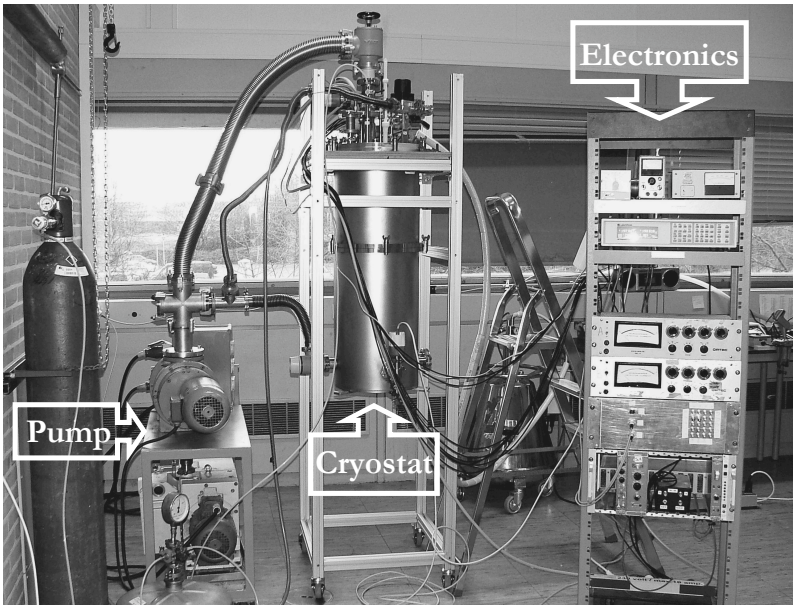

Figure 5.1: *Photograph of the off-line experimental setup.*

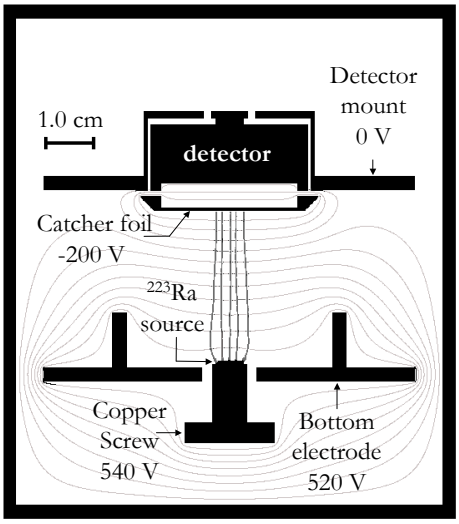

Figure 5.2: *Schematic view of the experimental cell. The voltages used with helium and argon gas filling are indicated. For neon the voltages were reduced to 65% of these values. The detector and container are grounded. Dark gray lines indicates the ion trajectories and light gray lines indicates the equipotential lines from ion optics simulations with SIMION [30]; they indicate 100% ion transport efficiency. In the simulations the presence of the gas is taken into account by a viscous force.*

960 Bq at the start and 550 Bq at the end of the experiments discussed here. The α particle detection efficiency is equal to the solid angle of the detector seen from the decay location (either source or foil). The efficiency that ^{219}Rn recoil ions survive the thermalization and are transported to the aluminum foil can be straightforwardly obtained by dividing the ^{219}Rn count rate originating from the aluminum foil by half of the ^{223}Ra source activity and by the detection efficiency. Decay losses during transport can be neglected because the ^{219}Rn half-life of 4.0 s is long relative to the transport time of order 1 ms for 1 bar helium at room temperature and the electric field used.

The experimental cell is attached to the so-called 1 K pot of the cryostat (see Section 4.1). As the experiments reported here aimed to show the effect of the freezing out of impurities, we did not use high purity gas in the experimental cell at room temperature. The experimental cell was not at all designed for good pumping capability. Moreover, in the case of helium the impurity level at room temperature was intentionally increased by adding air to the cell before filling it with helium. If uniformly frozen on all surfaces, 3 mbar of air would form a solid layer on top of the source thick enough to stop the recoils. To prevent this, we chose a 10 times lower partial air pressure of 0.3 mbar to be on the safe side. This corresponds to an impurity level of about 300 ppm or a density of 1.0×10^{16} atoms cm^{-3} consisting mostly of air. For neon and argon, no extra air was added, and we estimate the impurity content to be around 100 ppm.

At the start of a measurement series the cell is filled at room temperature with 1 bar noble gas and 0.3 mbar of air in the case of helium. The cell is then closed and cooled down to the lowest temperature, at constant gas density in the cell. For argon gas, measurements are restricted to above 75 K to avoid its condensation. The temperature is then increased in steps and the α particle energy spectrum is measured at each step. At each step thermal equilibrium between cell and the noble gas is confirmed by consecutive measurements showing the same α line intensities. Measurements above about 200 K are not useful as radon is not frozen out and the ^{219}Rn atoms are floating through the chamber (this is readily apparent from the α-energy spectra). Figure 5.2 indicates the voltages applied to the source, the guiding electrode, and the aluminum foil for helium and argon in the cell. For neon these voltages were lowered to 65 % to prevent electric discharging. This reduces the magnitude of the electric field without changing its profile. Thus for neon the ion tracks are the same as in Figure 5.2, only the ion velocity is reduced.

5.1.2 Results and discussion

The efficiency ϵ_{gas} of ^{219}Rn recoil ion transport to the aluminum foil is measured as a function of temperature for helium, neon and argon gas. The results are shown in Figure 5.3. Towards lower temperatures the efficiency is strongly enhanced, starting at about 120 K for all three noble gases. The efficiencies saturate below about 90 K. In a separate experiment related to a study of ions in superfluid helium, the

saturation efficiency for helium gas was observed not to change anymore down to 4 K. A least-squares fit of the data using a Hill's equation was performed. The Hills equation is a sigmoidal function of the form

$$\epsilon_{gas} = \epsilon_{min} + \left[\frac{\epsilon_{sat} - \epsilon_{min}}{1 + \left(\frac{T_{1/2}}{T_g} \right)^r} \right] , \tag{5.2}$$

where the coefficient ϵ_{min} is the efficiency at high temperatures, ϵ_{sat} is the saturation value of efficiency at low temperatures, r is the rise rate, T_g is the gas temperature and $T_{1/2}$ is the temperature at which ϵ_{gas} is at $(\epsilon_{min} - \epsilon_{sat})/2$. This function is used in order to quantify the observed trend. The saturation efficiency ϵ_{sat} is determined to be 28.7(1) % in helium, 22.1(2) % in neon, and 17.0(2) % in argon. Only the statistical errors from the measured spectra and the fitting procedure are given. The overall systematic relative error of about 6 % is due to the uncertainty in determining the detector solid angle. Qualitatively the ^{215}Po line intensities show the same temperature dependence as ^{219}Rn but α-lines from ^{215}Po are complicated to analyze, because the position where the isotopes are created is not known (see Section 4.2.1). We believe the high efficiencies and their saturation at low temperatures are due to the freezing out of impurities, which enhances the survival probability of thermalized ions. The saturation efficiency is reached once all impurities are frozen out. In our setup we cannot distinguish between atomic or molecular ions reaching the aluminum foil in front of the detector. At high temperatures, our measured efficiencies include both variants; although molecular ions should be rather rare since radon is a noble gas. At low temperatures, however, impurities that could take part in forming molecules are frozen out first. The measured efficiency is thus solely due to the ^{219}Rn ions.

In the absence of impurities the fate of the ions can still be affected by the ionization of the noble gas. We checked this qualitatively for helium: the electron-ion density was altered by changing the gas density and the electric field strength. A higher electric field separates electrons and ions quicker, resulting in a lower equilibrium ionization density, while a higher pressure increases the ionization density. We found that the efficiency at 73 K in the saturation regime does not change if the electric field is lowered by a factor of 4 or if the gas density is changed by a factor between 0.25 and 1.6.

We repeated the off-line measurements with a different electrode geometry in which intermediate guiding electrodes are incorporated between the source and the collection foil. The survival and transport efficiency of ^{219}Rn ions in helium gas over a wide range of gas density, temperature and electric field was measured. Measurements were done with helium gas pressures of 1 to 6 bar room temperature equivalent in a temperature range of 5 to 30 K (see Figure 5.4). The results show an almost constant efficiency of close to 30%. If neutralization would occur after slowing down, the efficiency would not be constant as a function of e.g. electric field or density.

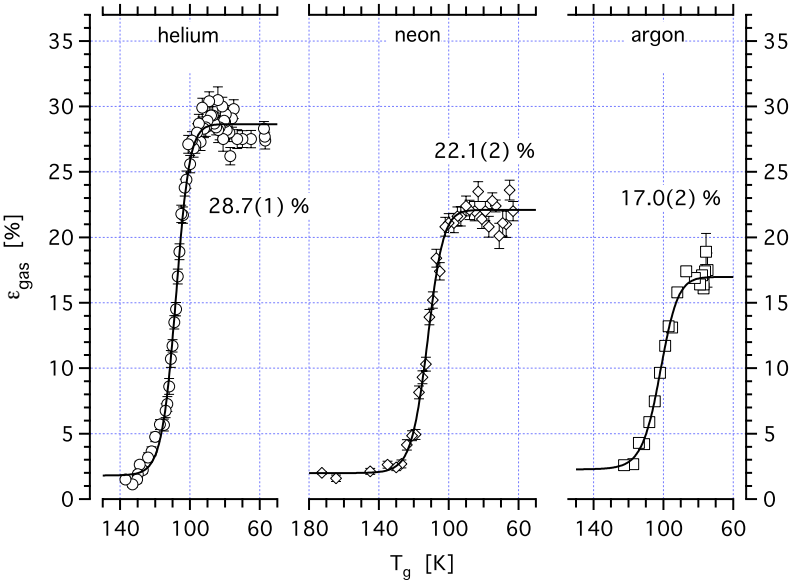

Figure 5.3: *Measured efficiency ϵ_{gas} as a function of temperature T that ~ 100 keV ^{219}Rn ions survive thermalization and transportation over about 3 cm in an ionic state through noble gases of densities equivalent to 1 bar pressure at room temperature. The lines are least-squares fits of a Hill's equation to the data. The saturation efficiency (with statistical error) deduced from the fit is indicated. The overall systematic uncertainty amounts to about 6 % as discussed in the text.*

From this we conclude that at thermal energies neutralization due to free electrons is negligible in our experiments. Therefore the observed saturation efficiencies at low temperatures may well reflect the charge exchange and stripping cross sections involved in the slowing-down process of the ions. This would represent a fundamental upper limit for the efficiency of noble gas ion catcher devices. Note that the efficiencies decrease systematically from helium over neon to argon. This demonstrates that our results are based on intrinsic properties of the noble gases-ion system. A similar trend has been observed earlier for the slowing down of protons and muons in noble gases [2, 102]. Our data have to be compared with those obtained for ultra-pure helium gas catchers at room temperature. During the development of such devices by G. Savard and collaborators [72, 93, 116], efficiencies of up to 45% for fission fragments from a ^{252}Cf source were reported. Taking into account the systematic uncertainties involved in the efficiencies determined by Savard et al. and the fact that some dependence on the specific element is to be expected, we consider those measurements compatible with our work. A saturation extraction efficiency of 30(2)% for ^{219}Rn ions in helium gas in the SHIPTRAP stopping cell (at GSI) has been reported recently by Eliseev et al. [38].

Huikari et al. [59] used a room-temperature gas catcher system with modest

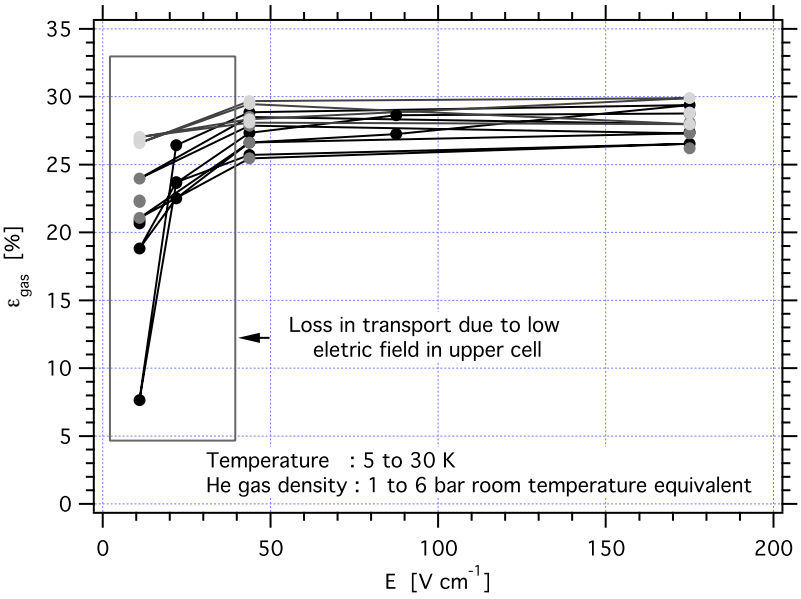

Figure 5.4: *Efficiency for ^{219}Rn ion survival and transport in helium gas over a wide range of density, temperature and electric field in the vicinity of the ^{223}Ra source. For small electric fields at the ^{223}Ra source, the field in the upper cell becomes so small (a few V cm^{-1}) that it was difficult to control accurately, causing some transport loss.*

purity helium gas (of order several ppm) to also extract ^{219}Rn recoils from a ^{223}Ra source. They reported a ^{219}Rn efficiency of 75% at a helium pressure of 50 mbar, decreasing strongly with increasing pressure: down to 20% at the lowest density used in the present work (equivalent to 250 mbar at room temperature) and down to an extrapolated value of 0.2% at a density equivalent to 1 bar at room temperature. This latter value is only slightly lower than our detection limit of about 0.3% efficiency. However, the pressure dependence of the efficiency reported in [59] differs completely from that observed by us and also by Maier et al. [72] for ultra-pure helium, where the efficiency does not change at all in the investigated pressure range. One could speculate whether the strong decrease of efficiency with increasing pressure observed in [59] is due to the presence of impurities, i.e. due to an increased neutralization via three-body reactions with electrons and impurity molecules. The fact that efficiencies higher than our low-temperature saturation values are obtained at pressures below about 200 mbar would indicate a higher ion survival probability during slowing down in the presence of impurities. This would happen, if charge exchange and stripping cross sections on impurity molecules are more favourable towards ion survival than those on helium atoms. The fact that in the system used by Huikari et al. [59] molecular ions are broken up in the extraction region of the gas catcher and contribute to the measured efficiency may be relevant

in this respect. Dedicated work is needed to understand this issue in detail. Since gas catchers have to operate at a rather high pressure to provide sufficient stopping power, there is no question that ultra-pure conditions need to be employed.

5.2 On-line measurements

The feasibility of cryogenic noble gases as stopping media was demonstrated earlier using α-decay recoil ions from a ^{223}Ra source. In their main prospected application, gas catchers are employed to stop an ion beam from an accelerator or energetic recoil ions from a target. On-line operation of a gas catcher differs from its off-line counterpart by the plasma created by the projectile beam. This will introduce an additional complication which we didn't encounter in off-line measurements. A detailed theoretical discussion of this phenomenon is outside of the scope of this work but some basic ideas are discussed in section 2.3. Here we investigated the effect of ionization of helium gas because this determines the maximum beam intensity the system can handle. A 13 MeV proton beam was used to ionize the helium gas just above the ^{223}Ra source. The combined efficiency of survival and transport of the recoil ions over several centimeters was measured as a function of the ionization density, i.e. beam intensity, the electric field strength, the helium pressure and the temperature.

5.2.1 Experimental setup

A ^{223}Ra source is placed near the bottom of a closed cylindrical cell. The cell is filled with the desired amount of helium gas and cooled down to the required temperature. The ^{223}Ra source is part of an electrode system guiding the thermalized ions over a distance of about 6 cm to a thin aluminum foil in front of a silicon detector.

In helium gas with a density equal to 1 bar pressure at room temperature, i.e. 0.18 mg cm^{-3}, α-decay recoil ions from a ^{223}Ra source are stopped within about 0.5 mm. At this location the ionization rate density due to both recoil ions and the α activity from the ^{223}Ra source with a typical activity of 5 kBq over a diameter of 4 mm is about 10^9 ion-electron pairs cm^{-3} s^{-1}. In the presence of a moderate electric field no influence of this ionization on the behaviour of the ions is expected. In order to study the effect of the gas ionization we have used a proton beam to ionize the region in which the recoil ions are stopped.

Apart from the presence of the proton beam the experimental setup is similar to that used in the off-line experiment (see Section 5.1.1). Therefore, only the new features are described in detail here. A photograph of the setup is shown in Figure 5.5 and a schematic view is shown in Figure 5.6. The most important difference is that the beam line is coupled to the cryostat and that the beam is let in to the cell. A copper window of 60 μm thickness through which the beam enters and a Faraday cup are incorporated. The electrode geometry is modified by adding three

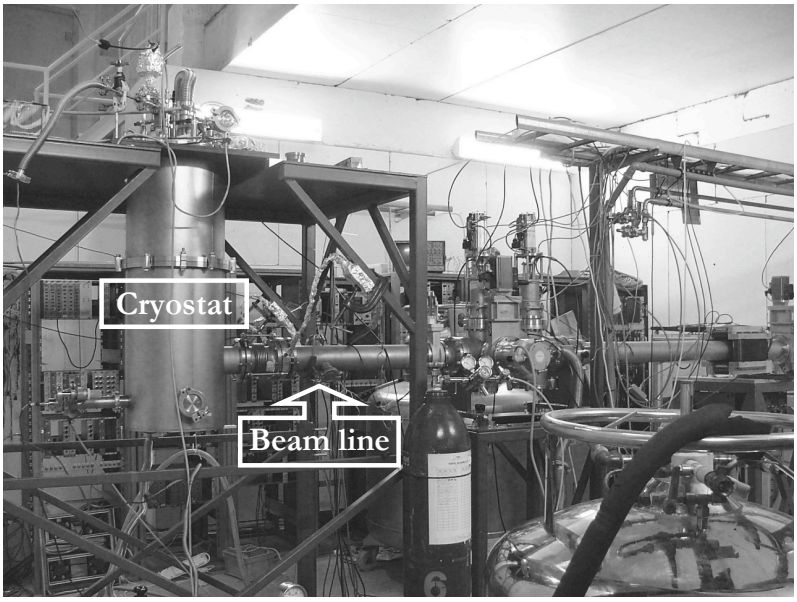

Figure 5.5: *Photograph of the on-line setup.*

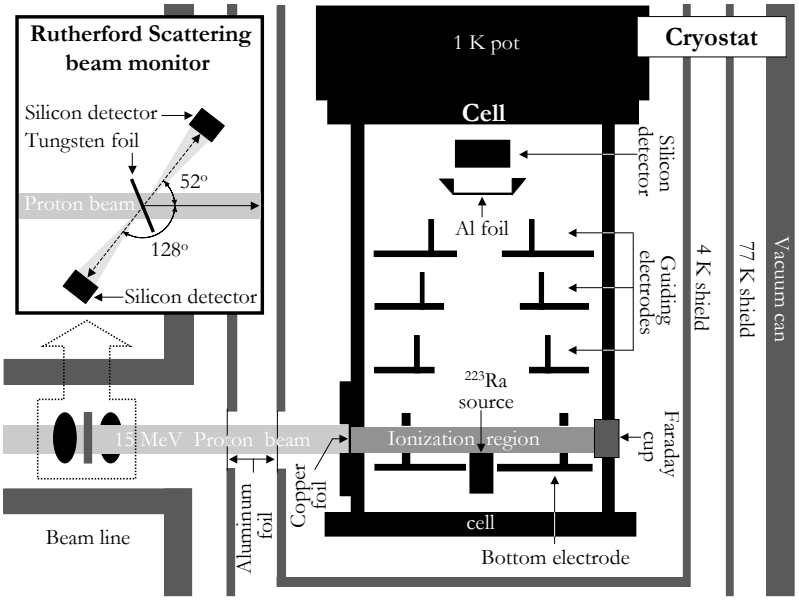

Figure 5.6: *Schematic view of helium gas ionization by a proton beam just above the ^{223}Ra source. Voltages on the electrodes produce an electric field which guides recoil ions stopped within about 0.5 mm from the source through the 5 mm diameter ionization region to the foil in front of the detector.* ***(Inset)*** *Top view of the Rutherford scattering beam monitor.*

guiding electrodes. To position the ion beam just above the top of the ^{223}Ra source, two diametrically opposite holes are drilled into the well-shaped bottom electrode. The proton beam enters the cell via the copper window, passes through the holes in the bottom electrode and is stopped in the Faraday cup. This Faraday cup was installed for the real time monitoring of the beam, but it gave a negative current when we admitted the beam to the gas-filled cell. Apparently a negative charge was collected on the Faraday cup. This charge collection is due to the large number of electrons knocked out by the protons when they pass through the helium gas. The Faraday cup was however very useful to align the beam when the cell was pumped to vacuum.

A 13 MeV proton beam from the cyclotron at the University of Jyväskylä was used to ionize the helium gas just above the ^{223}Ra source. A collimator restricted the beam diameter to 5 mm and care was taken to have a rather uniform beam intensity distribution over this diameter. A beam intensity of 1 pA corresponds to a helium ionization rate density within the volume of the beam of 5 $\times 10^9$ ion-electron pairs cm^{-3} s^{-1} for 1 bar room temperature equivalent of helium. The beam intensity was measured by Rutherford scattering on a 12.4 mg cm^{-2} tungsten foil at $\sim$60 degree backward angle with respect to the beam, thus having an effective thickness of 14.3 mg cm^{-2}. Scattered protons were detected with silicon detectors at forward and backward angles (52 and 128 degrees) with respect to the beam axis, resulting in a large dynamic range. Voltages were put on the electrodes such that the electric field in the region illuminated by the beam was much higher than that in the bulk of the cell. The cell is pumped to vacuum and then the beam is aligned with the help of two collimators and Faraday cup.

The α-particle energy spectra recorded with the detector give the intensity and identity of the transported α-decaying nuclides. Because only the information from α-decay of ^{219}Rn can be interpreted in a straightforward way (see Section 4.2.1), we restrict our analysis to the behaviour of ^{219}Rn ions.

5.2.2 Results and discussion

The combined recoil ion survival and transport efficiency from close to the source to the aluminum foil was measured for three temperature and density combinations: $T_g = 77$ K and $\rho = 0.18$ mg cm^{-3}, $T_g = 10$ K and $\rho = 0.18$ mg cm^{-3} and $T_g = 10$ K, $\rho = 0.54$ mg cm^{-3}. The electric field in the ionization region at the bottom of the cell was varied from about 20 to 160 V cm^{-1} by scaling all voltages with the same factor, thus avoiding any change in the ion paths through the cell. The ionization rate density was varied from 3 $\times$ 10^9 cm^{-3} s^{-1} to 9 $\times$ 10^{12} cm^{-3} s^{-1}; the lower limit is chosen such that the maximum efficiency of 30 % was still obtained at the lowest electric field, the upper limit is imposed by the radiation level limit in the experimental area. Up to now, room temperature gas catchers have been investigated at smaller electric fields (typically 5 - 25 V cm^{-1}) and mostly at lower densities (0.02 - 0.18 mg cm^{-3}) [38, 78, 93, 113, 116, 128]. Figures 5.7 and 5.8 show a representative

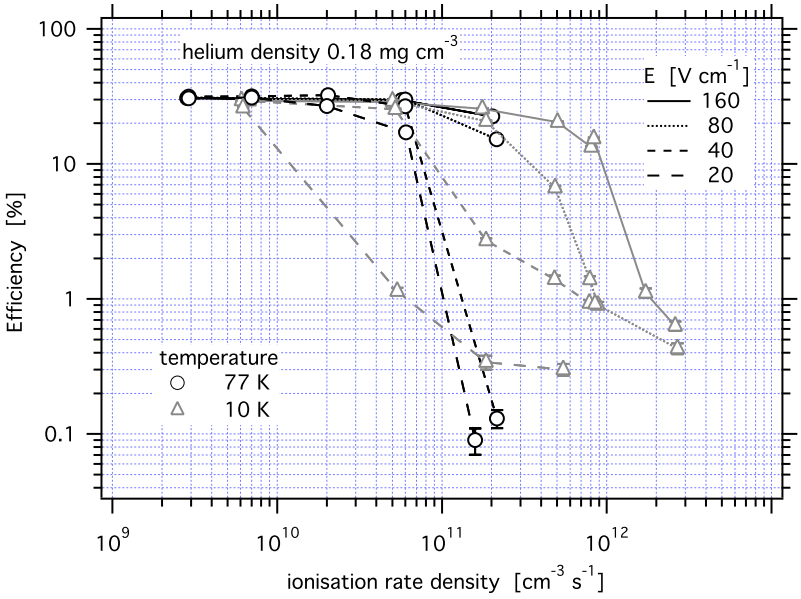

Figure 5.7: *The combined efficiency of ion survival and transport as a function of ionization rate density for different electric fields in the ionization region for temperatures 77 and 10 K and helium gas density 0.18 mg cm^{-3}.*

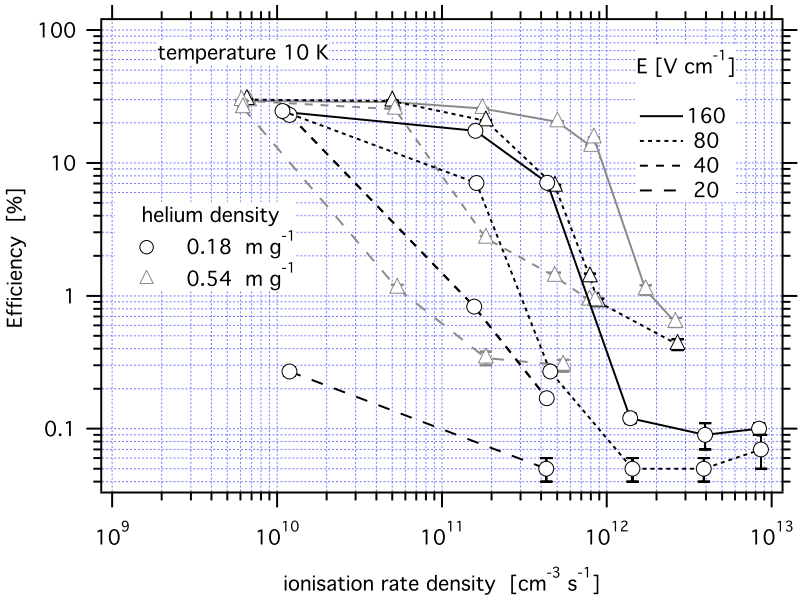

Figure 5.8: *The combined efficiency of ion survival and transport as a function of ionization rate density for different electric fields in the ionization region for temperature 10 K and helium gas densities 0.18 and 0.54 mg cm^{-3}.*

selection of results. At low ionization rate density, the efficiency saturates at a maximum of 28.7(17)%. This is exactly the same as in the experiments without ionizing beam, thus strengthening the conclusions from Section 5.1. Another important observation is the steep increase in the tolerable ionization rate density with electric field and its decrease with increasing helium density. Because the mobility of electrons is 2 - 3 orders of magnitude higher than that of positive ions, a positive ion cloud exists essentially in the ionization region (see sections 2.1 and 2.2). The applied electric field pushes the ions up and removes them from the ionization region. The equilibrium between ionization of the gas and removal of positive ions results in a steady state positive charge density. This positive ion cloud induces a shielding voltage V_{ind} for the applied field (see Equation 2.9). The induced shielding voltage increases as the beam intensity increases. The resulting decrease in the effective field slows down the removal of ions from the ionization region and enhances the increase in the positive charge density and induced voltage. Due to this positive feedback mechanism with increasing beam intensity one expects a quick increase in induced voltage up to the point where the effective field is zero. In this situation ions will diffuse out of the cloud into a region where the applied field transports them to the aluminum foil in front of the silicon detector. With the beam intensity increasing the positively charged cloud swells. For gas catchers this leads to a loss of ions as the ions hit the wall [113, 128] except if an RF barrier is present [125]. In our system there is room to accommodate such an expansion because only a small fraction of the ions may be pushed against the bottom electrode, neutralise and be lost for transport. It does not lead to a loss of ions. However, as the effective electric field is zero, electrons are no longer removed from the ionization region and a neutral low-density plasma results in which ions recombine with electrons. We believe this neutralisation is the main loss mechanism in our setup.

Figure 5.9 shows the combined ion survival and transport efficiency as a function of the ratio of induced to applied voltage (taken as the applied field multiplied with the beam diameter of 5 mm). For all data sets the efficiency drops to 1/10 of the maximum value for a ratio V_{ind}/V_{appl} between 0.8 and 2. This shows that the drop in efficiency relates to the screening of the applied field by the induced voltage. Other than the left-most and right-most curves (they show anomalous behavior), the curves in Figure 5.9 are split into two groups with respect to temperature. A reason for this behavior is not immediately apparent from Equation 2.9.

Our data show a baseline for the efficiency at about 0.1%. The reason for this is not clear. It is more than 2 orders of magnitude below the maximum efficiency and we can consider it therefore irrelevant for our discussion of the primary effects. The actual loss mechanism is considered to be the recombination of ions and electrons once the effective electric field becomes small enough to no longer remove the electrons effectively from the ionization region. We quantify this phenomenon using recombination losses. This concept succesfully describes the behaviour of ionization chambers [27] and was more recently applied to gas catchers [60].

The recombination loss for a parallel plate ionization chamber is given by Equa-

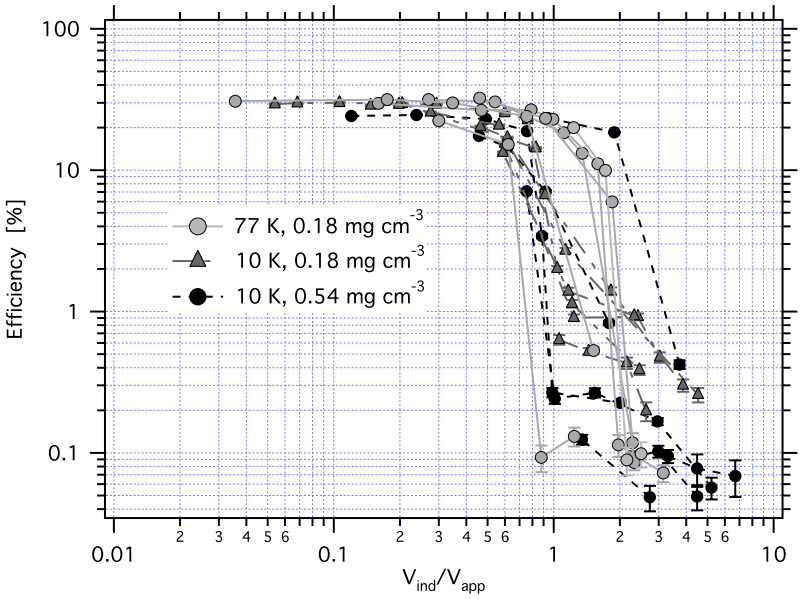

Figure 5.9: *The combined efficiency of ion survival and transport as a function of the ratio of induced to applied voltage. Data points taken for the same ionization rate density by varying the applied field are connected.*

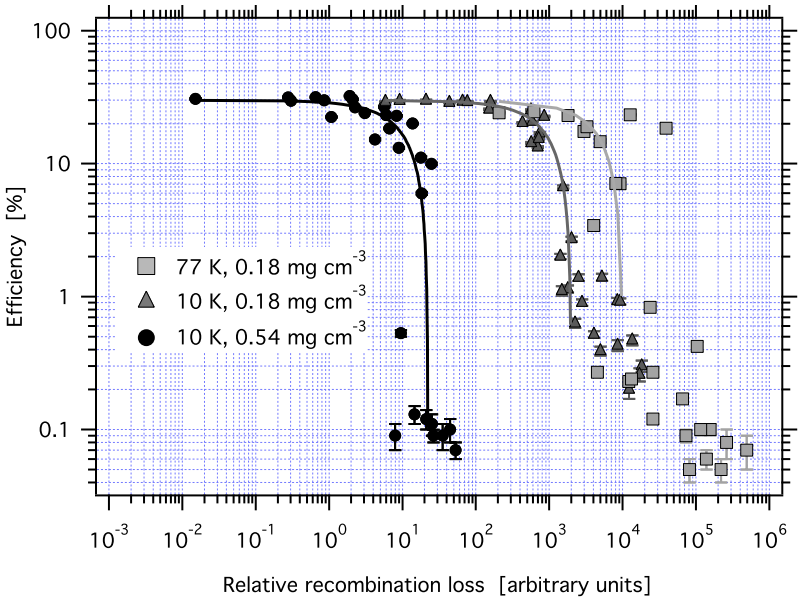

Figure 5.10: *The combined efficiency of ion survival and transport as a function of the relative recombination loss as calculated by Equation 5.3.*

tion 2.8. Using the fact that the ion mobility scales with the ratio of temperature and pressure T_g/P we define the following relative recombination loss

$$f_{rel} = \frac{Q\alpha}{E^2(T_g/P)\mu_-} , \tag{5.3}$$

where Q is the ionization rate ($\mathrm{cm}^{-3}\,\mathrm{s}^{-1}$), α is the ion-electron recombination coefficient, μ_- the electron mobility and E the applied electric. The charge density is dominated by helium ions and thus governed by helium ion recombination. As we measure the transport efficiency of radon ions, the recombination coefficient of radon is needed, which is yet unknown. One might assume radon to be similar in its behaviour to helium because both are noble gases. For the helium gas densities and temperatures used in this experiment 3-body recombination dominates the 2-body recombination by an order of magnitude (see section 2.5).

In the following analysis we only consider the 3-body recombination coefficient α_3 is considered for α. The 3-body recombination coefficient α_3 shows a temperature dependence of $T_g^{-2.5}$ between 200 K and 295 K (see Reference [118] and Section 2.6). We extrapolate the results of [118] down to 10 K and include a $T_g^{-2.5}$ dependence for the α_3 coefficient in the calculation of f_{rel}. It is also well documented that recombination depends strongly on the electron temperature (see Section 2.6), which in turn depends on the ionization method and can be much higher than the gas temperature. The temperature or more generally the energy distribution of the electrons, is not known in our case of ionization by a fast proton beam. We therefore do not take this effect into account. If the electron temperature is much different from the gas temperature, it is conceivable that any modification of the recombination coefficient would be independent of the gas temperature. Thus it would not affect the relative recombination loss. The electron mobility μ_- is taken from [88]. The ^{219}Rn ion extraction efficiency ϵ_{extr} from the ionization region is given by

$$\epsilon_{extr} = \epsilon_{max}(1 - f) , \tag{5.4}$$

where ϵ_{max} is the maximum efficiency obtained in off-line conditions ($\sim 30\%$) and f is the absolute recombination loss factor (see Equation 2.8). The absolute recombination loss can be expressed as

$$f = Kf_{rel} , \tag{5.5}$$

where K is a constant within our measurements. Figure 5.10 shows the efficiency as a function of the relative recombination loss as calculated with Equation 5.3. The data at 1 bar room temperature equivalent density show a rather weak temperature dependence; the measurements at 10 K show a strong density dependence. Curves of the form $\epsilon_{extr} = 30(1 - Kf_{rel})$ are shown as guide to the eye. The sharp drop in efficiency indicates that as soon as recombination sets in due to the incomplete separation of ions and electrons, there is a positive feedback accelerating the recombination. The fact that for a certain temperature and density a typical dependence

of the form Equation 5.4, shows that the tolerable ionization rate density increases with the square of the applied electric field. Maximizing the electric field is therefore a major design consideration for gas ion catchers.

5.3 Mobility measurements of ^{219}Rn ions in cryogenic noble gases

The feasibility of a noble gas catcher depends on the extraction efficiency and on how fast an ion can be extracted from the stopping volume. The extraction time should be shorter than the lifetime of the exotic nucleus. The mobility of positive ions is a factor which determines its extraction time from a noble gas ion catcher.

5.3.1 ^{219}Rn mobility experiment

The experimental setup used for the mobility measurements is identical to that in Figure 6.1b. The voltages on the electrodes are set to have an electric field as uniform as possible throughout the transport region. The SIMION software is used to find an optimum voltage configuration (see Figure 5.11). Within the first 0.15 cm of the ion trajectory, the electric field varies drastically. Along the rest of the trajectory the electric field is constant within 4.5%. Fluctuations of the electric field E are not important as the drift velocity $v_d \propto E$. In the analysis the average E is used. The voltages of the electrodes are lowered proportionately to have lower field strengths. The ^{219}Rn ion transport time through helium, argon and neon gases at different densities are measured. An ion transport time window is set by pulsing the voltages applied to the ^{223}Ra source and the collection foil. The schematic of the electronics for the pulsed measurements is given in Figure 5.12. Pulsing is applied in such a way that the ion transport is blocked by increasing the foil voltage to a high positive value, and decreasing the source and bottom electrode voltage to zero. The repetition rate is 1 Hz. The square pulse is fed into the TTL triggered voltage sources which are connected to the foil and the source plus bottom electrode. This square pulse from the pulse generator provides the transport window for the ions.

The width of the transport window is the time during which the electric field is favorable for the ion transport from the source to the collection foil. The number of ions transported is measured as a function of transport window width. If the transport window is larger than the transport time the ions that survived after the thermalization are transported to the collection foil. The fraction of the ions that arrives at the collection foil increases linearly with increasing transport window width. No ions will be transported to the collection foil if the transport window width is smaller than the ion transport time t_0. Thus t_0 is the maximum transport window width for which the ion intensity is zero. The value of t_0 can be found by extrapolating the data points in the plot of the ion intensity versus transport

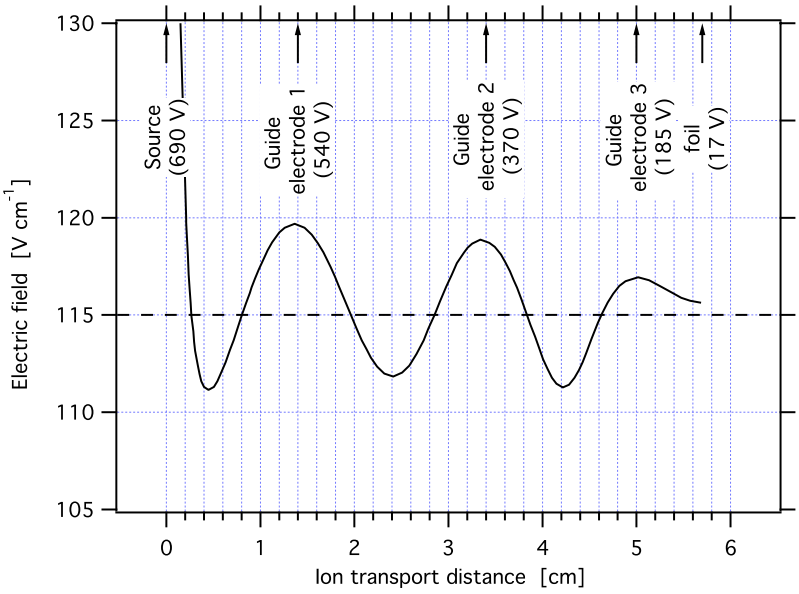

Figure 5.11: *Electric field profile along the ion transport trajectory. Electrode positions and the maximum voltages applied are marked on the top axis.*

window width to the zero intensity value (see Figure 5.14). We can find the mobility μ of the ions for the applied field from the relation

$$\mu = \frac{L}{Et_0}\,, \tag{5.6}$$

where L (= 56 cm) is the distance between the source and the collection foil and E is the applied electric field (calculated using the SMION, Figure 5.11). Figure 5.13 shows the pulsing scheme applied in this experiment. A pulse of 1 μs width from a pulser is used to trigger the pulse generator which produces a square pulse of 5 V height and adjustable width.

5.3.2 Results

The electric fields used in these experiments are 115 V cm^{-1}, 58 V cm^{-1} and 29 V cm^{-1}. The ^{219}Rn ion transport time for 1, 2 and 3 bar room temperature equivalent density helium at 77 K and 1 bar room temperature equivalent density argon and neon at 77 K are measured. The buffer gas pressure is measured at the room temperature side of the setup and the experimental cell is at 77 K. The ratio of the volumes at room temperature (where the pressure is measured) and cryogenic temperature for this experimental setup is $V_w / V_c = 0.55$. Equation 4.10 yields

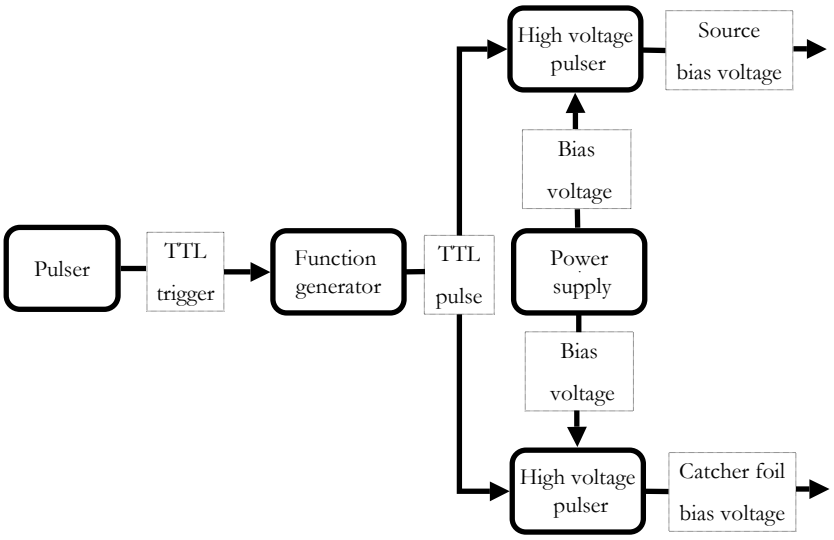

Figure 5.12: *Schematic diagram of the electronics setup used for the mobility measurement.*

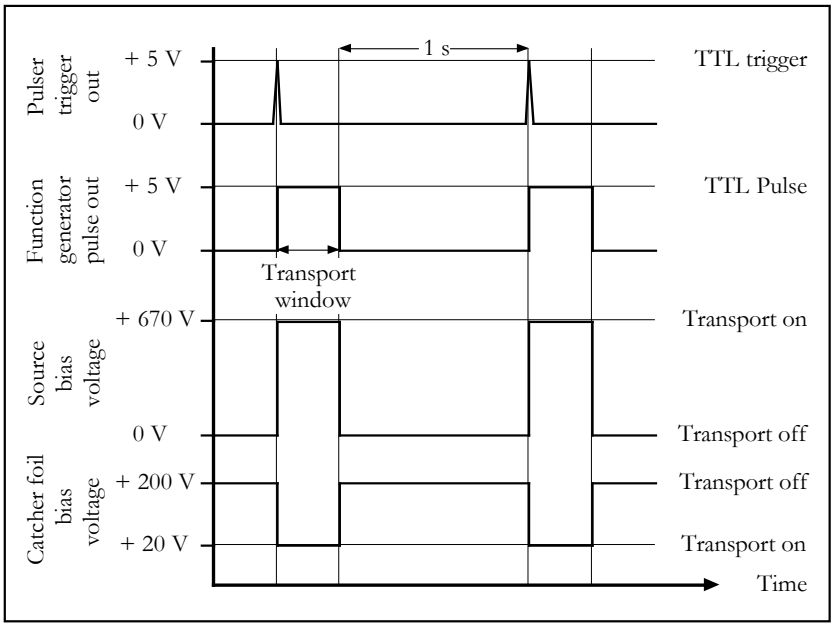

Figure 5.13: *Pulsing scheme used for the mobility measurement.*

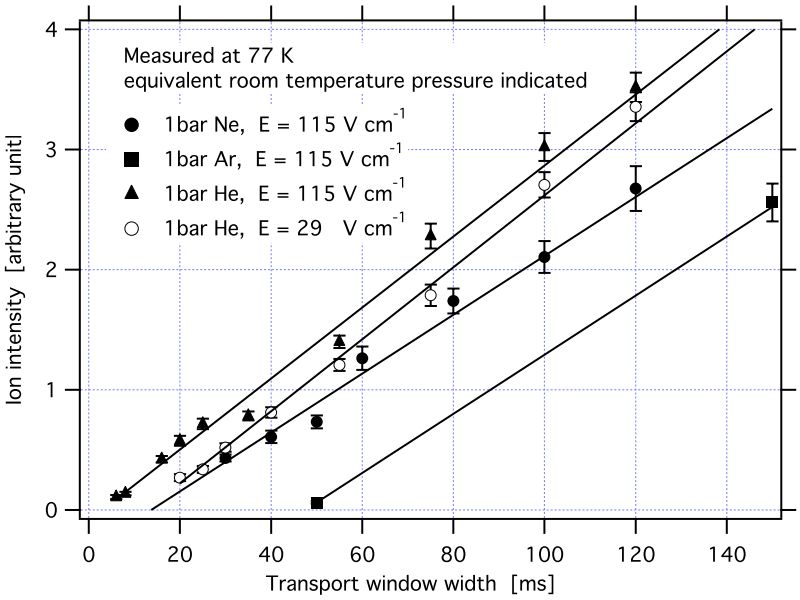

Figure 5.14: *Transported ion intensity as function of transport window width measured for the helium, neon and argon at 77 K at a density of 2.57×10^{19} cm^{-3}. Extrapolating the data to an ion intensity equal to zero gives the ion transport time t_0.*

a 4.4 % lower density inside the experimental cell than what would be expected from the pressure measured at the room temperature side. Figure 5.14 shows the ^{219}Rn ion intensity as a function of the transport window width for a number of experimental conditions. Extrapolation of the data points to zero ion intensity yields the ion transport time t_0. With this ion transport time t_0 deduced, the ion mobility for the given experimental conditions can be found from Equation 5.6.

Conventionally, mobility data are quoted in terms of the reduced mobility μ_{red} (see Equation 2.7) as a function of the ratio of the electric field to the gas density E/N. Figure 5.15 shows the reduced mobilities of ^{219}Rn ions in helium, argon and neon at 77 K. The experimental results are also tabulated in Table 5.1.

The reduced mobility of ions in the limit of vanishing electric field strength $E/N \rightarrow 0$ is referred to as the zero field reduced mobility $\mu_{red}(0)$. This value is obtained by extrapolating the reduced mobility values back to the $E/N = 0$ point. The values of E/N in these experiments are so low that the values μ_{red} obtained directly give $\mu_{red}(0)$. For 1 bar room temperature equivalent density the results are compatible with the reduced mobility of ions with comparable masses to ^{219}Rn (see Table 5.2) and other noble gas ions in helium, neon and argon gases (see Table 5.3). The reduced mobility of ^{219}Rn ions at 2 and 3 bar are rather the same and are less than that at 1 bar room temperature equivalent density helium gas at 77 K (see

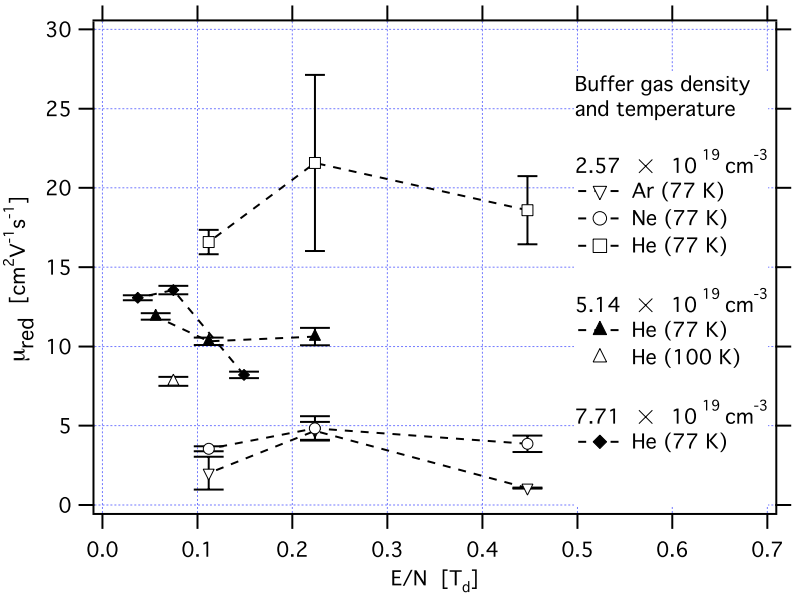

Figure 5.15: *Measured reduced mobilities μ_{red} of ^{219}Rn ions in helium, neon and argon gases as a function of the ratio E/N. The buffer gas densities and temperatures used for the measurements are indicated in the legend.*

Table 5.1: *Reduced mobility of ^{219}Rn ion in helium, neon and argon gases.*

Buffer gas	Buffer gas density [cm^{-3}]	μ_{red} [cm^2 V^{-1} s^{-1}]	E/N [Td]	T_g [K]
helium	2.57×10^{19}	18.6(21)	0.45	77
		21.6(56)	0.22	77
		16.6(8)	0.11	77
helium	5.14×10^{19}	10.6(2)	0.22	77
		10.3(2)	0.11	77
		11.9(2)	0.06	77
		7.79(28)	0.07	100
helium	7.71×10^{19}	8.2(2)	0.15	77
		13.6(3)	0.07	77
		13.1(2)	0.04	77
neon	2.57×10^{19}	3.9(6)	0.45	77
		4.8(8)	0.22	77
		3.55(15)	0.11	77
argon	2.57×10^{19}	1.10(3)	0.45	77
		4.7(6)	0.22	77
		2(1)	0.11	77

Table 5.2: *Reduced mobility in the limit of vanishing electric field strength ($E/N \rightarrow 0$) $\mu_{red}(0)$ of ions with comparable masses to ^{219}Rn in helium, neon and argon gases.*

Buffer gas	Ion	T_g [K]	$\mu_{red}(0)$ $[cm^2V^{-1}s^{-1}]$	Reference
He	Hg^+	300	19.7(8)	[41]
He	U^+	300	15.8(6)	[41]
He	Tl^+	300	19.1(8)	[40]
Ne	Hg^+	300	5.96(24)	[41]
Ne	Tl^+	300	5.92(24)	[40]
Ar	Hg^+	300	1.85(7)	[41]
Ar	Tl^+	300	1.91(8)	[40]

Figure 5.15). One may speculate that polarization interaction induced clustering of helium atoms around ^{219}Rn ions in high-density, low-temperature helium gas may be the reason. There are insufficient data to draw definite conclusions regarding the observed density dependence.

5.4 Conclusion

We have demonstrated large stopping and transport efficiencies of ions in noble gas stopping media of low purity in a container that is not ultra-high vacuum compatible by in-situ purification of the noble gas upon cooling to below 90 K. The measured efficiencies at low temperature are comparable to those achieved with ultra-high purity gas catchers at room temperature. However, constructing a cryogenic noble gas ion catcher operated at liquid nitrogen temperature is technically easier. To reach the required purity level of less than 1 ppb, room temperature gas cells have to be pumped to ultra high vacuum and baked for a long time before being operational. In cryogenic gas cells this is achieved without long pre-preparations and it is in this sense more reliable. It may therefore be a more practical choice.

In off-line measurements the combined ion survival and transport efficiency for ^{219}Rn ions saturated below about 90 K, reaching 28.7(17)% in helium, 22.1(13)% in neon, and 17.0(10)% in argon gases. The main result of these measurements is that nothing happens after the ions are slowed down. The measured efficiency is the result of charge exchange during slowing down and as such represents a fundamental upper limit to the efficiency of noble gas ion catcher devices. This upper limit depends on the chemical nature and the atomic structure of both the ion and the gas.

On-line results demonstrate the importance of a high electric field to pull ions and electrons quickly apart and as such reduce the neutralisation probability in

the ionization region. Both on-line and off-line measurements demonstrate that cryogenic helium at high density and high electric field is a promising medium for an ion catcher.

The mobility measurements of ^{219}Rn ions in helium, neon and argon at 77 K gave values comparable to those obtained earlier for xenon in the same gases.

Table 5.3: *Reduced mobility in the limit of vanishing electric field strength ($E/N \rightarrow 0$) $\mu_{red}(0)$ of noble gas ions in helium, neon and argon gases at different temperatures T [39, 40, 41, 122]*

helium		
Ion	T_g [K]	$\mu_{red}(0)$ [cm^2 V^{-1} s^{-1}]
He^+	300	10.3(1)
He^+	77	14.7
He^+	4.35	22.2(4)
He_2^+	300	16.7(2)
Ne^+	300	20.0(4)
Ne^+	82	19.0(8)
Ne^+	4.35	17.5
Ne^{2+}	300	17.8(9)
Ar^+	293	20.3(10)
Ar^+	170	20.5(10)
Ar^+	82	18.8(8)
Ar^+	4.35	16.8(3)
Ar^{2+}	300	18.9(9)
Kr^+	300	18.6(4)
Kr^+	82	17.7
Kr^+	4.35	16.4(3)
Kr^{2+}	300	16.7 (8)
Kr^{2+}	82	17.4
Xe^+	295	16.5(8)
Xe^+	82	17.5
Xe^{2+}	300	17.7(9)
Xe^{2+}	82	17.2(7)

neon		
Ion	T_g [K]	$\mu_{red}(0)$ [cm^2 V^{-1} s^{-1}]
Ne^+	300	4.07(04)
Ne^+	216	2.95(03)
Ne_2^+	300	6.16(06)
Ne_3^+	77	5.40(54)
$Ne^+(^2P_{1/2})$	78	5.3(1)
$Ne^+(^2P_{3/2})$	78	5.64(06)
$Ne^{2+}(^3P)$	306	6.95(31)
$Ne^{2+}(^1D)$	306	6.25(19)
$Ne^{2+}(^1S)$	306	8.21(25)
Ar^+	77	6.39(13)
Xe^+	300	5.75(29)
Xe^{2+}	300	5.47(28)

argon		
Ion	T_g [K]	$\mu_{red}(0)$ [cm^2 V^{-1} s^{-1}]
Ne^+	294	3.29(23)
Ar^+	77	2.1(1)
Ar_3^+	77	1.65(17)
Ar^+	300	1.53(02)
Ar^{2+}	300	2.49(03)
$Ar^{2+}(^3P)$	300	2.64(08)
$Ar^{2+}(^1D)$	300	2.29(07)
Ar_2^+	77	1.77(09)
Ar_2^+	300	1.83(02)
Kr^+	300	2.16(04)
Xe^+	294	2.07(15)

6 Superfluid helium ion catcher

A series of off-line experiments was carried out at the Department of Physics, University of Jyväskylä (JYFL), Finland in 2001-2002 to investigate the possibility to use liquid helium as ion catcher stopping medium. The measurements employed ^{219}Rn ions recoiling from ^{223}Ra (see Section 4.2.1) as an ion source. Among the reported results was the first observation of the extraction of heavy positive ions across the superfluid helium surface [56, 57, 108]. The efficiency for extraction across the liquid surface was 23(4)% at 1.60 K, the release time was 90(10) ms at 1.50 K and the barrier for positive ions moving through a free superfluid-helium surface was 19.4(45) K. Earlier experiments which tried to extract positive ions/snowballs from liquid helium were unsuccessful [15]. A difference is that in earlier works mostly helium ions were investigated. The electronic structure of heavy ions may have a relation to the different behavior observed in the JYFL experiments.

The experiments described in this section aim towards a better understanding of the ion extraction at the superfluid-vapor interface. Further, as a new idea the possibility to enhance the ion extraction efficiency by second sound assisted superfluid surface evaporation is also investigated.

6.1 Extraction of ^{219}Rn ions across the superfluid-vapor interface

6.1.1 Experimental setup

The experiments were carried out inside a helium bath-cryostat working in the temperature range of 1.0 K to 1.8 K (see Chapter 4).

The principle of this experiment consists of five consecutive steps:

1. Thermalization of ^{219}Rn recoil ions in superfluid helium where they spontaneously form snowballs (see Section 3.1).
2. An electric field pushes the snowballs towards the superfluid-vapor interface.
3. Ions are extracted across the superfluid-vapor interface (see Section 3.5).
4. The extracted ions are transported by an electric field to an aluminum catcher foil, from where
5. α-particles are detected with a surface barrier spectrometer.

An open ^{223}Ra α-decay-recoil source was mounted at the bottom of the experimental cell. Several ring electrodes are used to provide a favorable static electric field to transport the ions from the source to a thin aluminum catcher foil. The experimental cell is cooled down to superfluid temperature and then helium gas from a room temperature buffer volume is let in to be condensed. The buffer volume filled with 1 bar helium gas at room temperature gives 23 cm^3 superfluid helium on condensation. The volume profile of the experimental cell is known, therefore the height of the superfluid helium can be controlled with an accuracy of ~ 0.5 mm by admitting the appropriate amount of buffer volume fillings to the cold cell. In the experiments described here the ^{223}Ra source was covered by 6 mm of liquid helium.

As long as the source is above the superfluid helium surface, α-particles from the source can be recorded by the α-particle detector. Once the α-particles from the source can no longer be recorded by the detector, an amount of superfluid helium sufficient to cover the source with about 0.4 mm (the range of α-particles in liquid helium) is condensed. An applied electric field has been designed with a small radially focusing component at the superfluid helium surface in order to achieve radial confinement of the ions. Displacement of ions more than a few millimeters away from the cell axis would lead to transport loss. If an electric field is applied to guide positive ions from the source to the foil two sets of α-lines can be detected. One set corresponds to the ions which decay at the superfluid-vapor interface; the second set originates from the ions which are extracted across the superfluid-vapor interface and are transported to the aluminum foil and decay there. As explained in Section 4.2.3 both sets can be unambiguously identified because of the different energy loss. Different isotopes are identified based on their known α energies. The ^{223}Ra α-lines are not seen in either of these sets since ^{223}Ra is the mother nucleus and as such does not recoil out of the source. With this setup two sets of experiments were carried out to measure the snowball efficiency and investigate the ion extraction across the superfluid-vapor interface.

Both experiments were performed with similar setups; they are referred to as experiment A (see Figure 6.1a) and experiment B (see Figure 6.1b). The differences between experiment A and B are the shape of the ^{219}Rn recoil open ion source, the source strength, the number of intermediate guiding electrodes and the distance

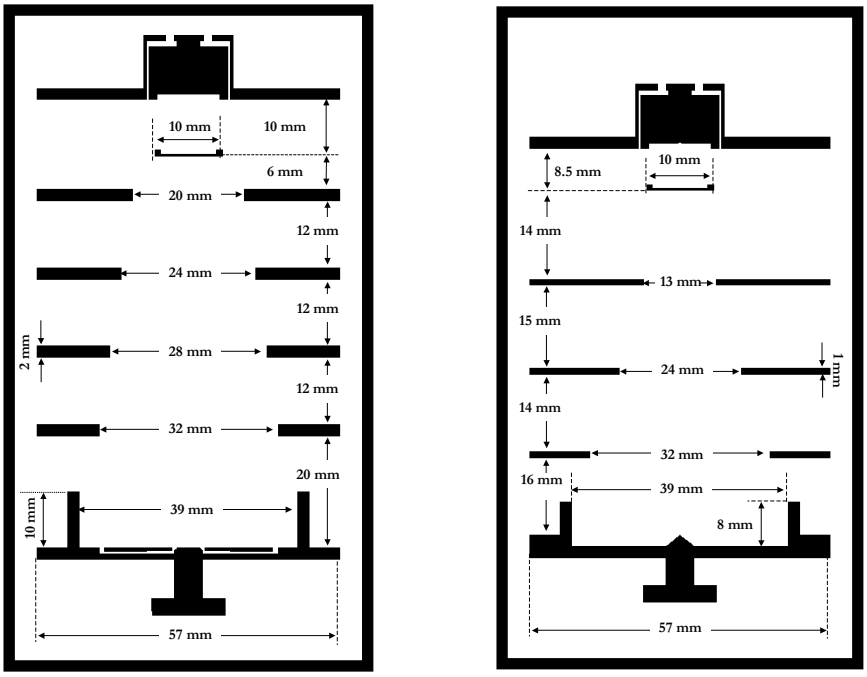

(a) Experiment A. **(b)** Experiment B.

Figure 6.1: *Cross-sectional view of the experimental cells used in experiments A and B.*

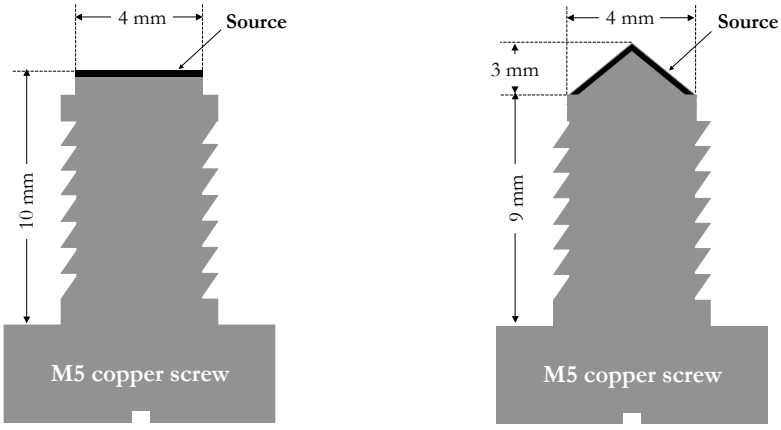

(a) Experiment A. **(b)** Experiment B.

Figure 6.2: *Schematic representation of the ^{219}Rn ion open source used in experiments A and B.*

between the source and the aluminum catcher foil. The open source in experiment A is deposited on a flat copper tip (see Figure 6.2a) and in experiment B on a cone-shaped copper tip (see Figure 6.2b). The cone-shaped source was used in order to avoid deposition of ^{223}Ra on the lateral side of the copper screw during the source preparation. The strength of the ^{223}Ra source was 21000 Bq in experiment A and 5000 Bq in experiment B at the start of the experiment. Experiment A is equipped with four guiding electrodes whereas B is equipped with three. The source-foil distances in the experiments A and B are 70 mm and 62 mm respectively. The number of guiding electrodes and the distance between the recoil ion source and the catcher foil have no effect on any of the results because once the ions are extracted out of the superfluid helium they are transported with 100% effiiciency to the catcher foil by a static electric field.

The main objective of experiment A was to find the effect of the applied electric field on the snowball efficiency which is the fraction of ^{219}Rn recoil ions transported to the superfluid-vapor interface after thermalization. Experiment B was performed to investigate the temperature dependence of the extraction efficiency of ions across the superfluid-vapor interface.

6.1.2 Results

A fraction of the recoil ions is neutralized due to charge-exchange processes during slowing down and thermalization. The surviving thermalized ions are transported to the superfluid-vapor interface by the electric field.

A fraction of the ions reaching the superfluid-vapor interface can be extracted into the vapor phase; the remaining ions decay at the interface. Because there are few electrons present at the interface, we assume there is no neutralization at the interface. The extracted ions are transported to the aluminum catcher foil and decay there. The snowball efficiency ϵ_{sb} is determined as the ratio of the sum of ^{219}Rn ion decays at the catcher foil N_{foil} and ^{219}Rn ion decays at the superfluid-vapor interface N_{surf} to the total ^{219}Rn recoil ions emitted from the source $N_{recoils}$:

$$\epsilon_{sb} = \frac{N_{surf} + N_{foil}}{N_{recoils}} = \epsilon_{surf} + \epsilon_{foil} \tag{6.1}$$

where ϵ_{surf} is the fraction of total ^{219}Rn recoils that decay at the superfluid-vapor interface and ϵ_{foil} is the fraction of total ^{219}Rn recoils that decay at the foil. The fraction ϵ_{foil} is the total efficiency of the system. These efficiencies are directly deduced from the observed α-line intensities. The extraction efficiency ϵ_{extr} is the fraction of the snowballs arriving at the surface that are extracted across the superfluid-vapor interface, i.e. the ratio of total efficiency ϵ_{foil} to the snowball efficiency ϵ_{sb},

$$\epsilon_{extr} = \frac{\epsilon_{foil}}{\epsilon_{sb}} = \frac{\epsilon_{foil}}{\epsilon_{surf} + \epsilon_{foil}} \, . \tag{6.2}$$

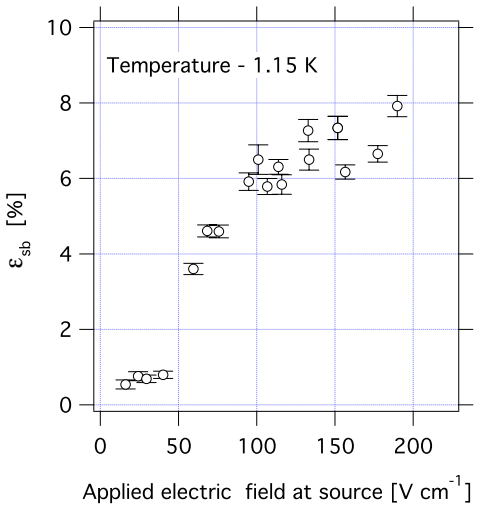

(a) Experiment A.

Figure 6.3: *Snowball efficiency as a function of electric field at 1.15K.*

Figure 6.3 shows the ^{219}Rn snowball efficiency as a function of the electric field in the vicinity of the recoil ion source obtained with the experimental configuration A. A gradual increase and saturation of the snowball efficiency with increasing electric field is observed. The saturation of the snowball efficiency occurs for electric field strengths above about 180 V cm^{-1}. A measurement series was performed within the temperature range 1.15 to 1.6 K. Figure 6.4a shows the snowball efficiency as a function of inverse temperature from experiment A. No significant temperature dependency is observed. An average snowball efficiency of 5.36(13)% is observed for temperatures between 1.15 and 1.6 K with an electric field of 180 V cm^{-1} in all the measurements. A similar measurement in experimental condition B yields an average snowball efficiency of 1.04(6)% for temperatures between 1.2 and 1.6 K (see Figure 6.4b). Experiment B was performed within the temperature range 1.15 to 1.8 K. The snowball efficiency at 1.8 K could not be extracted because of low statistics and the large low-energy tail of the α spectral lines.

Figure 6.5b shows the total efficiency ϵ_{foil} as a function of inverse temperature obtained in experimental configuration B. Measurements were performed within the temperature range 1.2 K to 1.8 K with an applied electric field of 180 V cm^{-1}. Figure 6.5a shows results from similar measurements in experimental configuration A. An increase in total efficiency with increasing temperature is observed.

Figures 6.6a and 6.6b show the extraction efficiency ϵ_{extr} as function of inverse temperature obtained from experiments A and B. The point at 1.8 K in experiment B is calculated using the average snowball efficiency of 1.05%. It clearly shows an increase in extraction efficiency with increasing temperature.

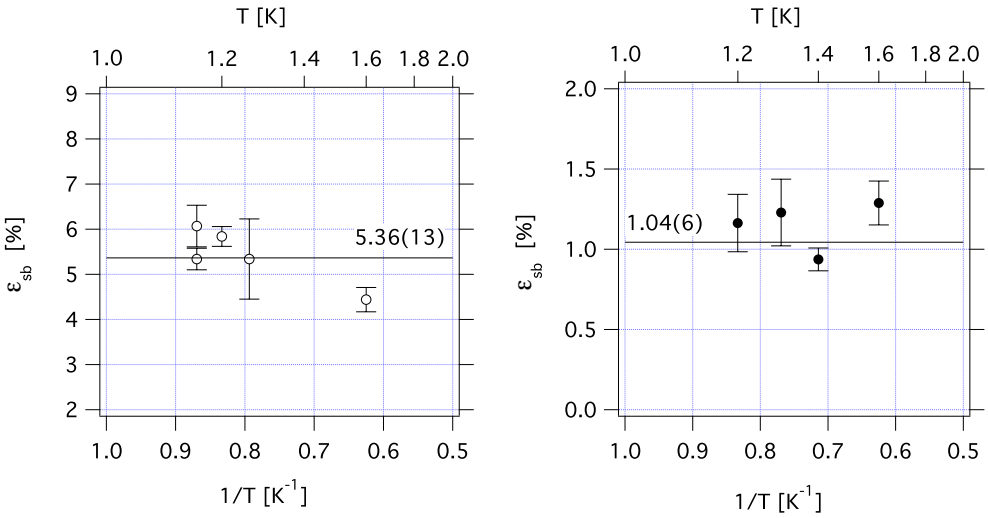

(a) Experiment A. **(b)** Experiment B.

Figure 6.4: *Snowball efficiency ϵ_{sb} as a function of the inverse temperature $1/T$. The experiments were performed with an electric field of 180 V cm^{-1} at the source.*

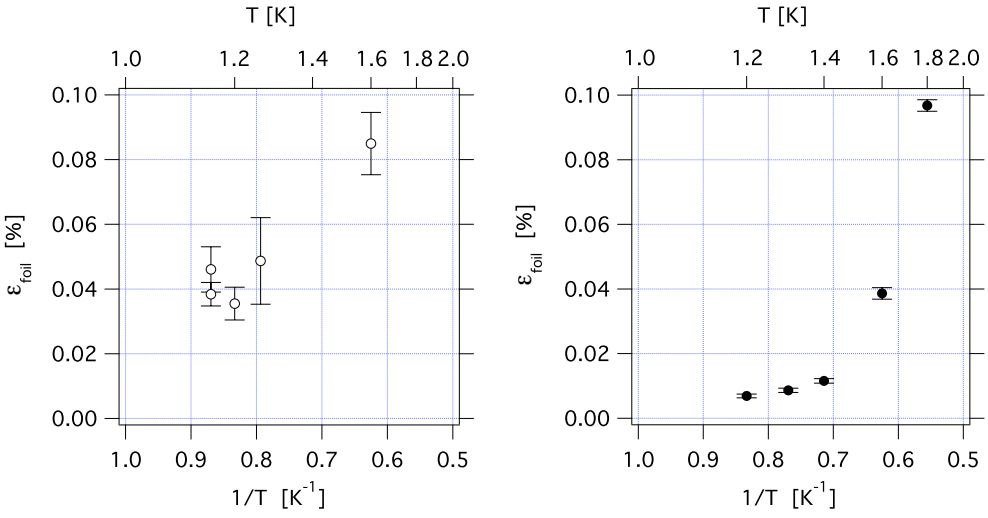

(a) Experiment A. **(b)** Experiment B.

Figure 6.5: *Total efficiency ϵ_{foil} as a function of inverse temperature $1/T$. The experiments were performed with an electric field of 180 V cm^{-1} at the source.*

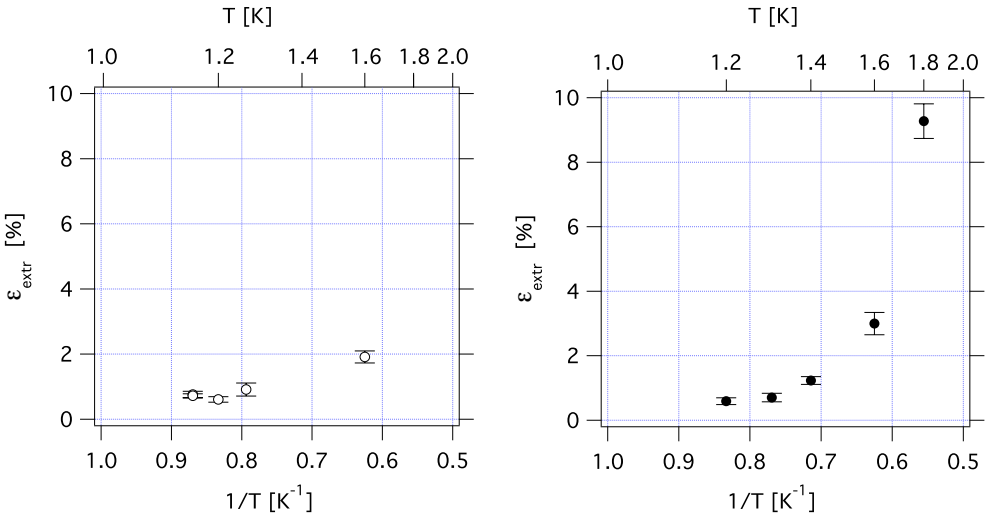

(a) Experiment A. **(b)** Experiment B.

Figure 6.6: *Extraction ϵ_{extr} efficiency as a function of inverse temperature $1/T$. The experiments were performed with an electric field of 180 V cm^{-1} at the source.*

6.1.3 Discussion

The growth and saturation of the snowball efficiency as a function of electric field observed in Figure 6.3 can be explained in terms of recombination losses. The ions undergo neutralization during the slowing down due to charge exchange processes. The region around the ion source is rich in excess electrons due to the ionization of helium atoms by recoil ions and the α-particles emitted from the recoil ion source. The range of the recoil ions and the α-particles in the liquid helium are about 0.55 μm and 0.4 mm respectively. If the ^{219}Rn snowballs are not transported out of this region fast enough they will neutralize as a result of electron-ion recombination. Once the ions are out of the electron-rich region, the neutralization is unlikely along the rest of the transport due to the very low electron density. The drift velocity of snowballs is proportional to the applied electric field (see Section 3.3). The snowball efficiency ϵ_{sb} can be represented in terms of the recombination loss factor f as

$$\epsilon_{sb} = \epsilon_{sb}^{sat}(1 - f)\,, \tag{6.3}$$

where ϵ_{sb}^{sat} is the saturation value of the snowball efficiency as a function of electric field. The recombination loss factor for a parallel plate ionization chamber is used as f (see Section 2.4, Equation 2.8). At a constant temperature and ionization rate, f is proportional to E^{-2}, where E is the applied electric field at the ionization region.

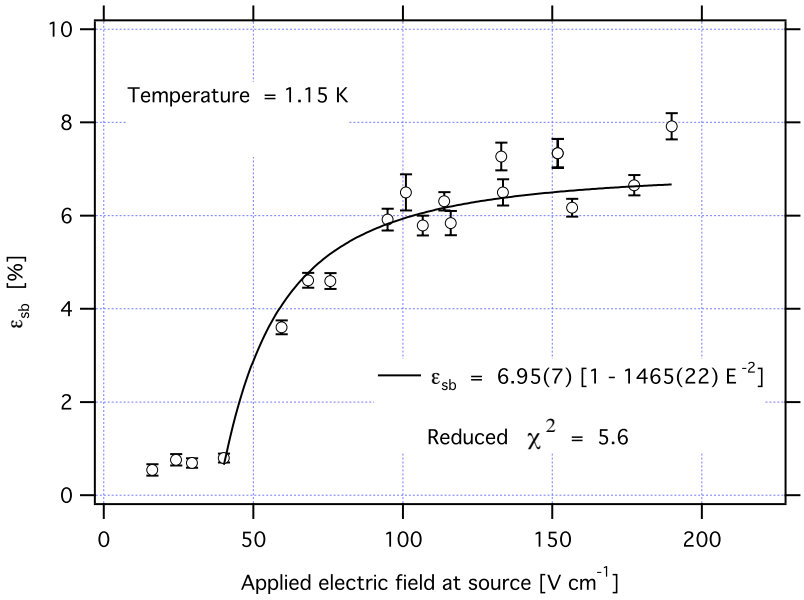

Figure 6.7: *Snowball efficiency ϵ_{sb} as a function of electric field E at the source. The function $\epsilon_{sb}^{sat}(1 - KE^{-2})$ is fitted to the data. The snowball efficiency reaches a saturation value of 7.0% at electric fields above about 180 V cm^{-1} at the source.*

Using this result the snowball efficiency can be expressed as

$$\epsilon_{sb} = \epsilon_{sb}^{sat}(1 - KE^{-2}) \,, \tag{6.4}$$

where K is given by

$$K = \frac{Q\alpha_{SF}d^2}{6\mu_+\mu_-} \,, \tag{6.5}$$

where Q is the ionization rate desnity (helium ion-electron pairs cm^{-3} s^{-1}), α_{SF} is the recombination coefficient of ions in superfluid helium (see Section 3.4), μ_+ and μ_- are the positive ion and electron mobility (see Section 3.3) and d is the size of the ionization region along the applied electric field. As the range of the ionizing particles (recoils and alphas) is much smaller than the diameter of the source, we consider a cylindrical ionization region above the source with a radius equal to that of the source (4 mm). This ionization region consists of two parts: (1) a region of height 0.55 μm where the recoil ions with an energy of about 100 keV are thermalized, (2) a region of height 0.4 mm being the volume where the α-particles with an average energy of about 6.5 MeV are stopped. Recoiled ^{219}Rn ions are thermalized in the first region and transported through the second region. The ^{223}Ra source strength at the time of the experiment was about 5000 Bq. The Q associated with recoil ions, i.e. in the region 1 is about 1.3×10^{12} cm^{-3} s^{-1} and the Q

Table 6.1: *Saturation value of snowball efficiency ϵ_{sb}^{sat} for different ions in superfluid helium.*

Ion	ϵ_{sb}^{sat} [%]	T [K]	Reference
^{219}Rn	6.95(7)	1.15	This work
^{12}B	30(3)	1.7	[107]
^{12}N	10(3)	1.7	[107]
^{8}Li	30(3)	1.7	[107]

associated with the α-particle range, i.e. in the region 2 is about 0.2×10^{12} cm^{-3} s^{-1}. In this calculation, we assumed on average 40 eV is needed for the creation of a helium ion-electron pair (the same as in gaseous helium) and estimated the total number of recoils entering the superfluid helium to be 0.65 times the ^{223}Ra source strength and the total number of α-particles causing ionization of the helium to be 1.1 times the ^{223}Ra source strength. Although Q in region 1 is an order of magnitude larger than in region 2 the α-particle range is about 3 orders of magnitude larger than the recoil range. The factor Qd^2 in Equation 6.5 is thus about 5 orders of magnitude larger in region 2 than in region 1. The ionization by the recoils is thus irrelevant for the recombination loss and the parameters of region 2 are used in the calculation. The recombination coefficient α_{SF} of ions in superfluid helium at a temperature of 1.15 K is about 2.7×10^{-6} cm^3 s^{-1} (see Section 3.4). The positive ion mobility μ_+ and electron mobility μ_- in superfluid helium at 1.15 K are about 1.25 cm^2 V^{-1} s^{-1} and 2.2 cm^2 V^{-1} s^{-1} respectively (see Section 3.3). Using these values, K is calculated to be 436 V cm^2. Thus the value of f for an electric field of 50 V is 0.17. As the value K in region 2 and region 1 differ only by the values of Q and d, f in region 1 is five orders of magnitude less than in region 2. This shows that the condition for Equation 6.4, i.e. $f < 1$ is satisfied here.

Figure 6.7 shows the best fit of Equation 6.4 to the snowball efficiency vs. electric field data. ϵ_{sb}^{sat} and K obtained from the fit are 6.95(7)% and 1465(22) respectively. The value of ϵ_{sb}^{sat} from the fit is in good agreement with the experimental values obtained at electric fields higher than about 180 V cm^{-1} (5.4%, see Figure 6.4a). K obtained form the fit is about 4 times larger than the calculated value. There should be no error on α_{SF} and μ_-. There is a chance for a 25% error on μ_+ as we used the ^{4}He ion mobility instead of the ^{219}Rn ion mobility. The largest error may arise form the calculation of the ionization rate Q as we considered a uniform energy loss of the α particles throughout the ionization region. Given these uncertainties, the calculated and experimentally determined value of K are in good agreement.

The saturation of the snowball efficiency indicates that all the thermalized snowballs are moved out of the electron-rich region before recombination-neutralization. The saturation value of 6.95(7)% shows the charge exchange cross section limit of ^{219}Rn ion thermalization in superfluid helium. The charge exchange cross section

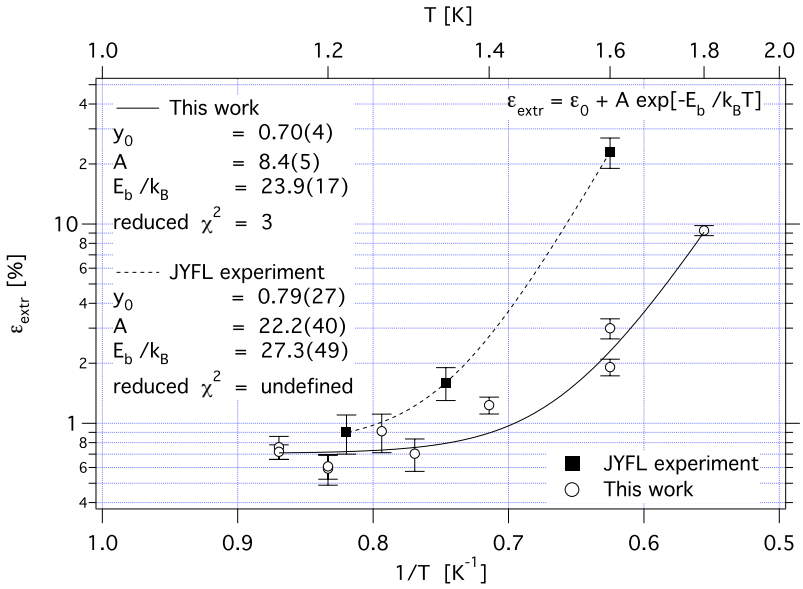

Figure 6.8: *Extraction efficiency ϵ_{extr} as a function of inverse temperature $1/T$. The lines represent a constant plus an exponential function obtained by fitting to the data points.*

limit of ^{219}Rn ion survival in helium gas is about 30% (see Section 5.1.2).

Takahashi et al. [109, 107] measured snowball efficiencies of ^{12}B, ^{12}N and ^{8}Li ions in superfluid helium (see Table 6.1). Positively charged impurities were created through the injection of fast nuclear beams into superfluid helium. The snowballs involving a radioactive core ion were transported under a static electric field and were traced through the measurement of the radioactive decay of the impurity ions. Electric fields of 100 V cm^{-1} to 500 V cm^{-1} were used to transport the snowballs out of the stopping region. This shows that the snowball efficiencies are different for different species of impurity ions.

The offset in snowball efficiency observed at electric fields lower than about 40 V cm^{-1} may be due to the shielding of the applied electric field by an induced field created by the charge polarization at the ionization region. A similar effect was observed in weakly ionized helium gas (see section 2.4). The main difference between the superfluid and gas cases is the different nature of the electron and ion mobility. The electron mobility in helium gas is several orders of magnitude higher than that of positive ions, whereas in superfluid helium they are very similar (see Sections 2.1, 2.2 and 3.3). Therefore in helium gas even a very small applied electric field will drive the ionized gas into a positive ion cloud. But in superfluid helium the ions and the electrons are removed at roughly the same rate and comparatively higher electric fields are necessary to quench the counter-balancing polarization field.

Both experiment A and B show a temperature independent snowball efficiency at high electric fields (see Figures 6.4a and 6.4b). The average snowball efficiency observed in experiment B is 5 times smaller than that in experiment A. No explanation of this difference is apparent. It may be due to a problem with the recoil source strength determination.

The total efficiency obtained in both experiments A and B shows a similar behavior as a function of temperature. An increase in total efficiency with increasing temperature is observed in both experimental configurations. This indicates that an increase in temperature favors the extraction process as the snowball efficiency is temperature independent. The values of total efficiency ϵ_{foil} as a function of temperature obtained in experiment A are higher than in experiment B (see Figures 6.5a and 6.5b). This is due to the high snowball efficiency observed in experiment A compared to experiment B.

Figure 6.8 shows the extraction efficiency as a function of inverse temperature from this experiment and the JYFL experiment [57]. ϵ_{extr} data from both experiment A and B are combined as ϵ_{extr} is independent of the experimental setup. The trend observed in both experiments is similiar. Above $\sim$1.3 K, ϵ_{extr} is compatible with the thermally activated crossing of particles across a potential barrier with height E_b

$$\epsilon_{extr} \propto e^{-E_b/k_B T} \, . \tag{6.6}$$

The fact that ϵ_{extr} below $\sim$1.3 K is much larger than the extrapolation of the thermally activated extraction towards lower temperature, points to another mechanism being dominant below $\sim$1.3 K. The nature of this mechanism is at the moment unknown. The role of quantum tunneling in the extraction can be ruled out due to large mass of the ions as compared to the electron. This mechanism may very well also be present above 1.3 K but it is dominated by the thermal crossing of the barrier. In the absence of evidence to the contrary, we assume this mechanism to be temperature independent with efficiency ϵ_0 and Figure 6.8 shows the best fit of the function

$$\epsilon_{extr} = \epsilon_0 + A exp\left(\frac{-E_b}{k_B T}\right) \tag{6.7}$$

to the data. ϵ_0 is similar for both experiments, i.e. 0.70(4)% in JYFL work and 0.79(27)% in this work. The function gives a perfect fit for JYFL data because the number of data points is equal to the number of fit parameters. The errors on the fit parameters come from the fact that it is a weighted fit with the experimental errors as weights.

Although the trend observed above $\sim$1.3 K in both experiments is compatible with the thermally activated crossing of particles across a potential barrier (see Section 3.6.2), there is quite some difference in ϵ_{extr} and E_b. The reason for this is not clear; over-estimation of transport losses in the analysis of the JYFL experiment may be part of the answer. Given the quality of the temperature sensors used, an inaccuracy in temperature measurement can not explain the difference.

No theoretical model has yet been developed which adequately describes positive ion extraction across the superfluid-vapor interface. The most realistic model for the potential energy barrier was proposed by Stern [103]. According to this model the image charge potential barrier experienced by a unit charge at the superfluid-vapor interface is about 300 K. This is about 15 times higher than our measured result (taking an average barrier height from the data sets shown in Figure 6.8 to be 20 K). This difference may arise from the fact that Stern's model lacks some important physical features of the real situation. Most important is the density profile at the superfluid-vapor interface assumed in the calculation. The width of the interface used in Sterns' calculation is 0.68 nm and the experimentally measured value by Lurio et al. is 0.92(10) nm [71]. For the density variation across the interface, Stern considers a linearly graded transition and sinusoidally rounded corners. A later experimental study by Lurio et al. [70, 71] showed that the actual rate of density change at the superfluid side of the interface is much slower than sinusoidal (see Figure 3.15). Stern's calculation for a Si - SiO_2 interface in the same paper [103] showed that the resulting barrier height strongly depends on the density variation rate. Thus for a more realistic image charge potential barrier calculation one should include the density profile obtained by Lurio et al. If we believe that the potential barrier present is purely of image charge character, there should be no change in barrier height with respect to temperature because the permittivity of the superfluid helium has a temperature dependence of only about 10^{-3} K^{-1}. One more important aspect that is missing in Stern's model is the actual size and structure of the charge carrier. Stern considered a point charge for his calculation, however in reality the size of the snowball is comparable to the width of the interface. We consider it likely that a snowball will deform the liquid helium surface as it comes close enough. Given the fact that image charge potential is very sensitive to the surface density profile, such deformation is expected to have an influence on the image charge potential barrier and thus influence the extraction process. A detailed theoretical study is necessary to understand the mechanism of positive ion extraction across the superfluid-vapor interface.

6.2 Second sound assisted superfluid surface evaporation

Second sound is a quantum mechanical phenomenon exclusively known from the superfluid phase. It is a heat transfer mechanism by an entropy (or temperature) wave (see Chapter 3). A single second sound pulse can maintain an extremely sharp wavefront in temperature rise. T. Furukawa et al. [47] reported transient evaporation of helium at the superfluid helium surface if a second sound thermal pulse impinges onto the superfluid-vapor interface. This result triggered interest to investigate the possibilities to use this phenomenon to release the ions trapped below the superfluid helium surface.

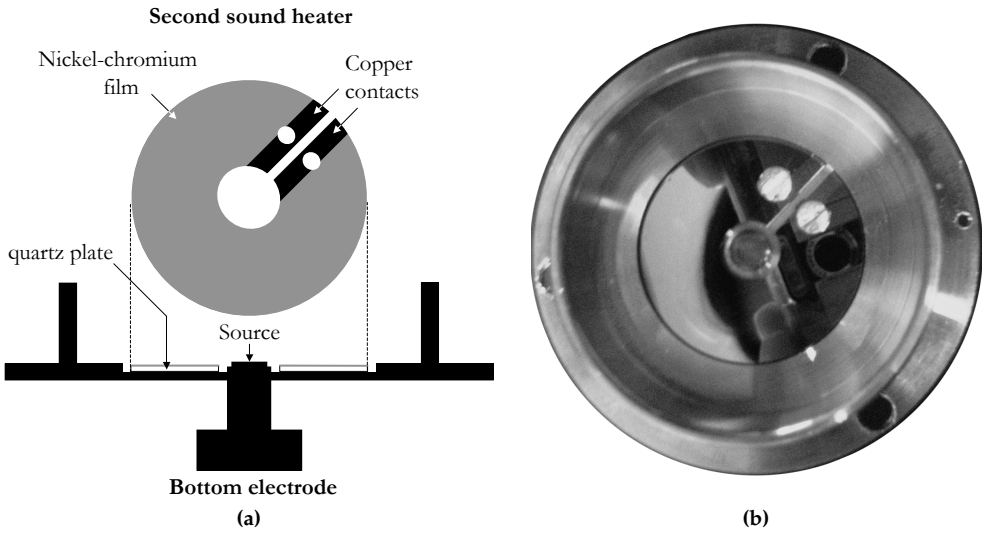

Figure 6.9: ***(a)*** *Schematic side view of the bottom electrode incorporated with the second sound heater and top view of the second sound heater.* ***(b)*** *Photograph of the bottom electrode incorporated with the second sound heater from the top.*

6.2.1 Experimental setup

In an ion catcher device ions are continuously accumulated below the superfluid surface in a potential well, which is formed by the image charge potential and an external electric field normal to the interface. Above a temperature of about 1.6 K, an extraction efficiency of 10-20% is achieved due to thermal excitation of trapped ions. The new idea is to enhance the extraction efficiency in the present setup by evaporating the superfluid helium layer containing the trapped ions and thus release them to the vapor phase. Having second sound pulses at a high enough repetition rate might also reduce the average delay time due to the thermal crossing of the barrier. The second sound thus acts as a pulsed heat source for evaporation. A heat pulse is generated by resistive heating of a planar thin-film heater surrounding the radioactive source. This heat pulse evolves into a shock wavefront and propagates upwards in the superfluid helium and impinges on the surface. The only modification in the experimental setup (see section 6.1) is the addition of a heater to produce second sound pulses (see Figure 6.9). A nickel-chromium thin-film acts as heater to generate second-sound waves. Nickel-chromium was chosen because of its constant electric resistance down to superfluid helium temperatures. The thin-film heater is prepared at the KVI target laboratory by evaporative deposition of nickel-chromium on an annular quartz plate of 27 mm outer diameter, 7 mm inner diameter and 1 mm thickness which has a narrow radial gap. The film is deposited with a uniform thickness across the quartz substrate. A narrow copper thin-film

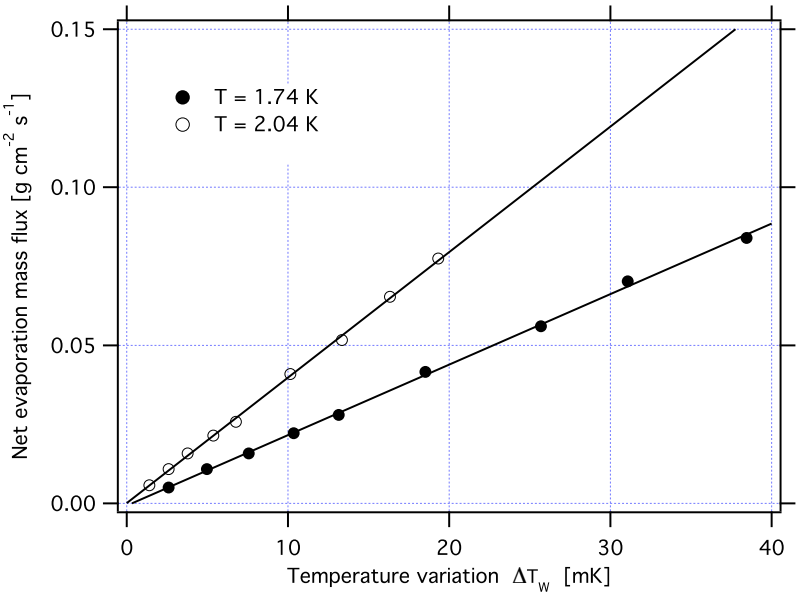

Figure 6.10: *Net evaporation mass flux as a function of the temperature variation ΔT_W at the second sound wave front for the bulk helium temperatures 1.74 K and 2.04 K (from [47]).*

strip is deposited on the nickel chromium edge along the radial gap to provide a uniform electrical contact. The thickness of the deposition is adjusted to obtain a resistance of about 100 Ω across the copper electrical contacts. The thin-film heater is placed at the same height as the ^{223}Ra source. The second sound heater is kept at the same electric potential as the source and the bottom electrode, which all are connected in series. In order to create a second sound pulse, the bias voltage of one of the thin-film heater contacts is pulsed with a rectangular voltage pulse from a floating power supply. The resulting current pulse creates a heat pulse with the same width and period as the driving voltage pulse. Its amplitude is proportional to the voltage amplitude. The generated second sound pulse travels along the ion transport trajectory. A pulse width of at least an order of magnitude less than the pulse period is used to avoid any significant effect on the ion transport. A pulse height of 150 V and a pulse width of 10 μs were chosen for all the measurements at 1.6 K and 1.15 K. The energy produced per pulse is 2.25 mJ. The heat input into the cell by the second sound pulse could be observed by a drop in the temperature controller heater power output. The power input by second sound pulses and the drop in temperature controller heater power are in agreement within about 10%, giving confidence in the proper operation of the second sound heater.

From the experimental results of Furukawa et al. [47] it is possible to calculate the thickness of the superfluid helium surface layer evaporated by a second sound

pulse. Heating of the nickel chromium heater creates a thermal pulse with a temperature amplitude ΔT_i given by linear acoustic theory as [47]

$$\Delta T_i = \frac{q}{\rho_{0,L} C_{ss} c_p}, \tag{6.8}$$

where q is the peak value of the heat flux supplied by the nickel chromium-heater, $\rho_{0,L}$ and c_p are the density and the heat capacity of superfluid helium and C_{ss} is the velocity of the second sound at the corresponding helium temperature T (see Figure 3.4). The heat flux q (W cm^{-2}) is given by

$$q = \frac{V_p^2}{A_h R_h}, \tag{6.9}$$

where V_p is the amplitude of the voltage pulse and R_h and A_h are the resistance and area of the nickel-chromium heater. The thermal pulse emitted by the heater travels upwards and impinges onto the superfluid surface. The thermal pulse is partially reflected. The resulting temperature variation is give by

$$\Delta T_W = \Delta T_i + \Delta T_r, \tag{6.10}$$

where ΔT_i and ΔT_r are the temperature rise at the impinging and reflected wave fronts. The reflection coefficient of a thermal pulse at normal incidence $R_{22} = \Delta T_r / \Delta T_i$ was measured by Murakami et al. [77] as 0.8. For superfluid helium R_{22} is a temperature independent quantity [77]. Thus the ΔT_W can be expressed as $1.8\,\Delta T_i$. In this experiment the temperature rise at the superfluid surface at the incidence of the second sound pulse can be calculated and is about 125 mK and about 900 mK for 1.6 K and 1.15 K respectively. Figure 6.10 [47] shows the net evaporation mass flux as a function of the temperature variation ΔT_W at the second sound wave front for bulk helium temperatures of 1.74 K and of 2.04 K. The net evaporation mass flux is the mass of the superfluid helium evaporated from unit area of superfluid surface per second. The thickness of the superfluid surface layer evaporated by the heat pulse used in this experiment is larger than 100 nm, which should be sufficient to evaporate the surface layer containing the trapped ions.

6.2.2 Results

Contrary to expectation, the evaporation of the superfluid helium surface by second sound gave no enhancement but rather a negative effect on the extraction efficiency. Figure 6.11 shows the extraction efficiencies at 1.60 K and 1.15 K as a function of second sound pulse period. At long pulse periods the extraction efficiency remains the same as that obtained in measurements without second sound pulses. The extraction efficiency shows an exponential fall-off with decreasing pulse period. Figure 6.12 shows the snowball efficiency at 1.60 K and 1.15 K as a function of second sound pulse period. No significant change in the snowball efficiency as a function of second sound pulse period is observed.

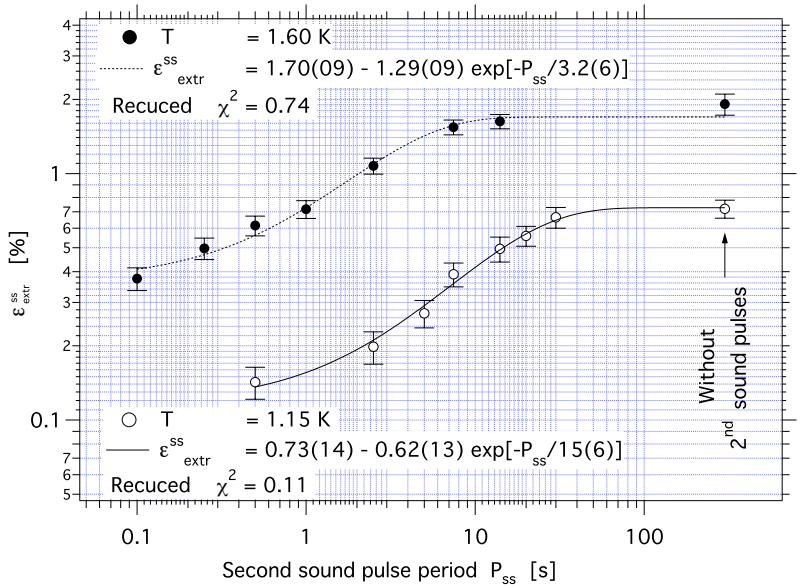

Figure 6.11: *Extraction efficiency ϵ_{extr} as a function of second sound pulse period P_{ss} for the temperatures 1.15 K and 1.60 K. The lines represent a fit with an exponential plus a constant.*

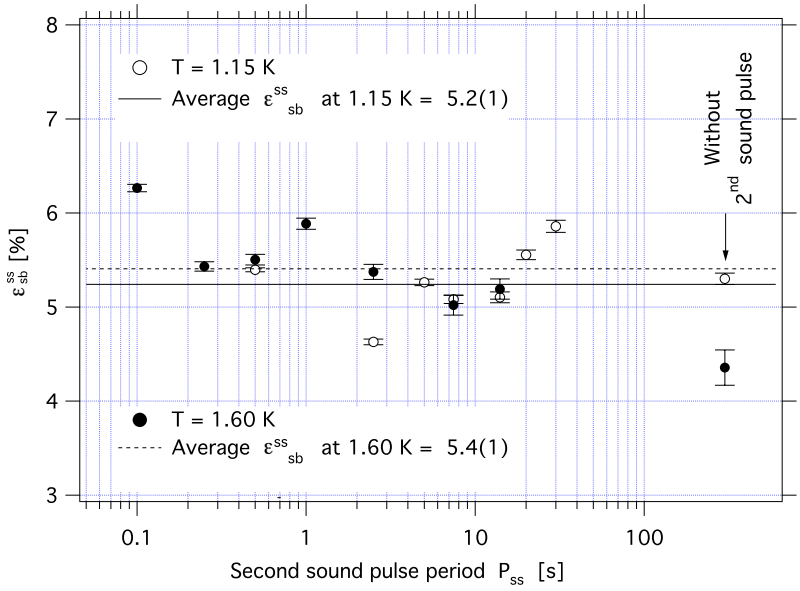

Figure 6.12: *Snowball efficiency ϵ_{sb} as a function of second sound pulse period P_{ss} for the temperatures 1.15 and 1.60 K. Rather similiar and constant snowball efficiencies are obtained at 1.60 K and 1.15 K.*

6.2.3 Discussion

Figure 6.11 shows the extraction efficiency as a function of the second sound pulse period. The extraction efficiency decreases with decreasing pulse period; for large pulse periods, the extraction efficiency saturates at the value measured without second sound pulses. Data points without second sound pulses are from experiment A (see section 6.1.2). Once the second sound pulse hits the superfluid helium surface the extraction process is apparently disturbed, and it recovers during the time gap between the pulses. Figure 6.11 shows the best fit of the function

$$\epsilon_{extr}^{ss} = \epsilon_{extr}^{0} - Ae^{-P_{ss}/\tau} , \tag{6.11}$$

to the data, where ϵ_{extr}^{ss} is the extraction efficiency with second sound pulsing, ϵ_{extr}^{0} is the extraction efficiency in the absence of second sound pulsing, P_{ss} is the second sound pulse period and τ is the "recovery time" of the extraction after the creation of a second sound pulse. The recovery times τ for the measurements at 1.60 and 1.15 K are 3.2(6) s and 15(6) s respectively, and the extraction efficiencies ϵ_{extr}^{0} are 1.7(1) and 0.73(14)% respectively.

Figure 6.12 shows the snowball efficiency ϵ_{sb}^{ss} at 1.6 and 1.15 K as a function of the second sound pulse period. No considerable difference in the snowball efficiencies between the 1.6 and 1.15 K data is observed. The snowball efficiency rather remains constant with respect to the second sound pulse period. This indicates that the number of ions trapped below the surface layer remains constant regardless of the destruction of the extraction efficiency. This result also seems to indicate that the trapped ions move downwards follow the superfluid surface during the evaporation.

No explanation for the observed destruction of extraction phenomenon is yet available as the physical processes involved are unknown. A detailed theoretical study is necessary to help understand the results. One may speculate that snowballs attach themselves to vortices created by the second sound pulse. It is known that second sound pulses create quatum turbulence (see e.g. [55]), which in a simple picture is represented as a tangle of vortex lines (see [123] for a review on quantum turbulence). It is well-known that snowballs attach themselves to vortices [18] and under certain conditions, quantum turbulence has a long decay time (e.g. Milliken et al. measure a decay time of 1.7 s at 1.45 K [74]). The assumption that ^{219}Rn snowballs attach themselves to vortices created by the second sounce pulse and as while being attached cannot be extracted from superfluid helium together with a long turbulence decay time can explain our experimental observations.

6.3 Conclusion

The survival of thermalized snowballs in superfluid helium depends strongly on how fast they are transported out of the electron-rich region where they are produced from slowed-down recoil ions. The snowball efficiency reaches a saturation

value at sufficiently high electric fields. The electric field strength needed to reach the saturation depends strongly on the ionization density. The saturation value of the snowball efficiency is independent of the superfluid helium temperature.

The exponential increase in the extraction efficiency of positive ions across the superfluid-vapor interface with increasing temperature indicates that the extraction is a thermally activated process. Our data between 1.4 and 1.8 K yield a potential barrier of about 20 K. The extraction efficiency below about 1.3 K is much larger than the extrapolation of thermally activated extraction and points to another mechanism being dominant below 1.3 K. This mechanism may very well also be present above 1.3 K but it is dominated by the thermal crossing of the barrier. It is interesting to note that the extraction efficiency below 1.3 K is quite similar in all experiments (0.5-0.8%).

The evaporation of the superfluid surface by second sound heat pulses has a lasting negative impact on the ion extraction efficiency. It takes 3.2(6) s at 1.60 K and 15(6) s at 1.15 K for the extraction process to recover from a disturbed state of yet unknown nature. One may speculate the trapping of ions in the vortex tangle created by the second sound induced turbulence.

7 Conclusion and outlook

The purpose of this thesis project was to investigate the possibility of using cryogenic noble gases and superfluid helium as stopping media for ion catchers.

Cryogenic noble gas ion stopping medium

Underlying physics and mechanisms

Based on the literature survey of physical processes in ionized cryogenic helium gas, the following conclusions are drawn:

- Most physical processes involved in the cryogenic ion catcher fall within the classical and elastic collision limit. The positive ion mobility is an important parameter determining the efficiency as it determines the extraction time of ions from the stopping volume.
- Given the helium densities used in noble gas ion catchers, He_2^+ is the dominant ion in ionised helium gas above a temperature of about 200 K. Below this temperature, He_3^+ is dominant. The electric field to density ratios considered here are not large enough to induce the breakup of He_3^+.
- The main ion-loss mechanism in a cryogenic helium gas ion catcher is recombination loss. Recombination of thermalized high-energy ions obviously has a negative impact on the total efficiency whereas helium ion recombination is a positive factor. Recombination of helium ions decreases the space charge problem associated with the ion beam and removes the free electrons from the ionization region.
- For the helium gas densities and temperatures relevant for the cryogenic helium gas ion catchers, 3-body recombination dominates the 2-body recombination by an order of magnitude.

- The recombination coefficient of helium ions shows a temperature dependence of $T_g^{-2.5}$ for the 3-body recombination coefficient α_3. The same temperature dependence is observed for simple molecular ions in helium down to 77 K. Recombination also depends strongly on the electron temperature which in turn depends on the ionization method and can be much higher than the gas temperature.

- Most of the available data on the recombination mechanism is restricted to helium gas densities less than 10^{18} cm^{-3} at room temperature. A detailed theoretical and experimental study dedicated to understand the recombination process in low-temperature high-density helium gas is necessary for a deeper understanding of the physical processes involved.

Key experimental observations

Off-line experiments on cryogenic helium gas as a stopping medium demonstrated large stopping and transport efficiencies of ^{219}Rn ions in noble gas stopping media of low purity in a container that is not ultra-high vacuum compatible by in-situ purification of the noble gas upon cooling to below 90 K. In an on-line experiment we have investigated the survival and transport efficiency of ^{219}Rn ions in high-density cryogenic helium gas, with ionisation of the gas induced by a proton beam. The combined efficiency of ion survival and transport by an applied electric field was measured as a function of ionisation rate density for electric fields and for three temperature and density combinations. The main results from the off-line and on-line measurements are:

- For high enough electric field, no neutralization takes place after slowing down. The measured efficiency is the result of charge exchange during slowing down and as such represents a fundamental upper limit to the efficiency of noble gas ion catcher devices. This upper limit depends on the chemical nature and the atomic structure of both ion and gas.

- In a separate experiment the mobility of ^{219}Rn ions in helium, neon and argon at 77 K is measured. The results are comparable to those of xenon in the respective gases.

- On-line results demonstrate the importance of a high electric field to quickly pull ions and electrons apart and as such reduce the neutralisation probability in the ionization region. Both on-line and off-line measurements demonstrate that the cryogenic helium at high density and high electric field is a promising medium for an ion catcher.

- The main conclusion of the studies on cryogenic noble gas ion stopping media is that helium is the most ideal among noble gases to be used as stopping medium for high-energy ion beams due to its high ionization potential.

- The measured efficiencies at low temperature are comparable to those achieved with ultra-high purity gas catchers at room temperature. However, constructing a cryogenic noble gas ion catcher operating at liquid nitrogen temperature is technically easier. To reach the required purity levels of less than 1 ppb, room temperature gas cells have to be pumped to high vacuum and baked for a long time before being operational, whereas in cryogenic gas cells this is achieved without long pre-preparations. It may therefore be a more reliable and practical choice.
- The idea of freezing out the impurities in a helium gas catcher has caught the attention of several groups in recent years. Unknown to us at the time of our experiments, M. Wada at RIKEN tested a cold trap at liquid nitrogen temperature placed inside the gas cell in order to purify the helium gas. Although this system did not maintain a low temperature in the helium gas, an increase in efficiency of a factor of 10 was reported [125, 124]. Wada et al. are planning a fully cryogenic gas cell to be installed at the universal slow RI-beam facility (SLOWRI) at the RIBF at RIKEN [126]. New gas catchers being developed at the National Superconducting Cyclotron Laboratory at Michigan State University are planned to be cryogenic [52]. Plans to replace the gas cell at the SHIPTRAP facility at GSI with a cryogenic version have been presented [37].

Superfluid helium ion stopping medium

Underlying physics and mechanisms

The possibility of superfluid helium as stopping medium for ion catchers is investigated. An overview of the properties of positive ions and electrons in superfluid helium shows strikingly different behavior due to the different nature of their interactions with the ambient medium. This project concentrated on properties of snowballs such as their survival and extraction efficiencies. On the basis of the literature survey on underlying physical processes the following observations could be made:

- The interaction of snowballs with the superfluid-vapor interface is not well understood. If we believe that the potential barrier present is purely image charge character, there should be no change in barrier height with respect to temperature.
- The barrier height and location of the potential minimum at the superfluid-vapor interface depend strongly on the density profile of the interface. An accurate theoretical description of the extraction of positive ions and the size of the potential barrier is not available yet. For a more realistic image charge potential barrier calculation one should include the actual density profile of the superfluid-vapor interface.

- The size of the snowball is comparable to the width of the interface. This may very well influence the extraction process. A detailed theoretical study is necessary to understand the mechanism of positive ion extraction across the superfluid-vapor interface.
- When pushed towards the superfluid-vapor interface, electron bubbles explode as a result of the combination of thermal motion and quantum tunneling and release the bare electron into the vapor phase. This indicates that the structure of the charged complex plays a key role in the extraction mechanism.
- An experimental study on extraction of alkaline earth metal ions from superfluid helium will give a more clear picture of the ion extraction process across the superfluid-vapor interface. The role of quantum tunneling in the extraction can be ruled out due to large mass of the ions as compared to the electron.

Key experimental observations

The main objective of the off-line experiments on superfluid helium was to study the dependence of the survival of snowballs on applied electric fields and the dependence of their extraction across the superfluid-vapor interface on temperature. A new idea to enhance the extraction by evaporating the superfluid helium layer containing the trapped ions and thus release them to the vapor phase is also experimentally investigated. Key results from our experimental studies on superfluid helium as ion stopping medium are:

- The survival of thermalized snowballs in superfluid helium depends strongly on how fast they are transported out of the electron-rich region where they are produced from slowed-down recoil ions. The snowball efficiency reaches a saturation value at sufficiently high electric fields. The electric field strength needed to reach saturation depends strongly on the ionization density.
- The exponential increase in the extraction efficiency of positive ions across the superfluid-vapor interface above about 1.3 K with increasing temperature indicates that the extraction is a thermally activated process. Our data yields a potential barrier of about 20 K.
- The extraction efficiency below about 1.3 K is constant and much larger than the extrapolation of the thermally activated extraction. This points to another mechanism being dominant below 1.3 K.
- No clear explanation for the observed phenomenon related to second sound assisted evaporation of the superfluid surface layer is yet available as the physical processes involved are unknown. One may speculate the trapping of ions in the vortex tangle created by the second sound induced turbulence. A detailed theoretical study is necessary to help understand the results.

- The constant snowball efficiency for superfluid surface evaporation assisted by second sound pulses indicates that the number of ions trapped below the surface layer remains constant regardless of the destruction of the extraction efficiency.
- Given extraction efficiencies of positive ions across the superfluid-vapor interface, superfluid helium can be used as a stopping medium for ions with high snowball efficiencies. Snowball efficiencies between 5 to 30% observed for different ionic species and an extraction efficiency of about 30% at 2 K gives a total efficiency between 1 to 10%. The high vapor density at higher temperatures is however not favorable for the fast transport of ions in the vapor phase.

Summary

Superfluid helium and cryogenic noble gases as stopping media for high-energy ions

Many scientific disciplines make use of radioactive ions in the form of a low-energy ion beam or a cold ion or atom cloud. Since radioactive isotopes are often best produced at very high energy, techniques to transform high-energy ions efficiently and quickly into low-energy ones are essential. In this context, the usefulness of superfluid helium and cryogenic noble gases was investigated.

The extreme purity of cryogenic noble gases allowed to demonstrate for the first time that the maximum efficiency in this kind of systems is determined by the chance of survival of ions during slowing down. This principal limit, a few tens of percent, is high enough to make the method of practical use. Experiments in which high-density cryogenic helium was ionized by a proton beam show the importance of a large electric field; a field that quickly pulls ions and electrons apart and thus prevents neutralization. We demonstrated that at high fields, the maximum efficiency is maintained at ionization densities many times larger than achieved up to now with other systems.

Two mechanisms play a role in the extraction of ions out of superfluid helium: thermal excitation, which is strongly temperature dependent, and an as yet unknown temperature independent mechanism. The transition between these two lies at a temperature of about 1.3 Kelvin. The combined efficiency for ion survival in and extraction out of superfluid helium lies between 1 and 10 percent; high enough for practical applications.

Samenvatting

Supervloeibaar helium en cryogene edelgassen voor het afremmen van hoogenergetische ionen

Veel wetenschappelijke disciplines maken gebruik van radioactieve isotopen in de vorm van een laagenergetische ionenbundel of een koude ionen- of atomenwolk. Omdat radioactieve isotopen vaak optimaal geproduceerd worden bij zeer hoge energieën zijn technieken om hoogenergetische ionen efficiënt en snel om te zetten in ionen met lage energie essentieel. In dit verband werd het nut van supervloeibaar helium en cryogene edelgassen als afremmedia onderzocht.

Door de extreme zuiverheid van cryogene edelgassen kon voor het eerst worden aangetoond dat de maximale efficiëntie in dit soort systemen bepaald wordt door de overlevingskans van de ionen tijdens het afremmen. Deze principiële limiet is met enkele tientallen procenten zo hoog dat de methode praktisch nut heeft. Experimenten waarbij cryogeen helium met hoge dichtheid wordt geïoniseerd door een protonenbundel tonen het belang van een hoog elektrisch veld aan; een veld dat ionen en elektronen snel uit elkaar trekt en zodoende neutralisatie belemmert. Er werd aangetoond dat bij hoge velden de maximale efficiëntie behouden blijft bij ionisatiedichtheden die vele malen hoger zijn dan tot nu toe met andere systemen werd bereikt.

Bij de extractie van ionen uit supervloeibaar helium blijken twee mechanismen een rol te spelen: thermische excitatie die sterk temperatuursafhankelijk is en een nog onbekend temperatuursonafhankelijk mechanisme. Het omslagpunt tussen deze twee ligt bij een temperatuur van ongeveer 1.3 Kelvin. De gecombineerde efficientie voor het overleven van ionen in en extractie uit supervloeibaar helium ligt tussen 1 en 10 procent; hoog genoeg voor praktische toepassingen.

Acknowledgment

With the completion of this thesis, an immensely enriching phase of my life comes to a fruitful conclusion. Further, it is very gratifying to know that the key results of this project are going to be implemented in a real application and I would like to thank everybody who directly or indirectly helped me reach this point.

In one way, this PhD thesis is a testimony to my love of Physics yet, this work could not have been possible without the personal and professional support of numerous people. I am most indebted to Dr. Peter Dendooven for being a patient supervisor and for his consistent support, guidance and never failing kindness. He is responsible for involving me in the RIASH project in the first place. Peter and his wife Liisa Heiman have always been there as good friends and I would like to thank Liisa, her care, support and hospitality during these years.

I would like to express my deep and sincere gratitude to my Promoter, Prof. Klaus Jungmann for his constant support and advice. Not a page has appeared in this dissertation, which he has not read, reflected and commented on.

I owe a huge debt of gratitude to Prof. Kurt Gloos and Prof. Noriaki Takahashi for all their help, advice and enlightening insights. Their willingness to read and comment on the manuscript is highly appreciated.

For having accepted to act as members of my Thesis reading committee, as well as for their valuable suggestions and comments, I warmly thank Prof. Juha Äystö, Prof. Ronnie Hoekstra and Prof. Christoph Scheidenberger.

The help, cooperation and hospitality offered by the Jyväskylä crew, especially Kari Peräjärvi, Antti Saastamoinen, Heikki Penttilä, Iain Moore and Tetsu Sonada is very much appreciated. For facilitating the smooth running of on-line experiments, I would also like to acknowledge the contribution made by the mechanical workshop, electronics department and cyclotron operators at the Department of Physics, University of Jyväskylä (JYFL), Finland.

I would like to thank the Director of KVI, Prof. Muhsin Harakeh for employing me at KVI. Many thanks to Prof. Rob Timmermans, Prof. Hans Wilsschut, Dr.

Gerco Onderwater and Dr. Lorenz Willmann for in depth discussions and support. I am especially grateful to the mechanical workshop, electronics, vacuum and IT departments for accommodating my off-schedule 4 pm requests. I would like to thank the personnel and financial departments for helping me through my unusual visa scenarios. Hans Vorenholt, Harry Timersma, Michel Hevinga, Henk Kooi, Nanko de Vries, Ronald van Wooning, Imko Smid, Willem Olthuis, Hans Dost, Roelof Dussel, Jelke Wieringa, Henk Groter, Alfred Felzel, Hilde Landstra, Hilde van der Meer, I owe you a debt of gratitude. I would also like to thank Marjan Koopmans and Amarins Petitiaux for their excellent organization of the FANTOM study weeks.

Many thanks are also due to the many mentors, colleagues, and friends in the Netherlands I came across along the way. I am greatly indebted to Dr. Otto Muskens and Prof. Jaap Dijkhuis for providing me with the opportunity to do my Master thesis at the Atom Optics & Ultrafast Dynamics group at Utrecht University. They were my original source of inspiration for coming to the Netherlands to advance my education.

I met many wonderful people during my time at KVI. Ahmad, Albert, Alma, Andraey, Andrija, Aran, Dennis, Duurt, Elmaddin, Gabriel, Hossein , Hossein Moeini, Ileana, Leila, Lotje, Marlene, Manisha, Minh, Mohammad, Ola, Ruud, Sadia, Simona, Suresh, Sybren, Vanni, Victor and Wilbert, I owe you a bunch for keeping me in good spirits. Special thanks to Oscar Versolato. I am pleased that you accepted to be my paranymph.

Special thanks to my “smoking room” mates, Johan Messchendorp, Tjalling Nijboer, Erwin Bodewits, Mohammad Babai, Alexander Usov and Petra Mossel, for many wonderful conversations we had.

My Keralite friends in Europe; they made here a home away from home. Abdul, Bahju and Achoos, with whom I have spent most of my free time, many thanks for being there with me in my ups and downs. Noby, Neethu, Anthappan and Immochan, thanks for always keeping your door open for me. Rajiv, Miek, Mini and Naomi, thanks for having me as a member of your family. Sreeji, Divya, Achoos, and Aarchi thank you very much for the nice times together. Nibu, Sherin and Tharun, Anaz, Shams, Reshmi, Jeena and Pradeep, Shibu and Prathibha, and all those wonderful people I met during NANMA events, thanks for all those nice moments we have had together. Prasanth, Aneesh, Jojo, Marina, Sony and Deepthi, you guys made my stay in Utrecht memorable. My heartfelt thanks to all my CUSAT mates for your support and nice times together. Vinu, Rajesh, Manesh, Mahesh, Abraham, Denny, Mercy, Reshmi, Jyotsna and Lee, thanks for being there, whenever needed.

I would also like to express my deep gratitude to all my teachers who have taught me through the years. Though only a few of then I mention here by name. I am deeply indebted to Prof. Pappootty, Prof. Suresh, Dr. Ramakrishnan, Dr. Narayanan, Abdunnur and Sasi from Government College, Madappally, Prof. Rameshbabu, Prof. Kuriakose, Prof. Sabir and Dr. Abdul Rasheed from

CUSAT for showing the beauty of physics and guiding me through.

I have been fortunate in meeting many wonderful people who made my stay in Groningen unforgettable. Far too many people to mention individually; but my sincere gratitude to them all. In particular, Sarah Dean, Andrea Scaramucci, Sophie Jaquier, Ana Moreno Monroy, Birgit Schwabl, Linda King, Marta Giulia, Laurence Bianchini, Mirre Boot, Julija Karpoviciute, Ana Lopera, Judit Hauber, Kim Roest, Myrte Cransberg, Joana Seixas, Ulrike Wegner, Christine Walsh, Jorn Veenstra, Tom Trummer, Edurne Jimenez, Tiago Brito, Gregor Schneider, Primoz Pirih, Leah Broussard, Magdalena Sucha, Julia Kleinschmidt, Sophia Zeschitz, Dieke Heerschop, Anna Oshkalo, Carlos Reis, Christos Pashalidis, Ramesh, Iskander Theuns, Ajay Bailey, thanks for being there!. Special thanks to Annika Stritzke for always being there as a "friend in need". Anni, it means a lot to me that you will stand by me as a paranymph.

I would also like to thank my friends back home; Aneesh, Adheep, Sandesh, Dr. Sunil Kumar, Anu, Neethu, Nitin, Shibu, Navas, Binu, Ranjith (chimbu), Arun anand(Kidu), Abhinand, Gineesh, Saju, Lishma, Rajeesh (kuttan), Lalu, for helping me get through the difficult times, and for all the emotional support, camaraderie, entertainment, and care they have provided.

These acknowledgments would not be complete without thanking my family for their support throughout my seemingly endless years in school. I thank my father Purushothaman, my mother Santha, my brother Arjun for standing by me for in whatever I wanted to do. Their everlasting encouragement and love helped me see it through calmly to the end. I also wish to extend my thanks to the family of my better half Maryam, especially Aliakbar Ghorbani, Fezzeh Mahmoudi and Fahimeh Mahmoudi for their encouragement. And last but obviously not the least to my Maryam: Thank you for your patience, inspiration and love.

Groningen, November 2008

List of Figures

List of Tables

List of Publications

1. P. Dendooven, S. Purushothaman, and K. Gloos. On a cryogenic noble gas ion catcher. *Nucl. Instrum. Methods. A*, 558(2):580–583, 2006.

2. P. Dendooven, on behalf of the TRIμP group and the RIASH group. New developments in TRIμP and RIASH at KVI. Proceeding of the *Frontiers in Nuclear Structure, Astrophysics, and Reactions (FINUSTAR)*, Isle of Kos (Greece), 12-17 September 2006. *AIP Conf. Proc.*, 831:39-43, 2006.

3. P. Dendooven, S. Purushothaman, K. Gloos, J. Aysto, N. Takahashi, and W. X. Huang, Radioactive ions and atoms in superfluid helium. Proceeding of the *Frontiers in Nuclear Structure, Astrophysics, and Reactions (FINUSTAR)*, Isle of Kos (Greece), 12-17 September 2006. *AIP Conf. Proc.*, 831:39-43, 2006.

4. S. Purushothaman, P. Dendooven, I. Moore, H. Penttilä, J. Ronkainen, A. Saastamoinen, J. Äystö, K. Peräjärvi, N. Takahashi and K. Gloos. Cryogenic helium as stopping medium for high-energy ions. Proceeding of the *Conference on Electromagnetic Isotope Separators and Techniques Related to their Applications (EMIS 2007)*, 24-29 June 2007, Deauville (France), *Nucl. Instrum. Methods B*, 2008 (in press).

5. S. Purushothaman, K. Peräjärvi, M. Ranjan, A. Saastamoinen, K. Gloos, N. Takahashi, and P. Dendooven. Positive ion extraction across the superfluid-vapor helium interface. Proceeding of the *25th International Conference on Low Temperature Physics (LT25)*, 6-13 August 2008, Amsterdam (Netherlands), submitted to *J. Phys: Conf. Ser.*

References

[1] J. F. Allen and A. D. Misener. Flow of liquid helium II. *Nature*, 141:75–75, 1938.

[2] S. K. Allison. Experimental results on charge-changing collisions of hydrogen and helium atoms and ions at kinetic energies above 0.2 keV. *Rev. Mod. Phys.*, 30(4):1137–1168, 1958.

[3] J. R. Alonso. Medical applications of nuclear physics and heavy-ion beams. *Nucl. Phys. A*, 685(1-4):454–471, 2001.

[4] L. L. Alves and C. M. Ferreira. Electron kinetics in weakly ionized helium under dc and hf applied electric fields. *J. Phys. D*, 24(4):581–592, 1991.

[5] F. Ancilotto and F. Toigo. Properties of an electron bubble approaching the surface of liquid helium. *Phys. Rev. B*, 50(17):12820–12830, 1994.

[6] J. Ärje, J. Äystö, P. Taskinen, J. Honkanen, and K. Valli. Ion guide method for on-line isotope separation. *Nucl. Instrum. Methods A*, 26(1-3):384–393, 1987.

[7] K. R. Atkins. Ions in liquid helium. *Phys. Rev.*, 116(6):1339–1343, 1959.

[8] V. M. Atrazhev. Delocalisation of electrons in dense helium gas by external electric feild. *J. Phys. D*, 17(5):889–902, 1984.

[9] J. Äystö. Development and applications of the igisol technique. *Nucl. Phys. A*, 693(1-2):477–494, 2001.

[10] R. Barrera and G. Baym. Roton-limited mobility of ions in superfluid He^4. *Phys. Rev. A*, 6(4):1558–1566, 1972.

[11] A. Bartels. Density dependence of electron drift velocities in helium and hydrogen at 77.6 K. *Appl. Phys. A*, 8(1):59–64, 1975.

[12] D. R. Bates. Classical theory of electron-ion recombination in an ambient gas. *J. Phys. B*, 13(13):2587–2599, 1980.

[13] M. Beau, H. Gunther, G. zu Putlitz, and B. Tabbert. Atoms and ions in superfluid helium. *Z. Phys. B*, 101(2):253–262, 1996.

[14] J. S. Brooks and R. J. Donnelly. The calculated thermodynamic properties of superfluid helium-4. *J. Phys. Chem. Ref. Data*, 6(1):51–104, 1977.

[15] L. Bruschi, B. Maraviglia, and F. E. Moss. Measurement of a barrier for the extraction of excess electrons from liquid helium. *Phys. Rev. Lett.*, 17(13):682–684, 1966.

[16] L. Bruschi, P. Mazzoldi, and M. Santini. Periodic critical velocities of ions in liquid helium II. Temperature dependence. *Phys. Rev.*, 167(1):203–214, 1968.

[17] L. Bruschi, P. Mazzoldi, and M. Santini. Positive ions in liquid helium II. The critical velocity for creation of vortex rings. *Phys. Rev. Lett.*, 21(26):1738–1740, 1968.

[18] A. G. Cade. Binding of positive-ion complexes to vortex rings in liquid-helium II. *Phys. Rev. Lett.*, 15(6):238–239, 1965.

[19] Y. S. Cao and R. Johnsen. Neutral-stabilized electron-ion recombination in ambient helium gas. *J. Chem. Phys.*, 94(8):5443–5446, 1991.

[20] G. Careri, S. Cunsolo, and P. Mazzoldi. Periodic discontinuities in the drift velocity of ions in liquid helium II. *Phys. Rev.*, 136(2A):303–310, 1964.

[21] G. Careri and F. Gaeta. Ionic recombination in liquid helium. *Il Nuovo Cimento*, 20(1):152–160, 1961.

[22] S. Chandrasekhar. Stochastic problems in physics and astronomy. *Rev. Mod. Phys.*, 15(1):1–89, 1943.

[23] E. Cheng, M. W. Cole, and M. H. Cohen. Binding of electrons to the surface of liquid helium. *Phys. Rev. B*, 50(2):1136–1142, 1994.

[24] J. Classen, C. K. Su, M. Mohazzab, and H. J. Maris. Electrons and cavitation in liquid helium. *Phys. Rev. B*, 57(5):3000–3010, 1998.

[25] M. W. Cole and R. A. Bachman. Structure of positive impurity ions in liquid helium. *Phys. Rev. B*, 15(3):1388–1394, 1977.

[26] C. B. Collins, H. S. Hicks, W. E. Wells, and R. Burton. Measurement of the rate coefficient for the recombination of He^+ with electrons. *Phys. Rev. A*, 6(4):1545–1558, 1972.

[27] C. A. Colmenares. Bakeable ionization chamber for low-level tritium counting. *Nucl. Instrum. Methods*, 114(2):269–275, 1974.

[28] R. W. Crompton, M. T. Elford, and R. L. Jory. The momentum transfer cross section for electrons in helium. *Aust. J. Phys.*, 20(4):369–400, 1967.

[29] R. W. Crompton, M. T. Elford, and A. G. Robertson. The momentum transfer cross section for electrons in helium derived from drift velocities at 77°K. *Aust. J. Phys.*, 23(5):667–681, 1970.

[30] D. A. Dahl. SIMION for the personal computer in reflection. *Int. J. Mass Spectrom.*, 200(1-3):3–25, 2000.

[31] D. de Klerk, R. P. Hudson, and J. R. Pellam. Second sound propagation below 1°K. *Phys. Rev.*, 93(1):28–37, 1954.

[32] R. Deloche, P. Monchicourt, M. Cheret, and F. Lambert. High-pressure helium afterglow at room temperature. *Phys. Rev. A*, 13(3):1140–1176, 1976.

[33] J. F. Delpech and J. C. Gauthier. Electron-ion recombination in cryogenic helium plasmas. *Phys. Rev. A*, 6(5):1932–1939, 1972.

[34] P. Dendooven. The development and status of the IGISOL technique. *Nucl. Instrum. Methods B*, 126(1-4):182–189, 1997.

[35] A. S. Dickinson, M. S. Lee, and L. A. Viehland. The mobility of He^+ ions in helium gas. *J. Phys. B*, 32(20):4919–4930, 1999.

[36] J. Dutton. A survey of electron swarm data. *J. Phys. Chem. Ref. Data*, 4(3):577–856, 1975.

[37] S. Eliseev, M. Block, M. Dworschak, F. Herfurth, H. J. Kluge, A. Martin, C. Rauth, and G. Vorobjev. A new cryogenic gas-filled stopping chamber for SHIPTRAP. *Nucl. Instrum. Methods B*, In Press, Corrected Proof, 2008.

[38] S. A. Eliseev, M. Block, A. Chaudhuri, Z. Di, D. Habs, F. Herfurth, H. J. Kluge, J. B. Neumayr, W. R. Plaß, C. Rauth, P. G. Thirolf, G. Vorobjev, and Z. Wang. Extraction efficiency and extraction time of the SHIPTRAP gas-filled stopping cell. *Nucl. Instrum. Methods B*, 258(2):479–484, 2007.

[39] H. W. Ellis, E. W. McDaniel, D. L. Albritton, L. A. Viehland, S. L. Lin, and E. A. Mason. Transport properties of gaseous ions over a wide energy range, Part II. *At. Data Nucl. Data Tables*, 22(3):179–217, 1978.

[40] H. W. Ellis, E. W. McDaniel, D. L. Albritton, L. A. Viehland, S. L. Lin, and E. A. Mason. Transport properties of gaseous ions over a wide energy range, Part III. *At. Data Nucl. Data Tables*, 31(1):113–151, 1984.

[41] H. W. Ellis, R. Y. Pai, E. W. McDaniel, E. A. Mason, and L. A. Viehland. Transport properties of gaseous ions over a wide energy range. *At. Data Nucl. Data Tables*, 17(3):177–210, 1976.

[42] A. Engel and R. Friedrichs. On the electromagnetic force on a polarizable body. *Am. J. Phys.*, 70(4):428–432, 2002.

[43] M. Facina. *A gas catcher for the selective production of radioactive beams through laser ionization*. PhD thesis, Katholieke Universiteit Leuven, Leuven, 2004.

[44] M. Facina, B. Bruyneel, S. Dean, J. Gentens, M. Huyse, Y. Kudryavtsev, P. van den Bergh, and P. Van Duppen. A gas cell for thermalizing, storing and transporting radioactive ions and atoms. Part II: On-line studies with a laser ion source. *Nucl. Instrum. Methods B*, 226(3):401–418, 2004.

[45] FAIR. Facility for antiproton and ion research, GSI, Germany. Available from: `http://www.gsi.de/fair/index_e.html`.

[46] M. Foerste, H. Guenther, O. Riediger, J. Wiebe, and G. Zu Putlitz. Ions and atoms in superfluid helium (^{4}He). *Z. Phys. B*, 104(2):317–322, 1997.

[47] T. Furukawa, M. Murakami, and T. Iida. Measurement of He II evaporation induced by impingement of a thermal pulse on a He II-vapor interface. *Exp. Fluids*, 30(2):181–189, 2001.

[48] GANIL. Grand acclrateur national d'ions lourds, france. Available from: `http://www.ganil.fr/`.

[49] J. B. Gerardo and M. A. Gusinow. Electronic recombination of He_3^+. *Phys. Rev. A*, 3(1):255–267, 1971.

[50] W. Glaberson and W. W. Johnson. Impurity ions in liquid helium. *J. Low Temp. Phys*, 20(3):313–338, 1975.

[51] D. J. Griffiths. *Introduction to electrodynamics*. Prentice Hall, Inc, 3 edition, 1999.

[52] C. Guénaut, G. Bollen, S. Chouhan, F. Marti, D. Morrissey, D. Lawton, J. Ottarson, G. Pang, S. Schwarz, B. Sherrill, M. Wada, and A. Zeller. The cyclotron gas stopper project at the NSCL. *Hyperfine Interact.*, 173(1):35–40, 2006.

[53] M. Hayashi and S. Ushiroda. Calculation of drift velocity of electrons in inert-gases at low E/N. *J. Chem. Phys.*, 78(5):2621–2625, 1983.

[54] H. Helm. The mobilities and equilibrium reactions of helium ions in helium at 77 K. *J. Phys. B*, 9(7):1171–1189, 1976.

[55] D. K. Hilton and S. W. V. Sciver. Direct measurements of quantum turbulence induced by second sound shock pulses in helium II. *J. Low Temp. Phys*, 141(1):47–82, 2005.

[56] W. X. Huang, P. Dendooven, K. Gloos, N. Takahashi, K. Arutyunov, J. P. Pekola, and J. Äystö. Transport and extraction of radioactive ions stopped in superfluid helium. *Nucl. Instrum. Methods B*, 204:592–596, 2003.

[57] W. X. Huang, P. Dendooven, K. Gloos, N. Takahashi, J. P. Pekola, and J. Äystö. Extraction of radioactive positive ions across the surface of superfluid helium: A new method to produce cold radioactive nuclear beams. *Europhys. Lett.*, 63(5):687–693, 2003.

[58] V. W. Hughes, D. W. McColm, K. Ziock, and R. Prepost. Muonium. I. Muonium formation and larmor precession. *Phys. Rev. A*, 1(3):595–617, 1970.

[59] J. Huikari, P. Dendooven, A. Jokinen, A. Nieminen, H. Penttilä, K. Peräjärvi, A. Popov, S. Rinta-Antila, and J. Äystö. Production of neutron deficient rare isotope beams at IGISOL; on-line and off-line studies. *Nucl. Instrum. Methods B*, 222(3-4):632–651, 2004.

[60] M. Huyse, M. Facina, Y. Kudryavtsev, P. Van Duppen, and ISOLDE collaboration. Intensity limitations of a gas cell for stopping, storing and guiding of radioactive ions. *Nucl. Instrum. Methods B*, 187(4):535–547, 2002.

[61] A. W. Johnson and J. B. Gerardo. Electronic recombination coefficient of molecular helium ions. *Phys. Rev. Lett.*, 27(13):835–838, 1971.

[62] A. W. Johnson and J. B. Gerardo. Recombination and ionization in a molecular-ion-dominated helium afterglow. *Phys. Rev. A*, 5(3):1410–1418, 1972.

[63] P. Kapitza. Viscosity of liquid helium below the λ-point. *Nature*, 141:74–74, 1938.

[64] H. A. Kramers. Brownian motion in a field of force and the diffusion model of chemical reactions. *Physica*, 7:284–304, 1940.

[65] Y. Kudryavtsev, B. Bruyneel, M. Huyse, J. Gentens, P. van den Bergh, P. Van Duppen, and L. Vermeeren. A gas cell for thermalizing, storing and transporting radioactive ions and atoms. Part I: Off-line studies with a laser ion source. *Nucl. Instrum. Methods B*, 179(3):412–435, 2001.

[66] L. Landau. Theory of the superfluidity of helium II. *Phys. Rev.*, 60(4):356–358, 1941.

[67] C. T. Lane, H. A. Fairbank, and W. M. Fairbank. Second sound in liquid helium II. *Phys. Rev.*, 71(9):600–605, 1947.

[68] F. London. The phenomenon of liquid helium and the Bose-Einstein degeneracy. *Nature*, 141(3571):643–644, 1938.

[69] F. London. *Superfluids, Volume II: Macroscopic Theory of superfluid helium.* John Wiley & Sons, New York, 1954.

[70] L. B. Lurio, T. A. Rabedeau, P. S. Pershan, I. F. Silvera, M. Deutsch, S. D. Kosowsky, and B. M. Ocko. Liquid-vapor density profile of helium: An x-ray study. *Phys. Rev. Lett.*, 68(17):2628–2631, 1992.

[71] L. B. Lurio, T. A. Rabedeau, P. S. Pershan, I. F. Silvera, M. Deutsch, S. D. Kosowsky, and B. M. Ocko. X-ray specular-reflectivity study of the liquid-vapor density profile of ^{4}He. *Phys. Rev. B*, 48(13):9644–9659, 1993.

[72] M. Maier, C. Boudreau, F. Buchinger, J. A. Clark, J. E. Crawford, J. Dilling, H. Fukutani, S. Gulick, J. K. P. Lee, R. B. Moore, G. Savard, J. Schwartz, and K. S. Sharma. Stopping, trapping and cooling of radioactive fission fragments in an ion catcher device. *Hyperfine Interact.*, 132(1):517–525, 2001.

[73] L. Meyer and F. Reif. Mobilities of He ions in liquid helium. *Phys. Rev.*, 110(1):279–280, 1958.

[74] F. P. Milliken, K. W. Schwarz, and C. W. Smith. Free decay of superfluid turbulence. *Phys. Rev. Lett.*, 48(17):1204–1207, 1982.

[75] H. B. Milloy and R. W. Crompton. Momentum-transfer cross section for electron-helium collisions in the range 4-12 ev. *Phys. Rev. A*, 15(5):1847–1850, 1977.

[76] N. F. Mott and H. S. W. Massey. *The theory of atomic collisions*. Oxford, Clarendon Press, and New York, Oxford University Press., 1933.

[77] M. Murakami, J. Fujiyama, and Y. Tanaka. Reflection of second sound thermal pulse obliquely incident on he ii free surface. *Physica B*, 329–333(Part 1):264, 2003.

[78] J. B. Neumayr, L. Beck, D. Habs, S. Heinz, J. Szerypo, P. G. Thirolf, V. Varentsov, F. Voit, D. Ackermann, D. Beck, M. Block, Z. Di, S. A. Eliseev, H. Geissel, F. Herfurth, F. P. Heßberger, S. Hofmann, H. J. Kluge, M. Mukherjee, G. Münzenberg, M. Petrick, W. Quint, S. Rahaman, C. Rauth, D. Rodríguez, C. Scheidenberger, G. Sikler, Z. Wang, C. Weber, W. R. Plaß, M. Breitenfeldt, A. Chaudhuri, G. Marx, L. Schweikhard, A. F. Dodonov, Y. Novikov, and M. Suhonen. The ion-catcher device for SHIPTRAP. *Nucl. Instrum. Methods B*, 244(2):489–499, 2006.

[79] F. E. Niles and W. W. Robertson. Conversion of atomic ions to molecular ions for the noble gases. *J. Chem. Phys.*, 43(3):1076–1078, 1965.

[80] NSCL. National superconducting cyclotron laboratory, Michigan State University (MSU), USA. Available from: `http://www.nscl.msu.edu/future/sr`.

[81] NuPECC. Nupecc report–nuclear science: Impact, applications, interactions [online]. Available from: `http://www.nupecc.org/iai2001/`.

[82] J. L. Pack and A. V. Phelps. Drift velocities of slow electrons in helium, neon, argon, hydrogen, and nitrogen. *Phys. Rev.*, 121(3):798–806, 1961.

[83] J. L. Pack, R. E. Voshall, A. V. Phelps, and L. E. Kline. Longitudinal electron diffusion coefficients in gases: Noble gases. *J. Appl. Phys.*, 71(11):5363–5371, 1992.

[84] T. C. Padmore. Motion of ions in helium II. *Phys. Rev. A*, 5(1):356–372, 1972.

[85] P. L. Patterson. Evidence of the existence of an He_3^+ ion. *J. Chem. Phys.*, 48(8):3625–3631, 1968.

[86] P. L. Patterson. Temperature dependence of helium-ion mobilities. *Phys. Rev. A*, 2(4):1154–1164, 1970.

[87] L. P. Pitaevskii. Electron recmobination in a monoatomic gas. *Sov. Phys. JETP*, 15(5):919–921, 1962.

[88] G. Ramanan and G. R. Freeman. Electron mobilities in low density helium and nitrogen gases: Momentum transfer cross sections at very low energies. *J. Chem. Phys.*, 93(5):3120–3126, 1990.

[89] F. Reif and L. Meyer. Study of superfluidity in liquid he by ion motion. *Phys. Rev.*, 119(4):1164–1173, 1960.

[90] RIKEN. RI beam factory – basic science, RIKEN accelerator research facility. Available from: `http://www.rarf.riken.go.jp/ribf/doc/ribf94e/`.

[91] J. T. Routti and S. G. Prussin. Photopeak method for the computer analysis of gamma-ray spectra from semiconductor detectors. *Nucl. Instrum. Methods*, 72(2):125–142, 1969.

[92] V. N. Samovarov and I. Fugol. Recombination decay of cryogenic helium plasma. *Sov. Phys. JETP*, 48(3):444–452, 1978.

[93] G. Savard, J. Clark, C. Boudreau, F. Buchinger, J. E. Crawford, H. Geissel, J. P. Greene, S. Gulick, A. Heinz, J. K. P. Lee, A. Levand, M. Maier, G. Münzenberg, C. Scheidenberger, D. Seweryniak, K. S. Sharma, G. Sprouse, J. Vaz, J. C. Wang, B. J. Zabransky, and Z. Zhou. Development and operation of gas catchers to thermalize fusion-evaporation and fragmentation products. *Nucl. Instrum. Methods B*, 204:582–586, 2003.

[94] W. Schoepe and G. W. Rayfield. Tunneling from electronic bubble states in liquid helium through the liquid-vapor interface. *Phys. Rev. A*, 7(6):2111–2121, 1973.

[95] K. W. Schwarz. Mobilities of charged carriers in superfluid helium. *Adv. Chem. Phys.*, 33:1–49, 1975.

[96] K. W. Schwarz. Electron localization in dense helium gas: New experimental results. *Phys. Rev. B*, 21(11):5125–5136, 1980.

[97] S. W. V. Sciver. *Helium cryogenic*. Plenum Press, New York, 1986.

[98] J. Sharpe. *Nuclear radiation detectors*. John Wiley & Sons, New York, 1955.

[99] V. B. Shikin. Mobility of charges in liquid, solid, and dense gaseous helium. *Sov. phys. usp.*, 20(3):226–248, 1977.

[100] T. Shimoda, H. Miyatake, S. Mitsuoka, Y. Mizoi, H. Kobayashi, M. Sasaki, T. Shirakura, H. Ueno, H. Izumi, K. Asahi, T. Murakami, S. Morinobu, and N. Takahashi. Preservation of nuclear spin polarization of ^{12}B in superfluid. *Nucl. Phys. A*, 588(1):235–239, 1995.

[101] W. T. Sommer. Liquid helium as a barrier to electrons. *Phys. Rev. Lett.*, 12(11):271–273, 1964.

[102] R. D. Stambaugh. *Part one. Muonium formation in noble gases and negative muon polarization in helium. Part two. Precision eighth-order solenoid.* PhD thesis, Yale University, 1974.

[103] F. Stern. Image potential near a gradual interface between two dielectrics. *Phys. Rev. B*, 17(12):5009–5015, 1978.

[104] C. M. Surko and F. Reif. Evidence for a new kind of energetic neutral excitation in superfluid helium. *Phys. Rev. Lett.*, 20(12):582–585, 1968.

[105] C. M. Surko and F. Reif. Investigation of a new kind of energetic neutral excitation in superfluid helium. *Phys. Rev.*, 175(1):229–241, 1968.

[106] N. Takahashi. Condensed-matter nuclear physics with radioactive beams snowballs in superfluid helium. *Acta Phys. Pol.*, 28(1-2):41–46, 1997.

[107] N. Takahashi. Radioactive charge carriers in liquid helium created from fast nuclear beams. *Fizika B*, 12(2):135–144, 2003.

[108] N. Takahashi, W. X. Huang, K. Gloos, P. Dendooven, J. P. Pekola, and J. Äystö. Production of zero energy radioactive beams through extraction across superfluid helium surface. *Physica B*, 329-333(Part 2):1596–1597, 2003.

[109] N. Takahashi, T. Shigematsu, S. Shimizu, K. Horie, Y. Hirayama, H. Izumi, and T. Shimoda. Impurities in superfluid helium detected via radioactivity. *Physica B*, 284-288(1):89–90, 2000.

[110] N. Takahashi and T. Shimoda. *Physics of snowballs - Impurity ions in superfluid helium in Nucleon-Hadron Many Body System*. Oxford Science Publications, 1999.

[111] N. Takahashi, T. Shimoda, Y. Fujita, T. Itahashi, and H. Miyatake. Snowballs of radioactive ions - nuclear spin polarization of core ions. *Z. Phys. B*, 98(3):347–351, 1995.

[112] N. Takahashi, T. Shimoda, H. Miyatake, S. Mitsuoka, Y. Mizoi, H. Kobayashi, M. Sasaki, T. Shirakura, H. Ueno, K. Asahi, and S. Morinobu. Freezing-out of nuclear polarization in radioactive core ions of microclusters, "snowballs" in superfluid helium. *Hyperfine Interact.*, 97-98(1):469–477, 1996.

[113] A. Takamine, M. Wada, Y. Ishida, T. Nakamura, K. Okada, Y. Yamazaki, T. Kambara, Y. Kanai, T. M. Kojima, Y. Nakai, N. Oshima, A. Yoshida, T. Kubo, S. Ohtani, K. Noda, I. Katayama, P. Hostain, V. Varentsov, and H. Wollnik. Space-charge effects in the catcher gas cell of a rf ion guide. *Rev. Sci. Instrum.*, 76(10):1035031–1035036, 2005.

[114] J. J. Thomson. Recombination of gaseous ions, the chemical combination of gases, and monomolecular reactions. *Philos. Mag*, 47:337–378, 1924.

[115] L. Tisza. Transport phenomena in helium II. *Nature*, 141(3577):913–913, 1938.

[116] W. Trimble, G. Savard, B. Blank, J. A. Clark, F. Buchinger, T. Cocolios, J. E. Crawford, A. Frankel, J. P. Greene, S. Gulick, J. K. P. Lee, A. Levand, M. Portillo, K. S. Sharma, J. C. Wang, B. J. Zabransky, and Z. Zhou. Development and first on-line tests of the RIA gas catcher prototype. *Nucl. Phys. A*, 746:415–418, 2004.

[117] A. van der Woude. Impact and applications of nuclear science: Opportunities and perspectives. *Nucl. Phys. A*, 583:51–60, 1995.

[118] R. J. van Sonsbeek, R. Cooper, and R. N. Bhave. Pulse radiolysis studies of ion-electron recombination in helium. pressure and temperature effects. *J. Chem. Phys.*, 97(3):1800–1808, 1992.

[119] J. Vervier, J. Äystö, S. Doubre, H.and Galés, G. Morrison, G.and Ricco, D. Schwalm, and K. G. E. Nupecc report – nuclear physics in Europe: Highlights and opportunities [online]. Available from: `http://www.nupecc.org/iai2001/`.

[120] L. A. Viehland and E. A. Mason. On the relation between gaseous ion mobility and diffusion coefficients at arbitrary electric field strengths. *J. Chem. Phys.*, 63(7):2913–2915, 1975.

[121] L. A. Viehland and E. A. Mason. Gaseous ion mobility and diffusion in electric fields of arbitrary strength. *Ann. Phys.*, 110(2):287–328, 1978.

[122] L. A. Viehland and E. A. Mason. Transport properties of gaseous ions over a wide energy range, part IV. *At. Data Nucl. Data Tables*, 60(1):37–95, 1995.

[123] W. F. Vinen and J. J. Niemela. Quantum turbulence. *J. Low Temp. Phys*, 128(5):167–231, 2002.

[124] M. Wada, Y. Ishida, T. Nakamura, A. Takamine, Y. Yamazaki, T. Kambara, H. Ohyama, Y. Kanai, T. M. Kojima, Y. Nakai, A. Yoshida, T. Kubo, Y. Matsuo, Y. Fukuyama, K. Okada, T. Sonoda, S. Ohtani, H. Kawakami, and I. Katayama. On-line collection of ^{8}Li ions from the projectile fragment separator using an rf ion guide system (II). *RIKEN Accel. Prog. Rep.*, 36, 2003.

[125] M. Wada, Y. Ishida, T. Nakamura, Y. Yamazaki, T. Kambara, H. Ohyama, Y. Kanai, T. M. Kojima, Y. Nakai, N. Ohshima, A. Yoshida, T. Kubo, Y. Matsuo, Y. Fukuyama, K. Okada, T. Sonoda, S. Ohtani, K. Noda, H. Kawakami, and I. Katayama. Slow RI-beams from projectile fragment separators. *Nucl. Instrum. Methods B*, 204:570–580, 2003.

[126] M. Wada, Y. Yamazaki, T. Kambara, , Y. Kanai, T. M. Kojima, Y. Nakai, A. Ishida, N. Ohshima, T. Kubo, A. Yoshida, I. Katayama, T. Nakamura, K. Okada, H. Iimura, H. Wollnik, H. A. Schuessler, and V. Varentsov. The universal slow RI-beam facility (SLOWRI) [online]. Available from: `https://ribf.riken.jp/RIBF-TAC05/12_SLOWRI-mac.pdf`.

[127] Wavemetrics Inc. Igor pro 6. Available from: `http://www.wavemetrics.com/products/igorpro/igorpro.htm`.

[128] L. Weissman, D. J. Morrissey, G. Bollen, D. A. Davies, E. Kwan, P. A. Lofy, P. Schury, S. Schwarz, C. Sumithrarachchi, T. Sun, and R. Ringle. Conversion of 92 MeV/u ^{38}Ca/^{37}K projectile fragments into thermalized ion beams. *Nucl. Instrum. Methods A*, 540(2-3):245–258, 2005.

[129] B. L. Whitten, L. W. Downes, and W. E. Wells. Collisional radiative recombination in high-pressure noble gas mixtures. *J. Appl. Phys.*, 52(3):1255–1258, 1981.

[130] L. Willmann, G. P. Berg, U. Dammalapati, S. De, P. Dendooven, O. Dermois, K. Jungmann, A. Mol, C. J. G. Onderwater, A. Rogachevskiy, M. Sohani, E. Traykov, and H. W. Wilschut. Aspects of cooling at the TRIμP facility. In *Beam cooling and related topics*, volume 821 of *AIP Conf. Proc.*, pages 523–527, 2006.

[131] J. F. Ziegler, J. P. Biersack, and U. Littmark. *The stopping and range of ions in solids*, volume 1. Pergamon Press Inc., New York, 1985.